PROPOSAL FOR A MACROMOLECULAR NEUTRON DIFFRACTOMETER (*MaNDi*) AT THE SPALLATION NEUTRON SOURCE

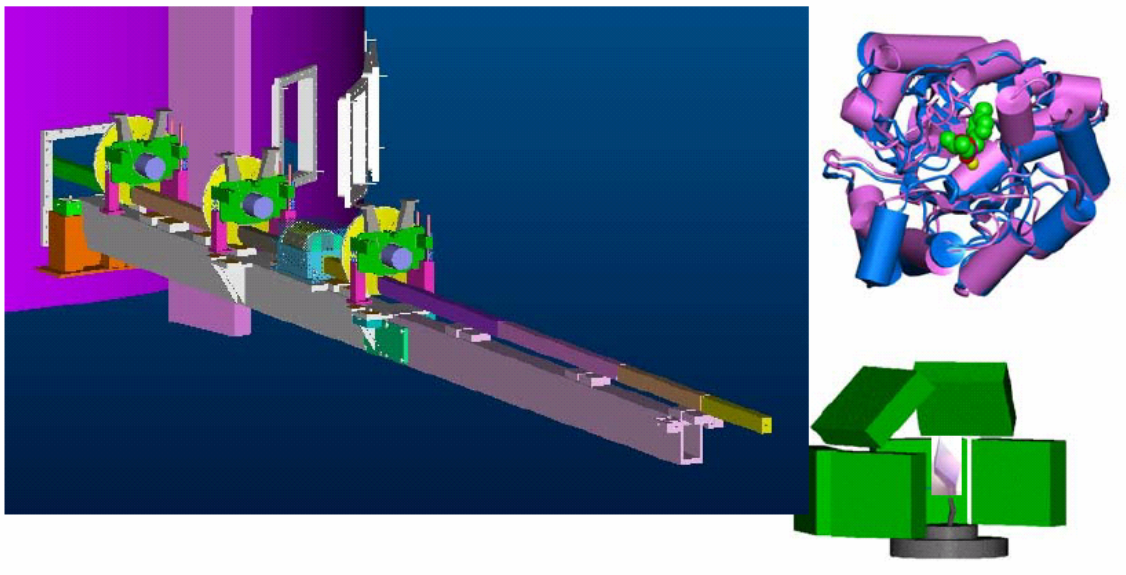

July 2004

SUMMARY

We propose to build a best-in-class, high-resolution Macromolecular Neutron Diffractometer (*MaNDi*) at the Spallation Neutron Source. *MaNDi* has been designed and optimized to achieve 1.5 Å resolution for crystals of 0.1 to 1 mm^3 with lattice repeats in the range of 150 Å. In addition, the *MaNDi* design will allow for neutron data collection, to resolutions of between 2.5 and 3 Å, on more challenging macromolecular samples with unit cell dimensions up to 250 to 300 Å. Based on an analysis of the Protein Data Bank (PDB), the proposed *MaNDi* instrument will increase the percentage of potential macromolecular systems that can be studied by neutron diffraction, by the best currently available instruments, from 49% (7,995 out of 16,252 of the structures deposited in the PDB that diffract to beyond 2.4 Å resolution and with unit cell edges < 150 Å) to 82% (13,270 out of 16,252). The large increase in the number of macromolecular systems that can be studied by *MaNDi* over currently available instruments, the unique information that can be obtained from neutron macromolecular crystallography, and the ability to collect data sets within 1 to 7 days, emphasize the potential scientific impact that we expect *MaNDi* to have on many areas of structural biology including enzymology, protein dynamics, drug design, and the study of membrane proteins.

This proposal has been prepared from contributions from the Instrument Design Group and from the participants of the workshop on "Neutron Macromolecular Crystallography at the Spallation Neutron Source" held during October 2-3, 2003 at IPNS, Argonne National Laboratory. The community enthusiastically welcomed gains of 10 to 50-fold in performance expected with the MaNDi instrument and agreed that this advance would revolutionize the field of macromolecular neutron diffraction.

ACKNOWLEDGEMENTS

The following individuals organized and assembled the main proposal as well as made significant contributions to the proposal content:

Thomas Koetzle	Argonne National Laboratory
Andrew Mesecar	University of Illinois at Chicago
Arthur Schultz	Argonne National Laboratory
P. Thiyagarajan	Argonne National Laboratory

The following individuals made significant contributions to the calculations and simulations of the instrument design:

Jason Hodges	Oak Ridge National Laboratory
Christine Rehm	Oak Ridge National Laboratory

The following individuals made significant contributions to the proposal content:

Robert Bau	University of Southern California
Gerard Bunick	Oak Ridge National Laboratory
Victor Davidson	University of Mississippi
Chris Dealwis	University of Tennessee, Knoxville
Martin Egli	Vanderbilt University
Petra Fromme	Arizona State University
Stephan Ginell	Argonne National Laboratory
Hong Guo	University of Tennessee, Knoxville
Leif Hanson	University of Toledo
John Helliwell	University of Manchester
Anthony Kossiakoff	University of Chicago
Paul Langan	Los Alamos National Laboratory
Patrick Loria	Yale University
Dean Myles	Oak Ridge National Laboratory
Alberto Podjarny	IGBMC
Benno Schoenborn	Los Alamos National Laboratory
Martha Teeter	University of California/Boston College
Peter Timmins	Institut Laue Langevin
David Worcester	University of Missouri

ORGANIZATION OF THE INSTRUMENT DEVELOPMENT TEAM (IDT):

The IDT was organized following the "Workshop on Neutron Macromolecular Crystallography at the Spallation Neutron Source", October 2-3, 2003, Argonne National Laboratory. There are currently about 50 IDT general members. The Instrument Design Group (IDG) is a subgroup of the IDT who are actively working on the design of the MaNDi instrument. In addition, an IDT Executive Committee was formed to manage and administer the IDT activities.

IDT Executive Committee:

Andrew Mesecar (Chair)	University of Illinois at Chicago
Gerard Bunick	Oak Ridge National Laboratory
Jenny Glusker	Fox Chase Cancer Center
Chris Dealwis	University of Tennessee, Knoxville
Martin Egli	Vanderbilt University
John Helliwell	University of Manchester, UK
Anthony Kossiakoff	University of Chicago
Paul Langan	Los Alamos National Laboratory
Dean Myles	Oak Ridge National Laboratory
Alberto Podjarny	IGBMC, France
Benno Schoenborn	Los Alamos National Laboratory
Arthur Schultz	Argonne National Laboratory
P. Thiyagarajan	Argonne National Laboratory

Instrument Design Group:

Arthur Schultz	Argonne National Laboratory
P. Thiyagarajan	Argonne National Laboratory
Andrew Mesecar	University of Illinois at Chicago
Jason Hodges	Oak Ridge National Laboratory
Christine Rehm	Oak Ridge National Laboratory
Dean Myles	Oak Ridge National Laboratory
Paul Langan	Los Alamos National Laboratory

IDT Members:

Last name:	**First name:**	**Institution:**
Bau	Robert	University of Southern California
Bunick	Gerard	Oak Ridge National Laboratory
Carter	Daniel	New Century Pharmaceuticals, Inc.
Davidson	Victor	University of Mississippi Medical Center
Dealwis	Chris	University of Tennessee
Egli	Martin	Vanderbilt University
Fromme	Petra	Arizona State University
Gardberg	Anna	University of Tennessee

Ginell	Stephan	Argonne National Laboratory
Glusker	Jenny	Fox Chase Cancer Center
Guo	Hong	University of Tennessee
Harrison	David H.	The Chicago Medical School
Hanson	Debra	Argonne National Laboratory
Hanson	B. Lief	University of Tennessee
He	Chuan	University of Chicago
Helliwell	John	University of Manchester
Hodges	Jason	Oak Ridge National Laboratory
Joachimiak	Andrzej	Argonne National Laboratory
Johnson	Michael E.	University of Illinois at Chicago
Koetzle	Thomas	Argonne National Laboratory
Kolesnikov	Alexander	Argonne National Laboratory
Kossiakoff	Anthony	University of Chicago
Kundrot	Craig	NASA/Marshall Space Flight Center
Laible	Phillip	Argonne National Laboratory
Langan	Paul	Los Alamos National Laboratory
Loria	J. Patrick	Yale University
Mesecar	Andrew	University of Illinois-Chicago
Myles	Dean	Oak Ridge National Laboratory
Niimura	Nobuo	JAERI
Pahl	Reinhard	University of Chicago
Podjarny	Alberto	IGBMC
Pokkuluri	Raj	Argonne National Laboratory
Rehm	Christine	Oak Ridge National Laboratory
Rosenbaum	Gerold	Argonne National Laboratory
Sanishvili	Ruslan	Argonne National Laboratory
Santarsiero	Bernard	University of Illinois at Chicago
Savage	David	University of California
Schiffer	Marianne	Argonne National Laboratory
Schoenborn	Benno	Los Alamos National Laboratory
Schultz	Arthur	Argonne National Laboratory
Stamper	Geoffrey	Abbott Laboratory
Sukumar	Narayanasami	Cornell University
Tanaka	Ichiro	JAERI
Teeter	Martha	University of California/Boston College
Thiyagarajan	P. (Thiyaga)	Argonne National Laboratory
Timmins	Peter	Institut Laue Langevin
Wlodawer	Alexander	National Cancer Institute
Worcester	David	University of Missouri

TABLE OF CONTENTS

SCIENTIFIC CASE

1.1 Overview

Neutron Macromolecular Crystallography (NMC) can fill an important niche in structural biology, enzymology, and functional genomics due to its versatility in the accurate determination of protons, protonation states, and hydration in macromolecular crystals even at a moderate 2.0 to 2.5 Å resolution (Wlodawer, 1982; Wlodawer & Hendrickson, 1982; Kossiakoff, 1983; Kossiakoff, 1984; Schoenborn, 1984; Wlodawer *et al.*, 1984; Borah *et al.*, 1985; Kossiakoff, 1985; Schoenborn, 1985; Raghavan & Wlodawer, 1987; Wlodawer *et al.*, 1989; Timmins, 1995; Schoenborn, 1996; Helliwell, 1997; Niimura *et al.*, 1997; Bon *et al.*, 1999; Niimura, 1999b; Habash *et al.*, 2000; Shu *et al.*, 2000; Coates *et al.*, 2001; Gutberlet *et al.*, 2001; Ho *et al.*, 2001; Kurihara, 2001; Ostermann *et al.*, 2002; Tsyba & Bau, 2002). Although ultra-high resolution X-ray macromolecular crystallography (UHRXMC) at third generation synchrotron sources, on cryo-protected highly ordered protein crystals, can locate some of the more ordered hydrogen atoms (Longhi *et al.*, 1997; Kuhn *et al.*, 1998; Jelsch *et al.*, 2000) and determine the protonation states of amino acid side chains (Berisio *et al.*, 1999) there are many instances where the information obtained remains inadequate. For instance, in myoglobin, even at resolutions better than 1.15 Å, UHRXMC did not provide hydrogen positions (Kachalova *et al.*, 1999; Vojtechovsky *et al.*, 1999; Miele *et al.*, 2003), whilst NMC on perdeuterated protein enabled the same hydrogen atom positions to be visualized in a structure determined to 2.0 Å resolution (Shu *et al.*, 2000).

The knowledge about protonation states of amino acid residues in the active sites of enzymes is crucial for an understanding of reaction mechanisms. Identification of protonated amino acids in the catalytic center can make it possible to discriminate between two or more competing reaction models (Schmidt *et al.*, 1996). In trypsin this type of critical information from NMC helped to resolve the question about which of the two amino acids, Asp-102 or His-57, is the origin of the catalytic proton (Kossiakoff & Spencer, 1981).

The large difference in the neutron scattering cross-sections of hydrogen and deuterium nuclei has been exploited to extract important structural information on exchangeable protons and bound water in macromolecules. At a higher resolution (1.5 Å) neutron diffraction shows the degree of order of water molecules in the crystals (Engler *et al.*, 2003). Such information is very difficult to obtain from other techniques.

Crystals of perdeuterated proteins provide enhanced visibility of deuterons in the neutron crystallographic data (Shu *et al.*, 2000), due to the combined effects of large coherent and small incoherent scattering cross-sections of deuterium, which increases the signal-to-noise ratio by a factor of eight when compared to normal proteins. This enhanced signal-to-noise ratio also makes it possible to work with much smaller crystals. Perdeuterated crystals offer unique advantages in determining the exchangeable protons and provide access to information on the charge density distribution from X-ray and

neutron difference maps. Thus, NMC offers a number of unique advantages with respect to addressing important problems in enzymology and structural biology.

Another area where NMC has a great potential to make a strong impact is the structural biology of membrane proteins. Although X-ray Macromolecular Crystallography (XMC) has tremendous success in solving the crystal structures of soluble proteins, and the Protein Data Bank (PDB) currently includes over 21,000 entries, to date only a handful of membrane proteins (36 PDB entries) have been solved despite the fact that about 30% of the genome consists of membrane bound proteins. One obvious reason for this limited success is the difficulty in growing high quality crystals of membrane proteins. A unique advantage with NMC is its ability to reveal the structure of the detergent in the membrane proteins at low resolution (Pebay-Peyroula *et al.*, 1995; Penel *et al.*, 1998; Prince *et al.*, 2003) when measurements at different contrasts are combined. Such information would be quite valuable to learn about the mechanisms involved in membrane protein crystallization and would provide impetus to the growth of this very important field.

Even though NMC is a powerful technique, its productivity has been severely constrained by the scarcity of facilities and the intrinsic low brightness of available neutron sources. Currently there are only a very limited number of instruments that are recognized to be useful for high resolution single crystal macromolecular neutron crystallography: LADI at the Institut Laue-Langevin (ILL), Grenoble, France; BIX3/BIX4 at the Japan Atomic Energy Research Institute (JAERI), Tokai; and PCS at Los Alamos National Laboratory (LANL). While the reactor based LADI and BIX3 instruments were operational during the past five to seven years, the time-of-flight diffractometer PCS at the spallation source at Los Alamos National Laboratory has only become available during early 2002.

Since its inception in 1995, LADI has raised the molecular weight ceiling above 30 kDa for NMC studies of proteins such as aspartic proteinase at 2 Å resolution (Coates *et al.*, 2001). Gilboa *et al.* (Kalb(Gilboa) *et al.*, 2001) took this to new limits with the 50 kDa case of glucose bound concanavalin A with a cubic unit cell repeat of 167 Å. The large incoherent background inherent to Laue diffraction is greatly ameliorated by perdeuteration, and recent work has shown that it is possible to collect high resolution data (~2.2 Å) from small (0.14 mm^3) crystals, although spatial overlap of reflections at the detector limits application with unit cells > 100 Å. BIX3 (Tanaka *et al.*, 2002) at JAERI, by using monochromatic neutrons, enabled diffraction studies on locating hydrogen and hydration in several proteins and nucleic acids (Niimura *et al.*, 1997; Niimura, 1999a). Although the background is much smaller than that at LADI, thus enhancing the signal-to-noise (Tanaka *et al.*, 2002), the low flux at BIX3 limits studies on crystals with large unit cells.

The PCS instrument at the Los Alamos Neutron Science Center (LANSCE) is the only instrument currently operating in the U.S.A. for NMC. The time-of-flight wavelength resolved Laue diffraction technique employed at PCS (Langan *et al.*, 2004) offers indisputable advantages over the conventional Laue method at LADI in using a

large wavelength band (0.7 - 7 Å) and spreading the diffraction peaks as well as the background into a large number of wavelength channels. This has enabled diffraction data to be collected for D-xylose isomerase (Hanson *et al.*, 2004), with an I-centered unit cell of dimensions 94 x 99 x 103 Å, which is one of the largest systems addressed to date by NMC at high resolution (~2.0 Å). Recognition in the scientific community of the unique information obtainable with NMC has already resulted in oversubscription factors of greater than two on neutron instruments worldwide and greater than three for the LANSCE PCS instrument. Higher flux is required for studies on crystals of smaller volumes and larger unit cells (>100 Å) at resolution in the range of 1.5 Å. Thus, there is an urgent need for powerful high resolution diffractometers for NMC.

With the advent of the Spallation Neutron Source (SNS) at Oak Ridge National Laboratory, an excellent opportunity exists for the development of a powerful high resolution neutron diffractometer for structural biology. SNS will produce more than an order of magnitude higher intensity than the Los Alamos facility, and the opportunity exists at SNS to design a fully optimized diffractometer for NMC. Furthermore cryogenic moderators, state-of-the-art neutron guides, and high sensitivity, high resolution detectors should allow additional factors of increased data rates and improved resolution to be realized.

Here we propose to develop a dedicated, best-in-class and high resolution time-of-flight single crystal macromolecular neutron diffractometer (*MaNDi*) at the SNS high power target station (HPTS), which operates at 60 Hz. Design calculations, using analytical expressions and Monte Carlo simulations, show that the data rates at the *MaNDi* instrument can be over 50 times greater than at PCS. Thus, it should be possible to investigate larger unit cell systems at high resolution, using smaller crystals. It is expected that the unprecedented, high data rates and resolution with *MaNDi* will revolutionize NMC and greatly advance the field of structural biology.

1.2 Protein Data Bank Statistics of Macromolecules Amenable to Neutron Diffraction Analysis -- The Impact of *MaNDi*

The completion of the human genome project has ushered in the eras of functional genomics, proteomics, and structural genomics. The unifying theme of these fields is focused on structure-function relationships, which is a well-accepted hypothesis in modern biology, biochemistry, and biophysics. Structural biology is currently experiencing unprecedented growth as a field, and it will continue to grow over the next decade due to new projects, initiatives, and developments in structural genomics worldwide. Macromolecular X-ray crystallography and NMR spectroscopy will continue to play major roles in the determination of new macromolecular structures as well as in structures of macromolecule-ligand complexes. However, neutron macromolecular crystallography can fill an important niche in structural and functional genomics that X-ray crystallography and NMR spectroscopy cannot adequately fulfill.

Solution nuclear magnetic resonance (NMR) spectroscopy is a complementary experimental technique with neutron diffraction. Both techniques have the ability to

identify the locations of protons and water molecules, which are essential for detailed physico-chemical studies of enzymes, proteins, and nucleic acids. However, because of the nature of polarization transfer that is so essential to NMR, characterization of protonation states of carboxyl and hydroxyl containing amino acid side chains is problematic (Qin *et al.*, 1996). In addition, water molecules bound to macromolecules are detected by NMR through the effect of bulk solvent on amide nitrogen magnetization, thereby localizing the water (Mori *et al.*, 1996a; Mori *et al.*, 1996b; Hwang *et al.*, 1997; Hwang *et al.*, 1998). Consequently, essential water molecules such as those involved in catalysis that are not coordinated with amide groups are difficult to detect by solution NMR. Finally, one of the strengths of NMR is its ability to characterize protein dynamics (Palmer *et al.*, 2001; Kempf & Loria, 2002). The nature of protein motion often results in broadened NMR resonance lines thereby lowering the signal-to-noise of the experiment. In some cases this loss of sensitivity makes interesting resonances difficult to detect. Neutron diffraction does not suffer from these limitations as it directly detects the location of protons and not via indirect effects as done in NMR.

Macromolecular X-ray crystallography will continue to be the front runner in the determination of new structures. Currently, X-ray crystal structures account for over 80% of the structures deposited in the PDB. In the late 1990's, with the advent of third-generation synchrotron sources, it was envisioned that ultra-high resolution, i.e. 0.5 Å to 1.1 Å, X-ray structures would provide detailed information on the positions of individual hydrogen atoms in the active sites of enzymes. However, this hypothesis has not been fully realized since not all hydrogen atoms in these structures could be identified, especially within the active sites. Since only about one percent (244 out of 21,233) of the X-ray structures in the PDB have been determined to 1.1 Å resolution (see Figure 1.2-1), it is clear that the vast majority of macromolecules cannot be studied by ultra-high resolution X-ray diffraction. In addition, since the majority of proteins have sizes that are beyond the optimal sizes to be studied by NMR spectroscopy, it will be virtually impossible to identify the hydrogen atoms involved in the catalytic mechanisms for the vast majority of large macromolecules.

Neutron diffraction has been shown to be reliable at locating hydrogen atoms at resolutions as low as 2.4 Å. As of July, 2004, 72.2% of all X-ray structures deposited (16,25, out of 21,233) have been determined to better than 2.4 Å resolution (see Figure 1.2-1). These resolution statistics suggest that the majority of structures in the PDB have the potential for study by macromolecular neutron crystallography under appropriate circumstances, including growth of protein crystals of sufficient size and being able to collect high resolution diffraction data at a neutron source that has beamline(s) optimized for collecting data on large macromolecules.

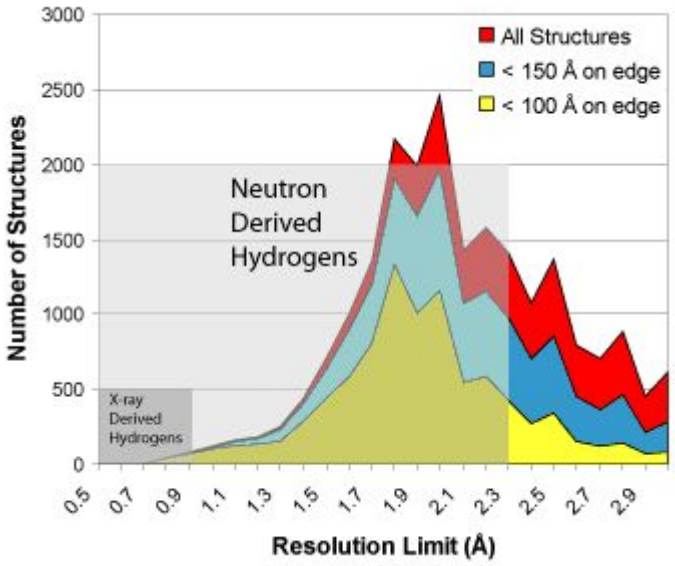

Figure 1.2-1. Protein Data Bank Statistics (July, 2004) on the number of structures determined within a given resolution range. The data range for the resolution limits are shown in 0.1 Å increments starting from 0.5 Å and ending at 3.1 Å. The structures with all unit cell edge lengths less than 100 Å are shown in yellow, and all structures with all unit cell edge lengths less than or equal to 150 Å are indicated in blue. All structures in the PDB are indicated in red.

Some of the considerations in the design of *MaNDi* include; 1) the molecular weight of the macromolecule that can be studied, 2) the unit cell dimensions of the crystalline samples, and 3) the maximal resolution for data collection that is attainable for individual samples. To date, most of the *completed* neutron diffraction structures deposited in the Protein Data Bank have been determined to between 1.5 to 2.4 Å resolution, and on crystals of proteins with molecular weights less than 35,000 Da and with unit cell edge lengths less than 90 Å in the longest dimension (Table 1.2-1). Most of the examples listed in Table 1.2-1 include proteins that have been studied intensively for well over a decade for a variety of reasons including that they are small proteins, they have small unit cells, they readily produce crystals with dimensions greater than 1 or 2 mm^3, and their crystals diffract X-rays to very high resolution. However, the neutron structures listed in Table 1.2-1, and the additional five neutron structures deposited in the PDB prior to 1990, represent a very small fraction of the total spectrum of proteins in the PDB that are amenable to neutron diffraction studies. One of the reasons for this paucity in the number of protein structures determined by neutron diffraction is that there are very few neutron sources worldwide that are available for macromolecular neutron diffraction. Moreover the currently available neutron sources are not optimized to collect high resolution neutron diffraction data on macromolecules with molecular weights well beyond 35,000 Da.

Table 1.2-1. Published and Unpublished Neutron Diffraction Structures of Proteins Since 1990

Protein Molecular Weight, Da	**Resolution Limit (Å)**	**a (Å)**	**b (Å)**	**c (Å)**	**β**	**Year**
[1]D-Xylose Isomerase **43,227**	2.5	94	100	104		2003, Preliminary results
[2]D-Xylose Isomerase **43,227**	2.2	94	100	104		2004, In preparation
[2]*trp* repressor **11,546**	2.1	53.6	53.3	32.7		2003
[3]Rubredoxin **5,841**	1.6	34.3	35.3	44.2		2003
[2]Rubredoxin **5,841 (@14 Kelvin)**	1.7	34.3	35.3	44.2		2004, In preparation
[3]Myoglobin **17,184**	1.5	64.5	30.9	34.9	105.9°	2002-03
[2]Endothiapepsin **33,615**	2.1	43.1	75.7	42.9	97.0°	2001
[4]Myoglobin **17,184**	2.0	64.5	30.9	34.8	105.8°	2000
[2]Concanavalin **25,583**	2.4	89.1	87.5	63.2		2000
[2]Concanavalin **25,583 (@14 Kelvin)**	2.4	89.1	87.5	63.2		2004, Submitted
[2,5]Concanavalin **51,166** (2 x 25583 in the asymmetric unit)	~4.0	167.8	167.8	167.8		Unpublished
[2]Ferritin	3.2	183	183	183		Unpublished
[2]Lysozyme **14,296**	1.9	27.3	32.0	34.2	108.8° α=88.8° γ=111.6°	1999
[2]Lysozyme **14,296**	2.0	80.8	80.8	37.1		1997
[2]Lysozyme **14,296**	2.1	28.0	62.9	60.3	90.7	2001
Crambin **4743**	1.1	41.01	18.69	22.64	90.65	Unpublished

[1]Data collected at the PCS at LANSCE, Los Alamos National Laboratory.
[2]Data collected on the LADI instrument, Institute Laue Langevin
[3]Data collected at BIX-3 at the JRR-3M Reactor at the JAERI.
[4]Data collected at the High Flux Beam Reactor at Brookhaven National Laboratory
[5]Unpublished data from John Helliwell. No structure determined.

On the other hand, the proposed *MaNDi* instrument has been designed and optimized to collect high resolution neutron diffraction data on the vast majority of potential macromolecules likely to be encountered by the user community. Our analysis of the PDB statistics indicates that about 82% (13,270 out of 16,252) of all X-ray structures deposited in the PDB that have been determined to better than 2.4 Å have unit cell edge lengths that are less than or equal to 150 Å in all three dimensions. In contrast,

only 49% (7,995 out of 16,252) of the X-ray structures determined to better than 2.4 Å have unit cell edge lengths that are less than 100 Å in all three dimensions. Since most of the current neutron diffractometers have difficulty in collecting data on crystals with unit cell edges above 90 to 100 Å, *MaNDi* has been designed to collect neutron data on crystals with unit cell dimensions up to 150 Å in all three unit cell dimensions. Moreover, *MaNDi* will have the ability to collect lower resolution neutron diffraction data (~2.5 to 3 Å) on larger unit cells, up to 250 to 300 Å. Based on these figures, the *MaNDi* design can theoretically accommodate over 80% of all proteins being studied by X-ray crystallography, which is an increase of over 65% of the number of proteins that can be studied by at currently available neutron sources. Therefore, *MaNDi* will be able to make a significant impact on our ability to analyze macromolecular structures by neutron diffraction.

1.3 Status of NMC Facilities in the United States

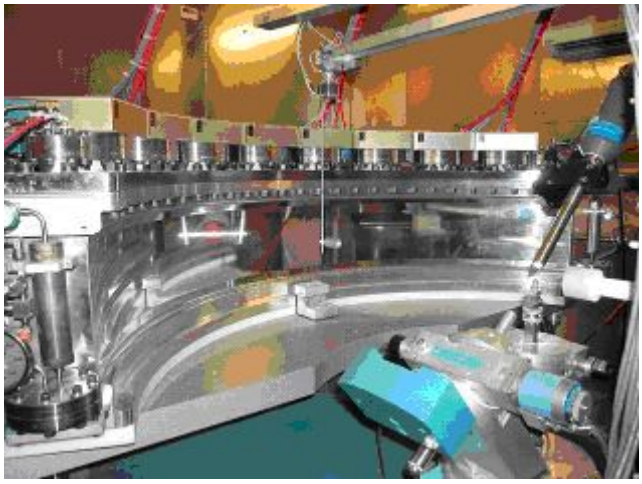

Figure 1.3-1. The area detector and the κ goniometer at the PCS.

The Protein Crystallography Station (PCS) at Los Alamos National Laboratory provides a much-needed facility for the U.S. structural biology community. It demonstrates the use of spallation rather than reactor neutron sources for NMC. There is little prospect of any large increase in the flux of existing reactor neutron sources in the United States because of inherent limitations (mainly cooling) in the fission process. However at a spallation source there are fewer flux limitations. Neutrons are produced by bombarding a metal target with pulses of high-energy protons and then travel as a function of their energy so that neutrons of different energies are detected at different arrival times. By recording time-of-flight information, the corresponding wavelength of each neutron can be calculated. Time-of-flight techniques in combination with large electronic position sensitive detectors (Fig. 1.3-1) allow wavelength-resolved Laue patterns to be collected using all of the available, useful neutrons. The wavelength-resolved Laue technique has all of the advantages of the conventional Laue method, including rapid and efficient coverage of reciprocal space, but it does not suffer in the same way from reflection overlap and a build up of background.

Since August 2002 the PCS has been run as a user facility for the structural biology community (Langan *et al.*, 2004; Schoenborn & Langan, 2004). To date six full data sets and four partial data sets have been collected under the user program. Results of three experiments have been published (Hanson *et al.*, 2004; Li *et al.*, 2004; Schoenborn & Langan, 2004) and a number of manuscripts are in preparation.

The need for *MaNDi* is clearly indicated by the current oversubscription of available beam-time at PCS by a factor of between two and three. Furthermore, many crystals with sample volumes of <1 mm^3 have been tested on the PCS for which full data collection is beyond the feasibility limits. Thus, there are a large number of important proteins that crystallize to sizes too small for data collection on the PCS regardless of current plans to increase the efficiency of data collection. The proposed *MaNDi* instrument at SNS is necessary for the study of these proteins and to advance the NMC field.

2. Macromolecular Neutron Diffraction in Biology and Medicine

2.1 The Critical Role of Neutron Protein Crystallography at High Resolution for Modeling of Hydrogen Atoms, Water, and Discrete Disorder

Neutron crystallography at high resolution is critical to understanding protein structure and function for two key reasons. First, neutron crystallography at high resolution (higher than ~1.4 Å) makes it possible to accurately model protein and water discrete disorder, and disorder is related to protein function. Second, hydrogens on the protein and on water molecules can be visualized more readily by neutron than by X-ray diffraction, although the techniques are complementary. Hydrogens, which are best defined following discrete disorder modeling, can provide crucial information for enzyme mechanisms and protein/water dynamics.

How do we know discrete disorder is important? Protein dynamics are principally anharmonic, and thus their energy surface is rough. (Doster *et al.*, 1990) Kinetic parameters for myoglobin and bacteriorhodpsin are consistent with several states of almost equal energy and a multi-well potential energy surface. (Rasmussen *et al.*, 1992) Protein and water discrete disorder modeling, using high-resolution X-ray and neutron data, can define these stable states that contribute to protein function (see below).

On lowering the temperature, at 200 K protein function appears to cease (Austin *et al.*, 1975). Analysis of 1 Å X-ray models of crambin, a 4.7 kDa, hydrophobic protein, from 300 K to 100 K (Teeter, 2001) reveals a break in slope for vibrational factor (*B)* vs. *T* around 180 K. The sign of the slope for **water** vibrational factors changes to negative below 180 K due to the glassy nature of water. The same negative slope is seen for **discretely-disordered** but not for ordered atoms. Dynamics for water and discretely-disordered protein atoms are thus uniquely coupled, and this coupling is linked to the temperature at which proteins function.

Crambin structures at 0.54 Å resolution by X-ray and at 1.1 Å resolution by neutron diffraction reveal that discretely-disordered residues are **correlated**, both along the surface of the protein and buried within the protein. Figure 2.1-1 shows the same region of the protein (three residues on the surface each with two conforma-

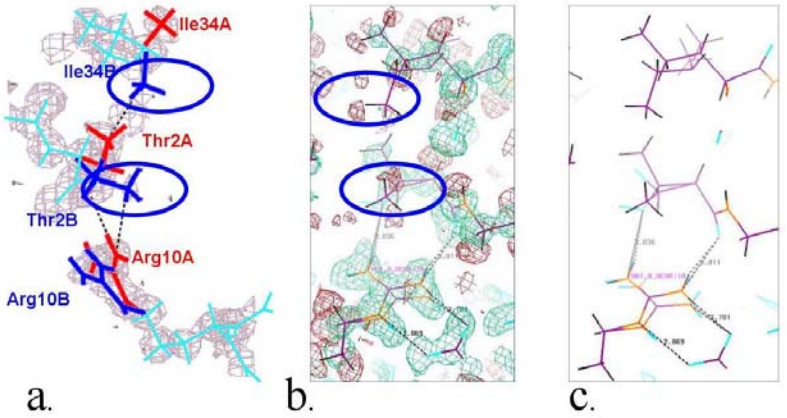

Figure 2.1-1. Correlated discrete disorder at the surface of crambin from a. X-ray and b. neutron. c. neutron key.

tions (red and blue for the X-ray) for the X-ray and neutron structures of crambin. The correlated nature of this disorder is apparent from the different occupancies of the two states of – 0.7 for one and 0.3 for the other, independently refined. Note in the blue ovals that the carbon density is much weaker for the B conformation. Figure 2.1-1c shows the neutron structure, omitting the scattering density for clarity.

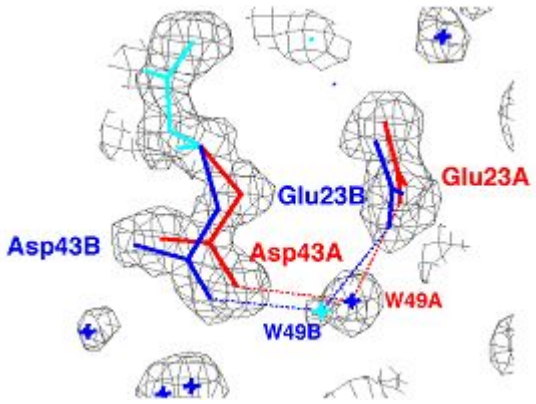

Figure 2.1-2. Discretely disordered water (49) connects A, B alternate conformations.

Along the protein surface, discretely-disordered water molecules connect protein residue states. Interestingly, this water connection can extend over tens of Å, suggesting that water stabilizes each kinetically observed state. Water 49 in Figure 2.1-2 has clearly-separated alternative positions depending on whether the A (red) or the B (blue) state for Asp 43 and Glu23 are present. Water deuterium atoms can be well-ordered or, as shown in Figure 2.1-2, statistically distributed.

Neutron protein crystallography determination of deuteriums, at around 2 Å resolution or better, matches that at 1.0 Å by synchrotron radiation X-rays due to the stronger signal of deuterium atoms in neutron diffraction. When the resolution of X-ray diffraction improves to values such as 0.6 Å for aldose reductase (Howard *et al.*, 2004) or 0.54 Å for crambin (Jelsch *et al.*, 2000), the valence electron density becomes discernible and the direct relation between the quantum mechnical orbital description and the observed protein atoms' orbital shapes is seen (Jelsch *et al.*, 2000; Afonine *et al.*, 2004). However, even in these cases, the mobility of hydrogens can abolish their X-ray diffraction signal (Figure 2.1-3), making neutron diffraction data desirable. Here the relative frequency of observation of hydrogen atoms in aldose reductase is plotted vs. the temperature factor of the bound heavy atom, which has been refined at subatomic resolution (0.66 Å). While most (90%) of the hydrogen atoms are observed for the very well ordered atoms (B~3 Å^2), the observations diminish linearly with increasing B-factor, and disappear when B is larger than ~ 16 Å^2. Therefore, the more mobile hydrogens for both the protein and the water

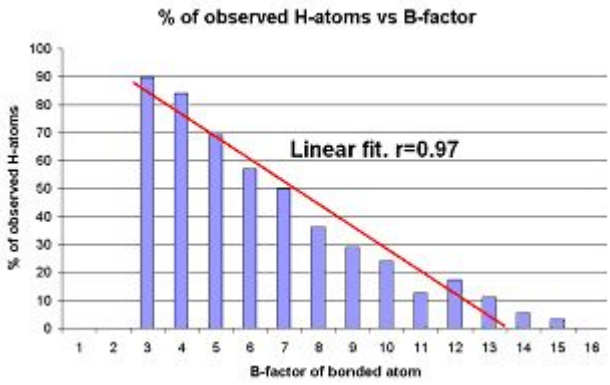

Figure 2.1-3. How the observation of hydrogen atoms depends on B-factor.

molecules are better determined by the neutron approach. Indeed, the bound solvent deuterium constitutes an entire category of deuterium atoms that are more efficiently sought by neutron techniques (Habash *et al.*, 2000). Figure 2.1-4 below shows that deuterium atoms for the Tyr 44 residue in the crambin structure and for hydrogen-bonded water are clearly visible. Note the contrast between the hydroxyl deuterium positive density (blue) and the tyrosine C-H hydrogen density (magenta).

The protonation state of amino acids could be determined in ultra-high resolution X-ray structures by analysis of bond lengths. As emphasized in Deacon *et al.* (Deacon *et al.*, 1997), with concanavalin A studied at 0.94 Å, the X-ray data-to-parameter ratio is around 5 whereas at 1.2 Å it is around 2. Dictionary restraints add "data" for refinement, making an overall X-ray + restraints data-to-parameter ratio of ~6 at 0.94 Å, and ~3 at 1.2 Å. However, certain dictionary restraints assume protonation states, *e.g.,* for carboxyl side chains. At a resolution of 0.9 Å (or higher), X-ray data can dominate the dictionary restraints, *i.e.*, for ordered carboxyl side chains. The dictionary restraints cannot be removed entirely, because some individual atoms or groups of atoms (such as on loops on the protein), where discrete disorder cannot be modeled, are sufficiently mobile that they diffract relatively more weakly at high resolution even if overall the diffraction extends to 0.9 Å. The dictionary structure restraints are thus essential to retain a proper overall geometry. This can introduce a slight error in bond distances in the ordered parts of the structure, but such errors are easily quantified in a separate refinement run with the restraints removed (Deacon *et al.*, 1997). These complications in restraints for refinement make neutron diffraction data, even at 1.4 – 2 Å resolution, very valuable for determining protonation states which are so important to enzyme mechanisms.

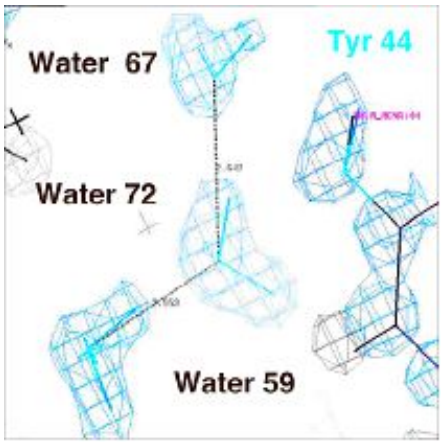

Figure 2.1-4. Water deuterium atoms are clearly visible by neutron diffraction of crambin.

In summary, neutron protein crystallography is very important for both discrete-disorder modeling and for determination of hydrogen position in solvent and protein, including protonation state. Even ultra-high resolution protein X-ray structures suffer from problems due to the weak diffraction of hydrogen and the difficulties in modeling mobile parts of the structure. A more accurate definition of hydrogen and deuterium atom positions in the protein and in water is invaluable for understanding protein structure and function.

2.2 Impact of Neutron Diffraction in Enzymology

2.2.1 Introduction.

The systematic application of neutron diffraction to identify the critical hydrogen atoms involved in the catalytic processes of enzyme systems promises to significantly enhance our understanding of the mechanism of enzyme action. Enzyme reaction mechanisms most often involve a series of chemical steps that transfer multiple protons either from or to acidic and basic amino acid residues. Steady-state and pre-steady-state kinetic studies can provide valuable information on the individual reaction rates for the chemical steps as well as the pKa's of amino acids involved in the proton transfer reactions and in substrate binding. Deuterium and tritium solvent isotope effects can provide valuable information on the approximate number of solvent derived protons transferred during the transition state of the reaction(s). High resolution X-ray crystal structures can provide atomic resolution, three-dimensional details of the amino acids and solvent molecules that are in positions to act as acids or bases, as well as those amino acid residues involved in substrate binding.

Unfortunately, it is extremely difficult to assign the protonation states of individual amino acids at active sites via kinetic studies and/or high-resolution X-ray crystallographic studies. In the late 1990's, with the advent of third-generation synchrotron sources, it was envisioned that ultra-high resolution, *i.e.*, 0.5 Å to 1.0 Å, X-ray structures would provide detailed information on the positions of individual hydrogen atoms in the active sites of enzymes. However, this hypothesis has not been fully realized. In the limited number, *i.e.*, 82, of X-ray structures determined within this resolution range, a number of the hydrogen atoms could not be identified in the active sites or ligand binding sites of the enzymes. Since less than 0.5% of all macromolecular structures reported in the Protein Data Bank are amenable to ultra-high resolution X-ray structure determination, it is clear that that the vast majority of enzyme systems cannot be studied by ultra-high resolution X-ray diffraction, and this implies that it will be virtually impossible to identify hydrogen atoms involved in the catalytic mechanisms.

Neutron diffraction studies, on the other hand, can be used on a much larger number of enzymes to obtain atomic resolution details of individual hydrogen atoms. Since neutron diffraction data determined within the resolution range of 1.5 Å to 2.4 Å can be used to identify individual hydrogens and deuterons in enzymes, over 80% of all macromolecular X-ray structures deposited in the PDB are amenable to neutron diffraction studies using *MaNDi*. The potential for studying a vast majority of enzyme systems via neutron diffraction could engender a renaissance in enzymology. For instance, structures determined by neutron diffraction could greatly aid in the determination of the individual protonation and ionization states of amino acid residues in enzyme active sites. Such data are crucial for correctly assigning the atomic charges and pK_a values of amino acids, and for reliably establishing those amino acids that are acting as acids and/or bases in the mechanism.

2.2.2 **Endothiapepsin**.

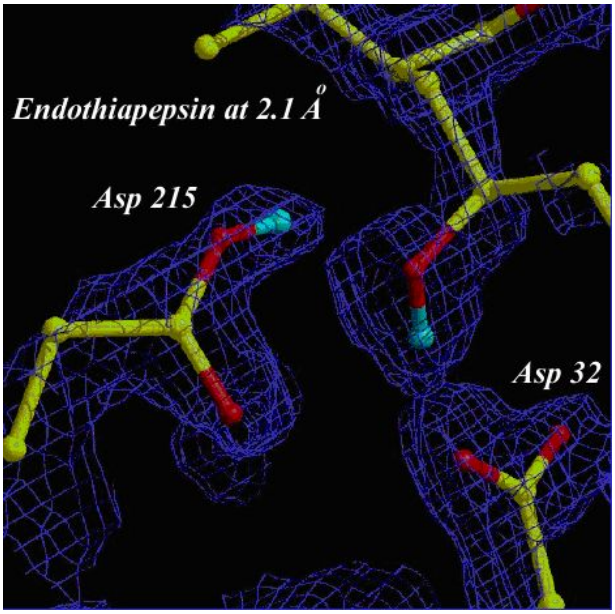

Figure 2.2-1. Neutron density at the active site of endothiapepsin showing Asp 32 to be deprotonated while Asp 215 is clearly protonated, Coates et al. (2001). Hydrogen atoms are shown in light blue.

Evidence for the catalytic mechanism of aspartic proteases, *e.g.*, endothiapepsin and HIV protease, is largely based on X-ray structures of bound peptide inhibitors containing non-hydrolyzable analogs of the peptide bond that is cleaved during catalysis. However, the positions of the hydrogen atoms on the catalytic aspartic acid residues (*e.g.*, endathiapepsin residues Asp 32 and Asp 215), on the inhibitors and on the other active site residues have not been determined with any certainty. Atomic resolution X-ray data could, in principle, resolve this problem. For instance, there should be a significant difference between the C–OH and C=O bond lengths (1.3 Å for the C–OH bond and 1.2 Å for the C=O bond) in neutral carboxylic acids, whereas ionized carboxylates are expected to have identical C–O bond lengths (about 1.25 Å) due to resonance. High resolution X-ray studies of endothiapepsin, using unrestrained refinement of the X-ray data to 0.9 Å, have shown that it is almost impossible to distinguish between COOH or COO^- in either of the two aspartate groups at the catalytic center since all four C–O bond lengths refined to almost identical values (P. Erskine, unpublished observations) (Tsyba & Bau, 2002).

On the other hand, in a neutron diffraction study of endothiapepsin in complex with an inhibitor at a resolution of 2.1 Å, convincing evidence that Asp 215 is protonated while Asp 32 is negatively charged in a transition state complex was provided from Quasi-Laue neutron data collected on the LADI instrument at the ILL (Coates *et al.*, 2001). A neutron density map showing the protonation states of Asp 32 and Asp 215 is shown in Figure 2.2-1, and the results confirm the earlier proposed catalytic mechanism by Veerapandian *et al.* (Veerapandian *et al.*, 1992). The structure determination of endothiapepsin represents the largest protein structure (330 residues) studied and published to date by neutron crystallography at moderately high resolution (2.1 Å).

2.2.3 Xylose Isomerase

The enzyme xylose isomerase represents another example of an enzyme where ultra-high resolution X-ray data are available, yet the protonation states of the amino acids at the active site are uncertain. D-xylose isomerase (XI) catalyzes the conversion of D-xylose to D-xylulose and D-glucose to D-fructose by transferring a hydrogen atom from one carbon atom to an adjacent carbon atom in a sugar molecule. XI has significant commercial impact in the production of high-fructose corn syrup, but, more importantly, it serves as a model for biochemical structure and function studies of metalloenzymes.

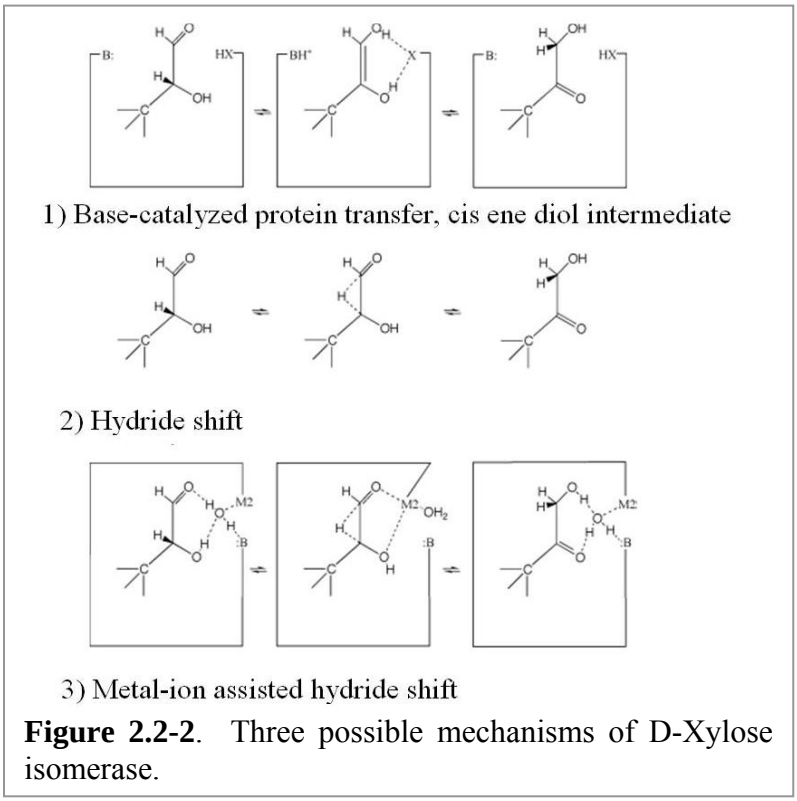

Figure 2.2-2. Three possible mechanisms of D-Xylose isomerase.

Three possible mechanisms have been proposed for the transfer of the hydrogen atom within the sugar substrate (Figure 2.2-2). However, despite years of intense scrutiny using atomic-resolution X-ray diffraction, a conclusive determination of the mechanism that initiates hydrogen transfer in this enzyme is still needed. The mode of action of this enzyme currently appears to involve an attack on the substrate by a hydrogen ion from a water molecule bound to one of two active site metal cations. The XI enzyme binds two divalent metal ions (M1 and M2) 4.9 Å apart, and

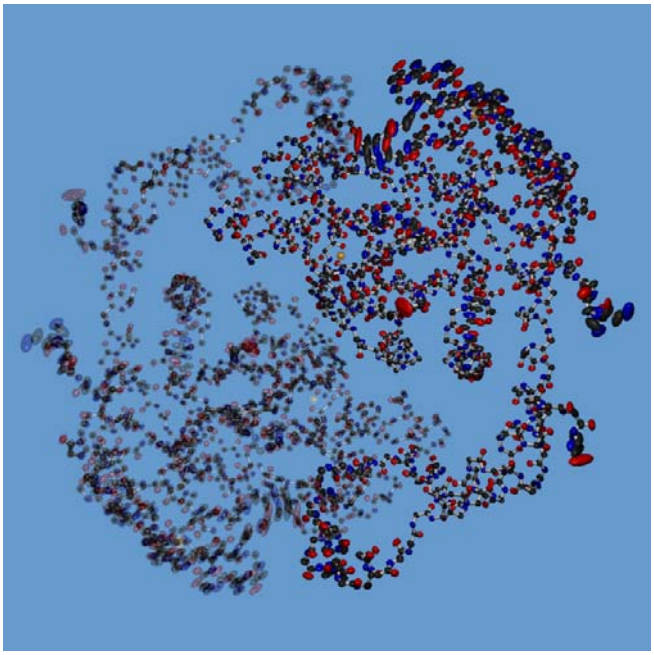

Figure 2.2-3. Overall structure of D-xylose isomerase at 0.86 Å resolution with ellipsoids showing anisotropic B-factors on one monomer (Ringe and Petsko, unpublished data).

the water molecule is bound to M2. A histidine group acts as a base that assists in opening the sugar ring system in the initial stages of the mechanism. The proposed mechanisms involve a *cis* ene-diol intermediate (Rose *et al.*, 1969), a hydride-shift mechanism (Farber *et al.*, 1989; Collyer *et al.*, 1990), or a hydride shift mediated by the metal ions (Whitlow *et al.*, 1991). The mechanism with a *cis* ene-diol intermediate is analogous to that in other enzymes catalyzing the same reaction but lacking metal ions. The hydride-shift mechanism involves a transfer of the hydrogen atom without any intervention from neighboring side chains in the active site. The metal ion-assisted hydride-shift mechanism includes some movement of the M2 metal ion. A second site for this metal ion has been observed in some crystal-structure determinations (Lavie *et al.*, 1994). The binding of substrates and inhibitors to XI has also been studied by X-ray crystallographic techniques (Carrell *et al.*, 1989). Several different binding modes were identified. However, despite the wealth of X-ray diffraction studies, and the recent ultra-high resolution 0.86 Å X-ray structure determined by G. Petsko and D. Ringe (unpublished data, Figure 2.2-3), the catalytic mechanism of hydrogen atom transfer has not been established.

During the 2002 LANSCE run cycle, neutron diffraction data were collected at the PCS from a crystal of XI, see Figure 2.2-4 and (Hanson *et al.*, 2004). The protein molecular weight is 43 kDa, and the unit cell dimensions of the crystals in space group *I*222 are 94 x 100 x 104 $Å^3$. The neutron density map has been calculated using data between 5 and 2.5 Å resolution, and the structure is currently being refined.

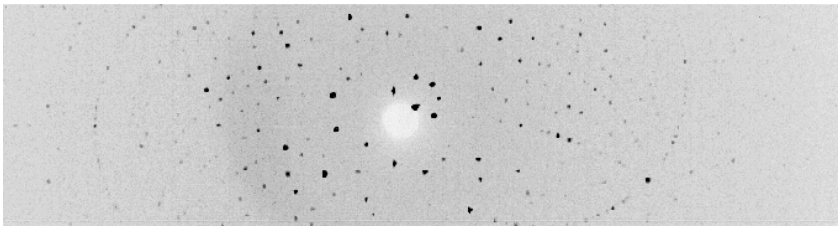

Figure 2.2-4. A quasi-Laue image showing Bragg reflections from D-xylose isomerase at the PCS. The image is a composite of several time channels. The diffraction is binned into 96 time channels covering the wavelength range from 1 to 5 Å.

2.2.4 Enzymes in Development for Neutron Diffraction Studies

A few of the enzymes of scientific interest to the *MaNDi* IDT members, and currently under development for neutron diffraction studies, are listed in Table 2.2-1. These enzymes are the subject of controversy because their mechanisms involve either proton or hydride transfers, and the amino acid residues responsible for acid and base catalysis have not been identified. All but one of the enzymes listed in Table 2.2-1 have at least one unit cell edge dimension greater than 90 Å, and most have an edge length between 100 Å to 150 Å.

Crystals of most, if not all, of the enzyme systems listed in Table 2.2-1 can be grown with volumes greater than of 0.8 mm^3, and all of these enzyme systems produce

crystals that diffract beyond 2.0 Å. Two examples of enzyme systems currently under development for neutron diffraction are described below, as well as in other sections of this proposal. We have included these examples to illustrate the ambiguities in establishing the detailed mechanisms of these enzymes despite the wealth of structural, biochemical and kinetic data available for each enzyme.

Table 2.2-1. Examples of Proteins Proposed for Neutron Diffraction Studies by Some IDT Members Using *MaNDi*

Protein Molecular Weight, Da	**IDT Members**	**X-Ray Resol. (Å)**	**Space Group**	**a (Å)**	**b (Å)**	**c (Å)**	**β**	**Reference**
Isocitrate Dehydrogenase **45,756**	Mesecar	1.4 to 1.9	$P4_32_12$	103.9	103.9	150		(Mesecar *et al.*, 1997; Mesecar & Koshland, 2000b; Mesecar & Koshland, 2000a) and unpublished
Trihydroxytoluene Dioxygenase **69,490** (2 x 34,745 Da in asymmetric unit)	Mesecar	1.2 to 1.5	C2	130	80	76	111 ^{o}	unpublished
Phosphotriesterase **34,730**	Mesecar	1.7-1.9	$P3_121$	61	61	207		unpublished
Enolase **93,632** (2 x 46,816 in asymmetric unit)	Mesecar	1.8	C2	121.9	73.2	93.9	93.3	(Larsen *et al.*, 1996)
D-Xylose Isomerase **43,227**	Bunick, Hanson, Petsko & Ringe	0.86	I2 2 2	94	100	104		unpublished
Aminopeptidase **32,217**	Petsko & Ringe	1.20	$P6_122$	108.4	108.4	93.5		(Desmarais *et al.*, 2002)
Aldose-1-epimerase	Petsko & Ringe	1.40	$P2_12_12_1$	128	132	101		unpublished
Alcohol Dehydrogenase **79,430** (2 x 39,715 in asymmetric unit)	Ramaswamy & Plapp	1.13	P1	44.3	51.4	92.7	103^o α=88.8 ^{o} γ=111.6 ^{o}	(Rubach & Plapp, 2003b; Rubach & Plapp, 2003a)
TEM−1 β-Lactamase **28,862**	Shoichet	0.85	$P2_12_12_1$	41.3	61.6	89.2		(Minasov *et al.*, 2002)

2.2.5 Isocitrate Dehydrogenase

Isocitrate dehydrogenase (IDH) catalyzes an essential, energy-producing reaction in the TCA cycle of many organisms whereby NADPH and 2-ketoglutarate are produced from isocitrate and NADP. In *Mycobacterium tuberculosis*, regulation of the concentration of isocitrate is important for survival of the pathogen during its persistent state.

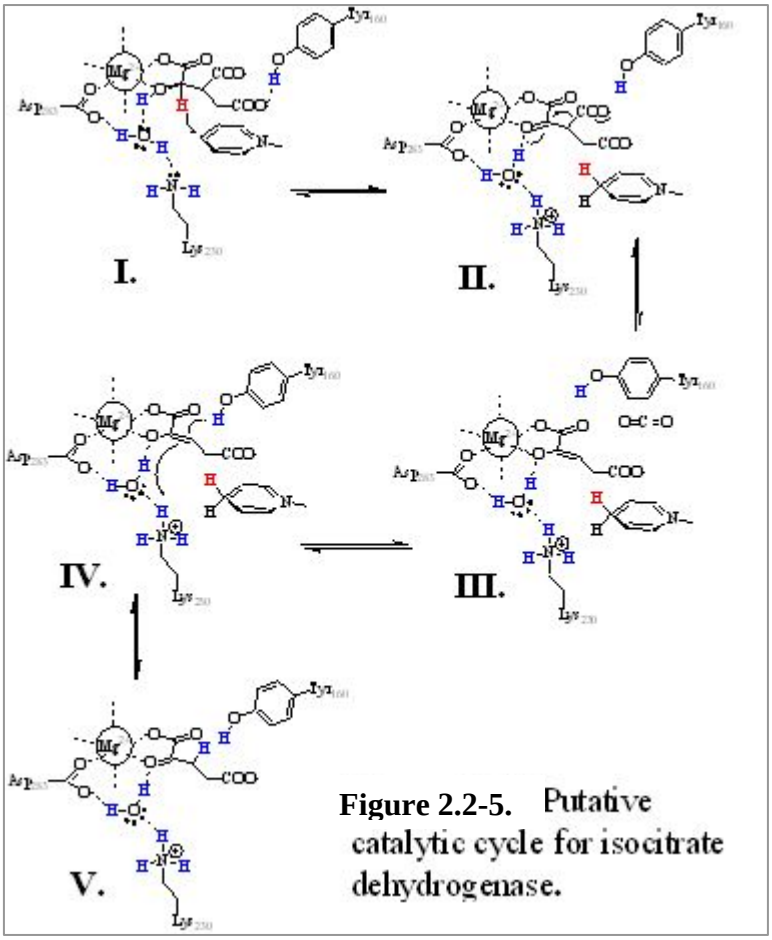

Figure 2.2-5. Putative catalytic cycle for isocitrate dehydrogenase.

The proposed reaction cycle for isocitrate dehydrogenase is shown in Figure 2.2-5. The reaction cycle is completed in approximately five steps (I- V) and involves the transfer of a number of putative, solvent derived protons (blue hydrogens) via a proton shuttle relay. From deuterium solvent kinetic isotope effects ($^{D}V_{max}$ ~4), we predict that at least two protons are in flight during the transition state. From a series of high-resolution X-ray crystallographic studies (Mesecar *et al.*, 1997; Mesecar & Koshland, 2000b; Mesecar & Koshland, 2000a), we have determined that a solvent molecule is involved in a relay mechanism with Lysine 230 and Aspartate 283. However, we have yet to establish the hydrogen positions of isocitrate, the active site amino acid residues or the water molecule involved in catalysis.

Our current hypothesis is that in the first part of the reaction cycle (I-II) Lysine 230 is atypically deprotonated at neutral pH so that it acts as a base and accepts protons from the hydroxyl group of the substrate via the water molecule. Once Lysine 230 is protonated, it may serve as an acid to transfer a proton to the enolate intermediate (IV) that forms immediately after decarboxylation (II-III). A second possibility is that the enolate (IV) could be protonated by the mobile amino acid residue Tyrosine 160. We wish to determine the neutron structures of the substrate and product bound states (I and V) in addition to the enolate bound state (III). We have synthesized a potent enolate analog that binds tightly to the enzyme form of IDH illustrated in (III) (Pirrung *et al.*, 1996), and we have determined the 1.7 Å structure of this intermediate (A. Mesecar,

unpublished data). Despite the fact that we are able to routinely determine 1.4 Å to 2.1 Å X-ray structures of IDH in a variety of complexes, we are still uncertain as to the positions of the hydrogen atoms. Since the reaction scheme of this enzyme potentially involves an atypical shuttle mechanism with an abnormally deprotonated lysine residue, we deem it necessary and important to pursue neutron diffraction studies to correctly establish or refute such a mechanism.

Isocitrate dehydrogenase crystals can be routinely grown between 0.8 mm - 1.2 mm in the longest dimension with square bipyramidal geometry (0.5 mm to 0.7 mm in the other dimensions). The crystals grow in the high symmetry tetragonal space group $P4_32_12$ with dimensions $a = b = 103$ Å and $c = 150$ Å and one molecule in the asymmetric unit. The crystals are catalytically active, and they can withstand prolonged exposure to monochromatic and polychromatic synchrotron X-rays (Bolduc *et al.*, 1995; Stoddard *et al.*, 1996; Stoddard, 1998; Stoddard *et al.*, 1998).

2.2.6 Trihydroxytoluene Dioxygenase (THTDO)

One of the most crucial reactions in the biodegradation of aromatic hydrocarbons involves the cleavage of aromatic carbon-carbon bonds. Aromatic ring-cleaving reactions are catalyzed by a class of enzymes known as non-heme metal(II) dioxygenases. These enzymes favor aromatic compounds that contain two vicinal hydroxyl groups (catechols) as substrates. Extradiol dioxygenases catalyze ring fission at bonds adjacent to one of the two hydroxyl groups. We are in the process of investigating the kinetic, chemical, and structural aspects of THTDO. To elucidate the mechanistic details of this proximal extradiol ring-cleaving enzyme, we have determined the high-resolution X-ray crystal structures of native THTDO to 1.4 Å and the enzyme complexed with 4-nitrocatechol (4NC), a potent inhibitor of THTDO, to 1.2 Å. The most notable difference between the two active sites is a lengthening of the Fe-O (water, *trans* to Glutamate271) bond from 2.08(2) Å in the native structure to 2.58(2) Å in the 4NC structure; this is the putative site for dioxygen binding. Examination of the active sites in these high-resolution structures suggests a modification of the currently accepted mechanism for extradiol enzymes. While it is generally proposed that the involvement of a single base (Histidine206) is necessary for catalysis, we propose that this Histidine206 acts instead as an *acid*, and that the base is more probably assigned as Tyrosine261 that is activated via a proton shuttle with

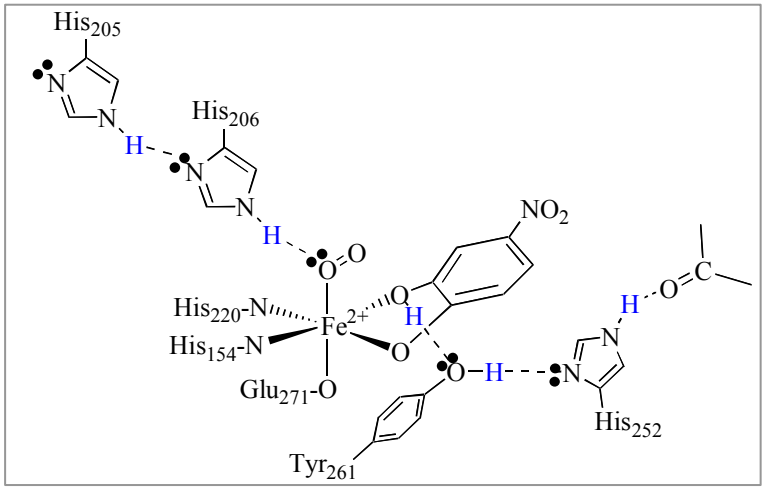

Figure 2.2-6. Putative Catalytic Cycle for THTDO.

Histidine252 (See Figure 2.2-6). The protons involved in acid and base catalysis and the associated proton relays are shown in blue.

Both structures crystallize in space group *C*2 with moderate unit cell parameters (*a* = 129 Å, *b* = 80 Å, *c* = 75 Å). The active site is composed of a mononuclear iron atom coordinated to His154, His220, and Glu271. The octahedral coordination around the iron atom is completed by water, catechol, acetate, or other oxo-ligands. It is crucial to determine the protonation state of the active site residues and ligands. We have generally been able to grow only moderately large crystals (400-900 microns), but they diffract well (beyond 1.2 Å) and are very stable. Despite such high-resolution X-ray structures, we are uncertain as to the protonation states of the amino acid residues in the active site of this important class of enzymes.

2.2.7 Summary

Neutron diffraction data on enzymes are critical for correctly assigning the atomic charges and pK_a values of amino acids, and for reliably establishing those amino acids that are acting as acids and/or bases in the mechanism. Moreover, neutron structures are necessary for identifying important water molecules and their hydrogen/deuterium atom positions and bonding patterns in active sites. Such data are crucial for our understanding as to whether water molecules are acting either directly as catalytic acids and bases, or rather are indirectly involved in acid-base catalysis via proton shuttle mechanisms. In addition, knowledge of the orientation of polar groups, *e.g.*, hydroxyls and amides, will enable researchers to identify detailed hydrogen bonding patterns between amino acid residues and water molecules in the interiors of the proteins as well as in the solvation shells surrounding the surface of the proteins. Accurate positions of hydrogen atoms will also help to determine the conformations of methyl groups and side chains and will provide details on amino acid packing arrangements. Accurate hydrogen atom positions derived from neutron diffraction data will provide important molecular details that will have significant impact on structure-based drug design, computational chemistry, protein dynamics, and on enzyme engineering studies. These research areas are on the forefront of biomedical research in the new millennium, and continued research in these areas utilizing neutron diffraction should positively impact public health.

2.3 Impact of Neutron Diffraction in Protein Dynamics Studies: Hydrogen/Deuterium Exchange

Because of their fundamental importance to the understanding of a broad range of biological processes, the dynamic properties of proteins have been the subject of intense investigation using a variety of methods. However, as more information is accumulated it is apparent that many of the most important issues remain concerning how the extent and nature of a protein's dynamical motions affect its function and folding.

Clarification of the details of the nature of protein fluctuations requires an experimental technique that can identify those segments of the polypeptide chain involved in transient motions. Since its introduction by Linderstrom-Lang and his colleagues in the 1950s, the hydrogen-deuterium exchange (H/D) method has been recognized to be a powerful probe for protein conformational change (Hvidt & Liderstromlang, 1954; Hvidt & Nielsen, 1966; Englander *et al.*, 1972; Englander *et al.*, 1980). This is because the H to D exchange rates of interior sites are found to differ by several orders of magnitude in an intact protein, providing a sensitive measure of the extent of shielding from the solvent provided at a given moment by the protein's secondary and tertiary structures (Hvidt & Nielsen, 1966; Englander *et al.*, 1972).

H/D exchange has advantages over other labeling techniques in that a deuteron has a negligible space requirement and has nearly equivalent chemical properties to the proton it replaces in the structure. Furthermore, potentially labile sites are distributed fairly uniformly throughout the molecule and therefore probe the structural variability of the whole molecule. Currently there are only two methods that can provide H/D data at high enough resolution to describe the exchange properties at the individual residue level, which is a requirement for a detailed dynamical analysis. One method is NMR, and it has considerable applicability for smaller proteins (generally <15-20 kDa). A more definitive approach for larger proteins is offered by neutron diffraction, which determines the location of each exchange site of the protein and permits the unambiguous characterization of its H/D exchange status by direct examination of the neutron scattering density map (Kossiakoff, 1982; Kossiakoff, 1983; Kossiakoff, 1995; Kachalova *et al.*, 1999). As can be seen in Figure 2.3-1, the task of assigning a site as having either H or D character is straightforward because the amplitude of H and D are of opposite signs. The practicality of using neutron diffraction for H/D analysis was first shown by Schoenborn and his colleagues (Schoenborn, 1975) and subsequently was verified by other investigators (Kossiakoff, 1983).

Although the number of H/D analyses by neutron diffraction is limited, a tremendous amount of unique structure-function information has been obtained (Schoenborn, 1972; Kossiakoff & Spencer, 1980; Kossiakoff & Spencer, 1981; Kossiakoff, 1983; Wlodawer & Sjölin, 1983; Phillips, 1984; Kossiakoff, 1988). Generally, it has been observed that surface accessible peptide groups exchange more rapidly than their buried counterparts. However, it has been shown that surface accessible peptide groups that are involved in β-sheet secondary structure motifs can be highly resistant to exchange, indicating that this type of hydrogen bonding organization is very stable (Kossiakoff, 1982). Figure 2.3-2 shows the overall H/D exchange pattern of the different secondary structure types in the proteolytic enzyme, trypsin. Interestingly, it was determined from the neutron analysis of subtilisin that the exchange patterns of β-sheets are found to be quite different between parallel and anti-parallel sheet motifs (Kossiakoff *et al.*, 1991). This suggests that the inherent breathing motions of these structural units are characteristically different, which had not been recognized until these studies. Additionally, neutron H/D data show that α-helix structures are much more prone to exchanging than β-sheets (both parallel and anti-parallel), indicating that they are inherently more flexible than either (Kossiakoff, 1982; Kossiakoff *et al.*, 1993).

The use of a crystallographic technique to study protein dynamics might appear at first glance to be inappropriate, because diffraction, by its very nature, constitutes a time-averaged sampling of the low-energy conformation of the molecule. Furthermore, there still exists some uneasiness about the degree to which the structures of crystallized proteins accurately represent protein structures in solution. H/D exchange data derived from neutron structures provide important insights into both these issues. Although H/D data provided by neutron diffraction are also time-averaged, the dynamic range of the technique still allows for the capture of a broad range of exchange rates in the diffraction experiment. While the shortest time ranges are inaccessible to the method (as is also true for NMR), the more important highly protected groups are easily distinguished. These highly protected groups provide the core for detailed analyses of properties that affect protein stability and breathing (Kossiakoff, 1982; Kossiakoff, 1983; Kossiakoff *et al.*, 1993). It is noteworthy that while the more buried peptide groups are generally most protected from exchange, there are a number that are deeply buried in the core of a protein and yet fully exchange (Kossiakoff, 1982). Likewise, buried exchangeable side chain groups like serine and tyrosine hydroxyl groups also are observed to exchange. These groups are seen to be totally inaccessible to solvent in the time-averaged structure, so that the fact that they exchange means that the crystallized protein molecule had to have undergone some rather large conformational fluctuations in the crystal lattice to facilitate the exchange of these groups. An extremely important conclusion from these findings is that even in a crystal lattice, protein molecules can undergo large conformational changes, a fact that clearly reduces the concerns that crystallized proteins are not good models for proteins in solution.

Although classical neutron Fourier maps have extremely high informational content about exchangeable groups and water structure, these analyses can be taken to an even higher level by employing D_2O-H_2O difference maps (Kossiakoff *et al.*, 1992). In practice, such maps are obtained by comparing the changes in diffracted intensities between two sets of data, one obtained from a crystal having H_2O as the major solvent constituent and a second where D_2O is the solvent medium. To a good approximation, the protein non-hydrogen atom contributions to the scattering intensities in both data sets are equal and cancel, but since H_2O and D_2O have very different scattering properties, their differences are accentuated to reveal an accurate and nearly unbiased representation of the solvent structure and the status of exchangeable groups (Figure 2.3-3). An additional advantage is that the features of a solvent difference map of this type are not as affected by errors in the phasing model as conventional difference maps (Shpungin & Kossiakoff, 1985; Kossiakoff *et al.*, 1992).

While these solvent maps have major advantages, the principal disadvantage is that they require an accurate high resolution H_2O data set. Due to problems associated with the incoherent scattering effects of H, such data sets are extremely difficult to obtain. This problem can be overcome with a higher flux neutron source such as SNS where it will be possible to acquire sufficient signal-to-noise improvements. This possibility has a transforming potential for obtaining a level of detailed information about

ordered water structure that is unavailable from other techniques even including ultra-high resolution X-ray structures.

H/D difference methods can also be used to obtain specific information at particular sites of covalently bound hydrogen if the sites in question can be deuterium labeled. Ligands bound to proteins provide a good example because the specific deuterium labeling is relatively straightforward. Difference analysis with data from labeled and unlabeled samples provides both positions and B-values of the deuterium labels, even if this part of the structure is disordered. The B-values, which provide a measure of the disorder, thermal or otherwise, can be obtained to better than 10% precision. This type of H/D analysis has been extensively applied to lipid bilayer structures (Worcester *et al.*, 1996). Diffraction studies for drug design could benefit greatly from such covalent H/D difference analysis.

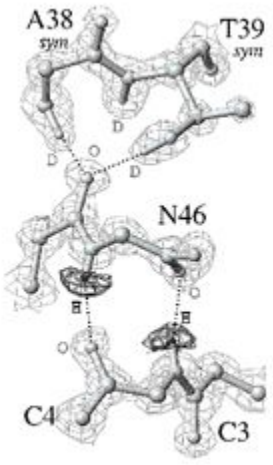

Figure 2.3-1. Fourier map showing the H/D exchange properties of a protein (amide peptide hydrogens (H) shown in dark contours, peptide deuteriums representing exchanged groups are designated as D). Peptide amide hydrogens in the secondary structure between C4 and N46 are protected from exchange. Conversely, peptide amide hydrogens of residues A38-T39 are fully exchanged. The crystal was soaked in D_2O for several months before data collection; thus those groups that remain unexchanged are highly protected.

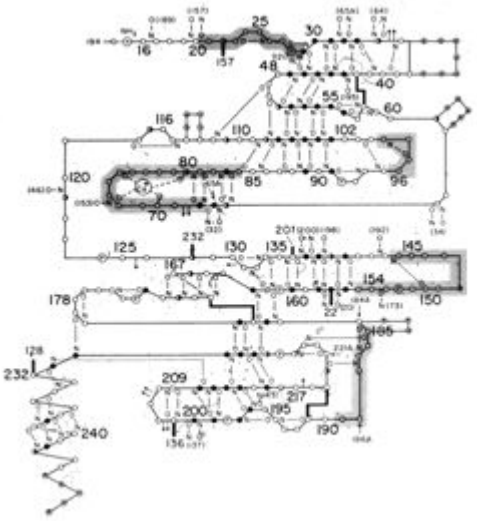

Figure 2.3-2. Schematic representation of exchange patterns in trypsin. Exchanged groups (D) are represented by open circles, unexchanged groups (H) by filled circles, and partially exchanged groups by half-filled circles.

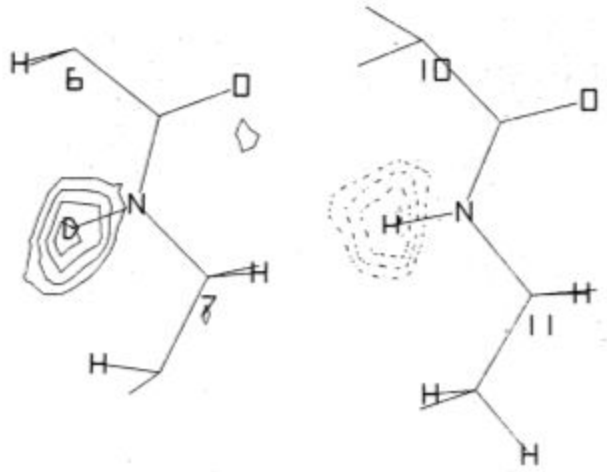

Figure 2.3-3. Sections of a neutron D_2O-H_2O difference map taken in the plane of the peptide group. On the left is a fully exchanged site, on the right is an unexchanged site. Note that all other density is zero. This is a characteristic of this type of map.

2.4 Impact of Neutron Diffraction in Membrane Protein Structural Studies

About 30% of all proteins are embedded into biological membranes. Membrane proteins are the major players in important cell processes including cell import and export, recognition, signaling, nerve function, respiration, and photosynthesis. Membrane proteins are therefore key targets for research on human health and drug

development. However, whereas more than 21,000 structures of soluble proteins are known, less than 40 different types of membrane protein structures have been determined to date.

The main impediment to the structure determination of membrane proteins is the challenge in growing crystals that can diffract to higher resolution. The membrane proteins are amphiphilic protein complexes. The membrane intrinsic central part of the protein complex is highly hydrophobic, whereas the loops connecting the hydrophobic α–helices or β-sheets on both sites of the membrane are hydrophilic and are exposed to the aqueous environment. Detergents must be used to extract membrane proteins in functional intact form from the membrane. The protein is solubilized in the form of a protein-detergent complex, where the hydrophobic membrane intrinsic part of the protein complex is surrounded by the detergent micelle like a swimming ring (see Fig. 2.4-1).

Many of the membrane proteins that have been crystallized to date are not single proteins but rather are large membrane protein complexes that contain several protein subunits and in some cases more than 100 cofactors. These large membrane protein complexes contain subunits that are membrane intrinsic as well as membrane extrinsic protein subunits that are responsible for the interaction with soluble proteins that dock to specific binding sites. The crystals of these large membrane proteins typically have very large unit cells with repeats of 100-300 Å.

Neutron diffraction experiments on membrane proteins can be used to further the following important specific aims:

1) To unravel the structure of the solvent and the detergent by means of low resolution neutron diffraction experiments.

2) To elucidate the structure of water channels, which are important for the catalytic mechanism of many membrane proteins.

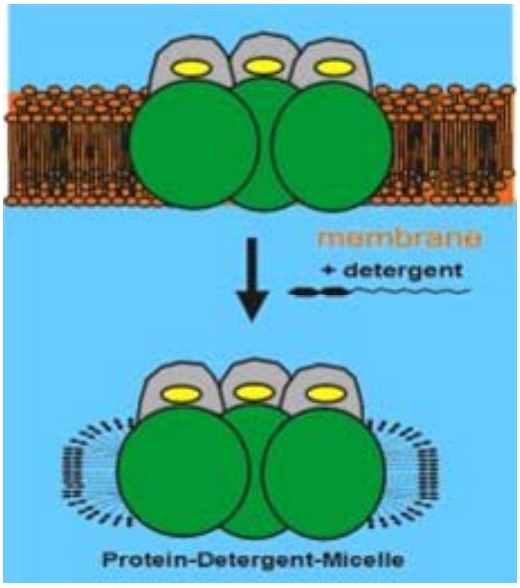

Figure 2.4-1. Schematic representation of the solubilization of a membrane protein in a detergent solution.

3) To unravel the catalytic mechanism of reactions involving water, as for example, the mechanism of water splitting and oxygen evolution in Photosystem II, by means of high-resolution neutron diffraction on membrane protein crystals.

The crystallization of membrane proteins is complicated, because they must be crystallized as detergent-protein complexes. The phase behavior of the detergent-protein solution is very complex, and there is currently a lack of knowledge about the nucleation and crystal growth processes. A description of the structure of the detergent within single crystals of membrane proteins will be essential for developing an understanding of the nucleation and crystallization mechanisms involved. Two models for the arrangement of detergent in membrane protein crystals can be found in text books: type I crystals, where the detergent should form a membrane-like structural arrangement similar to lamellar phases of detergent, and type II crystals where the detergent micelles are building blocks of the unit cell.

Low-resolution neutron diffraction experiments provide the best way to determine solvent and detergent structures within protein crystals (Roth *et al.*, 1991; Kossiakoff *et al.*, 1992; Pebay-Peyroula *et al.*, 1995; Badger, 1996). As a recent example, Snijder and coworkers determined the detergent organization in crystals of monomeric outer membrane phospholipase A (Snijder *et al.*, 2002). Also the detergent structure in crystals of the bacterial light-harvesting complex has been recently determined by Prince and coworkers (Prince *et al.*, 2003). These structures show a type II organization of the detergent, where the detergent micelles are the building blocks of the crystal and detergent-detergent interaction is important for crystal contact formation.

To address the question of the detergent structure within membrane-protein crystals in general, neutron diffraction experiments on a larger set of crystals of different membrane proteins with the *MaNDi* instrument will be vital. The aim of these neutron diffraction experiments should be to determine the detergent structure in a large number of different membrane protein crystals, with different crystal packing arrangements. Important questions to answer will include:

- How does the detergent participate in crystal formation?
- Can a lamellar detergent phase, mimicking the membrane, exist in the crystals?
- How is the solvent water arranged in the crystals?

With increasing knowledge on these important points, the process of crystal formation of membrane proteins will be unraveled, opening up the possibility of developing a rational design for the crystallization of membrane proteins.

Water and solvent channels play an important role in the function of membrane proteins. One of the most important examples is aquaporin, the protein that transports water across the membrane at a rate of 100,000 water molecules per second. The Nobel Prize in Chemistry for 2003 was awarded to Peter Agre for elucidating the structure and mechanism of this important channel protein, which is also of high medical relevance (Mitsuoka *et al.*, 1999; Agre *et al.*, 2002; Agre & Kozono, 2003). Based on the structure, Agre proposed a mechanism for water conductance through the channel and the exclusion of protons from being translocated. The mechanism was further supported by the crystal structure of the enzyme at 2.2 Å resolution (Sui *et al.*, 2001), but the orientation of the

water molecules could not be experimentally determined at this resolution by XMC (X-ray macromolecular crystallography). In X-ray structure analysis, the hydrogen atoms become visible only at resolution below 1 Å, whereas NMC (neutron macromolecular crystallography) at 2.2 Å should suffice to obtain the position of the hydrogen or deuterium atoms. Thus, NMC on membrane protein crystals like the aquaporin crystals may unravel the structure of the water channel at atomic detail and thereby make important contributions to confirm and extend the proposed mechanism of water translocation.

Aquaporin is not the only membrane protein complex where water plays an important role in the transport mechanism. Other known structures where NMC at *MaNDi* would promise to unravel important pathways in membrane proteins include

- Bacteriorhodopsin is a light driven proton pump, for which water plays a key role in the catalytic mechanism. Several structures of this enzyme, determined by XMC, agree on the main features of the protein fold, chromophore position, and amino acids. However, major points of discussion still remain on the positions of the water molecules, which are essential for the catalytic mechanism (Neutze *et al.*, 2002; Lanyi & Schobert, 2003; Schobert *et al.*, 2003; Shibata *et al.*, 2003).

- Three different water channels are postulated in the cytochrome oxidase complex (Olkhova *et al.*, 2004). Cytochrome oxidase is one of the key enzymes of the respiratory chain, catalyzing the reduction of oxygen to water. The water channels are thought to play a major role in the pumping of protons across the membrane.

- Photosystem II, the enzyme that produced all oxygen in Earth's atmosphere, is a further example where a water channel may be present in the enzyme to allow entry of substrate water to the catalytic site of water oxidation. Based upon the available medium resolution X-ray structures, so far it has not been possible to unravel the positions of the water molecules. Unraveling the details of the water channels in Photosystem II will be a major challenge for NMC at *MaNDi*.

The location of hydrogen atoms in the catalytic centers of proteins is one of the most important goals of NMC. As pointed out above, water and hydrogen atoms/protons play an important role in the function of membrane proteins. In some cases the water molecules are merely being transported, or they may function as a water chain of H-bonds for proton conductance. However, important catalytic reactions even involve water as a substrate or product.

Cytochrome oxidase catalyzes the electron transfer from cytochrome c to oxygen, thereby reducing 2 atoms of oxygen and 4 protons to form 2 molecules of water. Chemically, the reaction is the inverse reaction of that for PS II, but there exists no structural or functional homology between the cytochrome oxidase (which catalyses the exergonic reaction) and Photosystem II (performing the light driven endergonic reaction of water splitting). The reduction of oxygen by cytochrome oxidase represents the final

step in the reactions of the respiratory chain. Although the X-ray structure of the enzyme has been determined (Iwata *et al.*, 1995; Tsukihara *et al.*, 1996; Ostermeier *et al.*, 1997; Tsukihara *et al.*, 2003) recently to 1.7 Å resolution (Tsukihara *et al.*, 2003), the mechanism of the reaction is still debated. With high-resolution NMC, the protonation state of individual amino acids and cofactors could be unraveled, and this may solve several questions concerning the catalytic mechanism of the enzyme.

A much more challenging example in which important catalytic reactions are catalyzed by a large membrane protein complex, is Photosystem II. As mentioned above, Photosystem II is the enzyme that produces all oxygen in Earth's atmosphere. It catalyses the light driven transmembrane electron transfer from water to plastoquinone. Four electrons are subsequently extracted from the oxygen evolving complex and two oxygen atoms and four protons are released in the highly endergonic reaction of water splitting. The first step in unraveling the secrets of water splitting was the successful

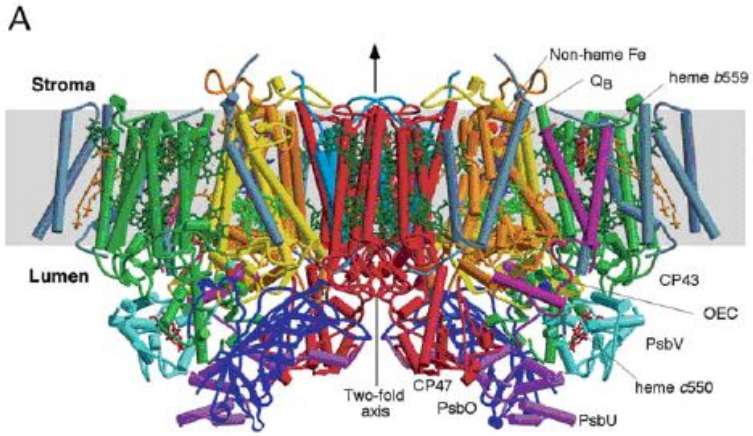

Figure 2.4-2. Structure of Photosystem II at 3.5 Å resolution (taken from Ferreira *et al.* 2004)

crystallization of Photosystem II (Zouni *et al.*, 2000; Zouni *et al.*, 2001) in an active oxygen evolving form. The structure of PS II at 3.8 Å resolution provided the first evidence for the location of the Mn cluster. This structure of PS II, and two further structures at slightly higher resolutions of 3.7 and 3.5 Å, allowed a first glimpse on the structure of the Mn cluster (Kamiya & Shen, 2003; Vasil'ev *et al.*, 2003; Ferreira *et al.*, 2004), see Fig. 2.4-2. However, neither the water molecules nor the protonation state of the amino acids have been determined so far, and for this reason none of these X-ray structures is sufficient to explain the mechanism of water splitting.

Whereas the X-ray structure must be improved to a resolution better than 3 Å to identify the oxygen atoms and better than 1 Å to identify the orientation of the water molecules, NMC would allow the identification of water molecules, including the hydrogen atoms, if the resolution limit could be extended to 2.5 Å resolution.

Another very exciting experiment would be the determination of the water structure in PS II in the different oxidation states of the Mn cluster. The crystals can be frozen and the water-oxidizing complex can be trapped in the different S-states (oxidation states) of the reaction. With XMC the investigation of the different S-states will be

difficult, because the strong interaction of the X-ray beam with the protein complex may change the oxidation state of the cluster. However, thermal neutrons will not perturb the protein crystal, and therefore the oxidation states of PS II would not be expected to change during collection of neutron diffraction data. By designing the *MaNDi* instrument to include the possibility for high resolution data collection on membrane proteins with large unit cells, it may become possible to visualize the water molecules bound to the cluster at atomic detail.

NMC may also determine the mechanism and pathway of the protons that are released during the catalytic cycle. A hypothesis exists that the redox active tyrosine may not only extract electrons but also hydrogen atoms from the Mn cluster. The unraveling of the mechanisms of water splitting by PS II would be an ultimate goal for neutron diffraction experiments. The essential point would be not only to obtain a static high resolution picture of the complex, but also to examine different oxidation states of the cluster, so that the whole catalytic cycle could then be visualized at atomic detail.

2.5 Impact of Neutron Diffraction in RNA and DNA Structural Studies

Nucleic acid conformation is dependent on sequence, relative humidity, and ionic strength. While sequence dependence and DNA water structure were at the center of many physical-chemical investigations over the past 25 years, comparatively little is known about the details of how metal cations, in particular alkali and alkaline earth metal ions, affect DNA conformation and packing. Improved techniques for analyzing DNA structure and environment in crystals and solution should help shed light on DNA-ion interactions in the coming years. Thus, crystal structures of DNA duplexes at high resolutions (< 1.2Å) have now emerged [reviewed in (Egli, 2002)], some revealing unprecedented details of the ionic environment of DNA. For example, atomic-resolution crystal structures of the Dickerson-Drew dodecamer (DDD) revealed the locations of five Mg^{2+} ions (Minasov *et al.*, 1999) and binding of an alkali metal ion to the ApT step in the minor groove (Figure 2.5-1A) (Tereshko *et al.*, 1999).

To study the possible effects of metal ions on DNA conformation, sequences can be divided into three principal groups: A-tracts, G-tracts, and generic DNA, where the latter represents the vast majority of DNA sequences (Hud & Plavec, 2003). A-tracts have an unusually narrow minor groove (Figure 2.5-1B, left), are straight, and have high base-pair propeller twist. G-tracts have a propensity to undergo the B-form → A-form transition at increased ionic strength. The proponents of the 'ions are dominant' model believe that the DNA grooves are flexible ionophores and that DNA duplex structure is modulated by a tug of war between the two grooves for cation localization. They argue that the duplex geometry adopted by A-tracts (referred to as B*-DNA; Figure 2.5-1B, right) is due to ion localization in the minor groove as a result of the highly negative electrostatic potentials there. Conversely, G-tract DNA exhibits a highly negative electrostatic potential in the major groove, leading to preferred localization of cations there and consequently to a collapse of the DNA around the ions. Generic DNA, on the other

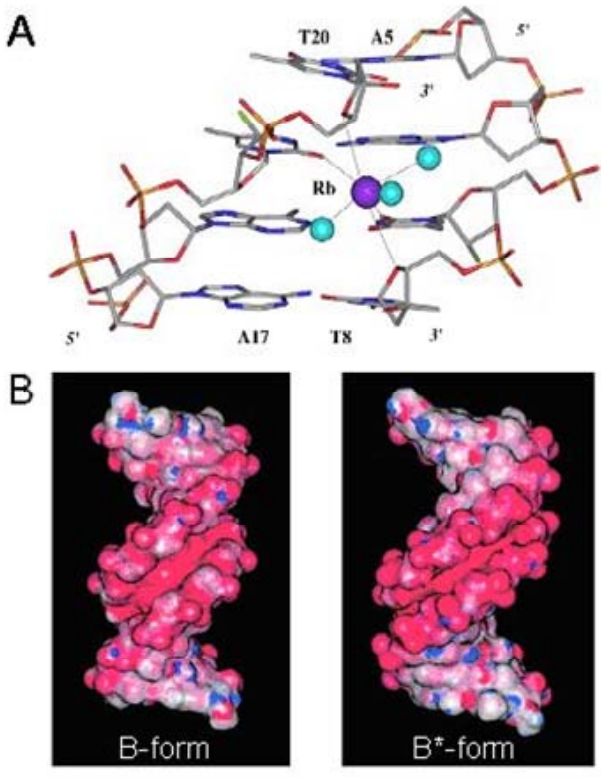

Figure 2.5-1. Metal ion binding and minor groove topology. (**A**) Coordination of an alkali metal cation at the central ApT step the DDD (Tereshko *et al*., 1999). (**B**) Narrowing of the minor groove in A-tract DNA (B*-DNA) and concomitant negative electrostatic polarization compared to generic B-DNA (Hud & Plavec, 2003).

hand, would have a more balanced occupation of its major and minor grooves by cations, consistent with a more or less canonical B-form geometry. By contrast, those who emphasize the dominating role of sequence in the control of DNA conformation argue that it is the sequence that shapes the DNA in the first place and that the narrow minor groove of A-tract or B*-DNA is narrow even before ions settle in the groove.

Neither experimental approaches using X-ray crystallography or solution NMR nor computational simulations have furnished a consistent picture regarding the individual contributions of sequence, negative backbone charges, and cations in the control of DNA topology and duplex groove widths. Reliable detection of cations, particularly Na^+, K^+ and NH_4^+, in experimental structures and correct parameterization of charges in simulations constitute current potential limitations (Tereshko *et al.*, 2001; Stellwagen & Mohanty, 2004). Although the 'ions first' hypothesis has a number of attractive features – *i.e.,* it provides a link between sequence-specific cation localization and sequence-directed curvature of DNA – it cannot be overlooked that high-resolution crystal structures of oligodeoxynucleotides containing A-tracts (stretches of As or Ts uninterrupted by a TpA step) have shown no variation of groove width as a consequence of different types and concentrations of alkali metal ions present in the crystallizations. Moreover, MD simulations of A-tract DNA in the presence of different classes and varying localizations of metal cations have not provided a picture that is consistent with a crucial role of metal ions with regard to the structure of duplex DNA. Thus, more studies need to be directed at the relative importance of sequence and cation coordination in governing the structure of double helical DNA.

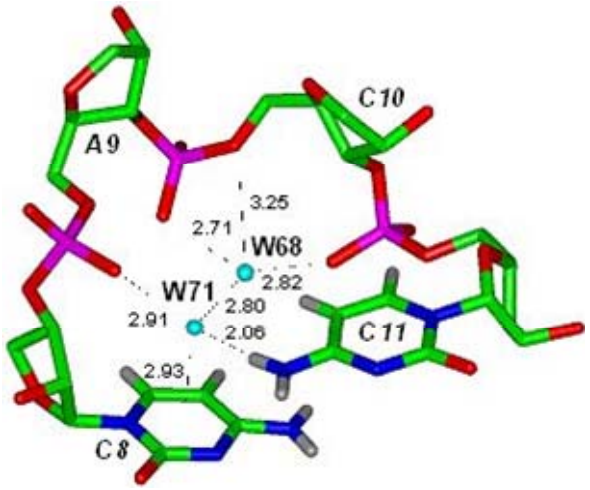

Figure 2.5-2. 'Stacking' interaction between water molecule W71 and the functionally important unstacked residue C8 in the 1.25 Å crystal structure of the ribosomal frameshifting RNA pseudoknot from Beet Western Yellow Virus. The distance of 2.93Å is indicative of a lone pair-π (*l.p.*–π) interaction. The possibility of the water hydrogen atom interacting with the π–face is unlikely because this would put the hydrogen at around 2Å from the cytosine ring centroid, a region that is sterically inaccessible. Furthermore, W71 is hydrogen bonded to the phosphate group of A9 and to W68; most likely the two hydrogens of W71 are used as donors in these. The existence of a *l.p.*–π interaction is also consistent with earlier evidence that proved C8 to be protonated at N(3).

In almost all X-ray crystal structures of nucleic acids, the cations that have been visualized along with DNA or RNA and water molecules account for neutralization of less than 50% of the negatively charged phosphate groups. NMC is expected to become a powerful tool for reliably discerning between light alkali metal ions and water molecules in crystal structures. It is likely that neutron diffraction can also shed light on the whereabouts of ions with low occupancy and thus furnish a more complete picture of the ionic environment of nucleic

acids in crystals. NMC will not only benefit crystallographic investigations of nucleic acids alone but will also be an important tool to analyze complexes between proteins and DNA and proteins and RNA. Metal ions are an important component of such complexes and can induce or stabilize particular conformational features of DNA that affect its interaction with the protein. One example is the binding of Mn^{2+} ions in the X-ray crystal structure of the nucleosome core particle at 1.9 Å resolution (Davey & Richmond, 2002). Here, manganese was used in place of magnesium to facilitate the detection of ions. This would expect to be a particularly powerful probe in NMC since manganese (like H) has a negative scattering factor and thus Mn^{2+} can very easily be distinguished from Mg^{2+}, Na^{+} or D_2O in the inter-molecular spaces of a crystal. In the nucleosome core, the specific location and mode of metal ion binding is the consequence of unambiguous conformational differences between dinucleotide sites owing to their sequence context and orientation. Although monovalent cations may play a less significant role in stabilizing simple nucleic acid duplexes than divalent ones, more complex architectures such as those encountered in complex folding motifs of RNA may be associated with specific coordination of monovalent ions, and NMC constitutes a unique tool for directly visualizing these binding sites.

One of the obvious advantages of neutron diffraction compared to X-ray diffraction data is that the protonation states of nucleobases and amino acid side chains can be firmly established with NMC. X-ray crystal structures at atomic resolution can provide detailed information on the structure of the solvent surrounding macromolecules in the crystal. However, even UHRXMC does not allow one to differentiate between the acceptor and the donor of a hydrogen bond between two water molecules. Occasionally it is possible to guess the role of a water molecule in a specific hydrogen bond from the identity and potential role of nearest neighbors of that water in solvent networks, particularly if the water belongs to the first or second hydration shell around a nucleic acid or protein molecule. Recently, an unusual type of a water-nucleobase 'stacking' interaction has been identified in the X-ray crystal structure of an RNA pseudoknot, where a water molecule sits directly above the six-membered ring of a cytosine base (Sarkhel *et al.*, 2003) (Figure 2.5-2). One would have intuitively concluded that it is the hydrogen of water molecule 71 that is directed into the aromatic ring of cytosine 8. However, closer inspection of the distances reveals that it is impossible to wedge a hydrogen atom between the water molecule and the cytosine plane, leaving only the possibility of an interaction between the electron lone pair and the nucleobase. NMC can firmly establish the existence of such interactions because this technique can distinguish between hydrogen and lone pairs.

2.6 Impact of Neutron Diffraction on Studies of Redox and Electron Transport Systems in Biology

Redox enzymes and electron transfer (ET) proteins are critical for proper metabolism. Redox enzymes are bifunctional in that they catalyze chemical reactions as well as participate in electron transfer. Such enzymes are required for the oxidation (degradation) of substrates during metabolism and the production of reducing equivalents (electrons) for energy production. The electrons that are extracted from substrates by redox enzymes are directed to specific sites to allow energy conservation via specific ET proteins. These redox processes are fundamental to respiration, photosynthesis, and reactions of intermediary metabolism. Redox proteins possess either metals or organic cofactors as redox centers. Many of these proteins exhibit pH-dependent redox properties. This is due to the protonation state of the organic cofactor or an amino acid residue that provides a ligand for the metal or a hydrogen bond to the cofactor. It has also been shown that rates of long range protein ET reactions may be regulated by or coupled to proton transfer reactions and reorganization of water (Davidson, 2000; Davidson, 2002). As such, precise knowledge of the positions of hydrogens and water molecules in the vicinity of the redox cofactor of a redox protein is critical to understand the roles of protonation state, H-bonds, and reorganization of water in controlling the reactivity of protein-bound redox centers. The methylamine dehydrogenase (MADH)-amicyanin-cytochrome *c*-551i complex has been established as a model for the study of redox properties of metal and organic cofactors and mechanisms of long range biological ET (Chen *et al.*, 1994a; Davidson, 2000; Davidson, 2002). Two specific examples from this system are described to illustrate the potential value of neutron diffraction in furthering our understanding of these fundamental processes.

Roles of H-bonds in regulating redox properties of metalloproteins. Amicyanin is a type I copper protein, for which the X-ray crystal structure has been determined to better than 1 Å resolution [(Cunane *et al.*, 1996) and unpublished]. Amicyanin mediates ET from a soluble dehydrogenase, MADH, which is a *c*-type cytochrome. The E_m value of amicyanin varies with pH and exhibits a pK_a value for the reduced form of 7.5. The crystal structure of reduced amicyanin at pH 4.4 reveals that His^{95}, which serves as a Cu^{2+} ligand, has rotated 180° about the C_β-C_γ bond relative to its position in oxidized amicyanin and is no longer in the copper coordination sphere (Zhu *et al.*, 1998) (Fig. 2.6-1). A similar phenomenon is observed with the plant copper protein

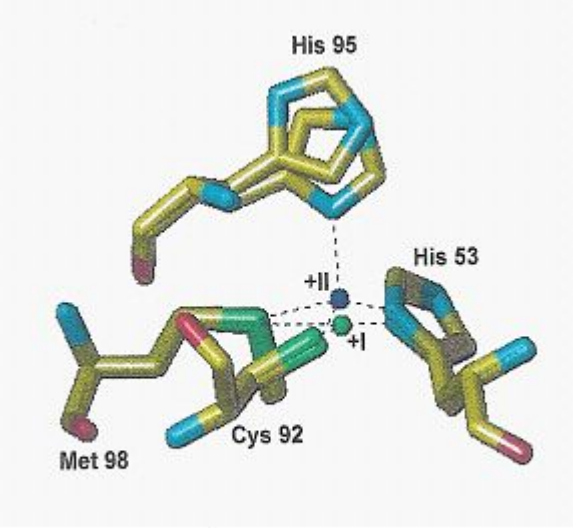

Figure 2.6-1. His^{95} in reduced amicyanin at pH 4.4 reveals that it has rotated 180° about the C_β-C_γ bond relative to its position in oxidized amicyanin and is no longer in the copper coordination sphere

plastocyanin. Potentiometric analysis of amicyanin in complex with MADH indicates that its E_m value is independent of pH between pH 6.5 and 8.5 and is similar to that of free amicyanin at high pH. This is so, because the redox-linked pH-dependent rotation of His^{95} in the complex is hindered; otherwise it would cause an overlap with residues of MADH (Zhu *et al.*, 1998). A P94F mutant of amicyanin has been prepared that increases the E_m value of free amicyanin by nearly 200 mV and shifts the pKa value for its pH-dependence (Machczynski *et al.*, 2002; Sun & Davidson, 2003). The crystal structure of the mutant (unpublished) suggests that the increase in E_m value may be explained by the Phe^{94} backbone N atom moving to within 3.4 Å of the S atom of Cys^{92}, which is a ligand for copper. This suggests that H-bond interactions could significantly modulate the redox properties of the copper site. Precise determination of H-bonding interactions in native and P94F amicyanins will allow us to determine their roles in determining the magnitude and pH-dependence of the redox potential and redox-linked conformational changes in this metalloprotein. Similar studies would be applicable to metalloproteins in general.

The role of water in determining reorganization energies for protein ET reactions. Marcus Theory (Marcus & Sutin, 1985) predicts that ET rates will depend upon ΔG^o, the electronic coupling between donor and acceptor (i.e., the donor-acceptor distance and the characteristics of the intervening medium) and the reorganization energy (λ). λ is defined as the energy needed to deform the nuclear configuration from reactant to the product state. How the protein environment surrounding the redox center will influence this parameter is poorly understood. It is known that the reorganization of water molecules can contribute substantially to λ. The ET reaction from TTQ to copper in the MADH-amicyanin complex exhibits a relatively large λ value of 2.3 eV (Brooks & Davidson, 1994). We have recently characterized an αF55A mutant of MADH that exhibits a λ value of 1.8 eV for the same ET reaction (Sun *et al.*, 2002). This is a rare example of significantly altering λ by site-directed mutagenesis, and it is important to understand the molecular basis for this change. Two water molecules are present in the native MADH active site at a distance less than 5 Å from TTQ and shielded from the bulk solvent by αPhe^{55} (blue structure in Fig. 2.6-2). Only one water in close proximity to TTQ is seen in the αF55A MADH active site (red structure for which electron density is shown). Additional waters are present in the αF55A MADH structure in the space created by the removal of the phenyl ring, but these reside further from TTQ and do not appear to participate in H-bonding interactions with TTQ or active-site residues. If the reorganization of solvent contributes to the λ for ET from MADH, then the reorganization of the inner waters in close proximity to TTQ would be significant. If TTQ is less solvated in αF55A MADH (Figure 2.6-2), then this would be expected to

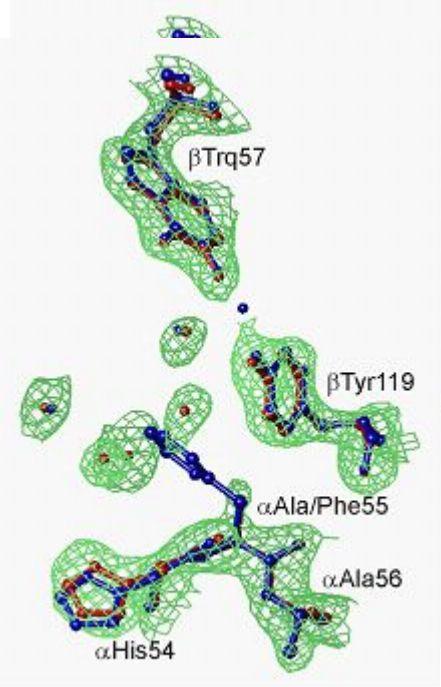

Figure 2.6-2. The native MADH active site.

decrease λ. More specific information about the orientations of these waters and their H-bonding interactions in the oxidized and reduced states of MADH, and other redox proteins, will allow us to more precisely determine the contributions of solvent reorganization to λ and consequently the rates of biological ET reactions.

2.7 Impact of Neutron Diffraction on Structure-Guided and Computer Drug Design

The application of molecular mechanics calculations based on force-field potentials has become an important tool in describing a wide range of biophysical and biochemical properties of proteins and in particular to the application of rational drug design. A primary strength of the approach is that it can provide a window on certain facets of protein structure and activity that are not easily accessible by direct experimentation. However, certain important parameters that define major energetic contributions to the total energy of protein systems are not well determined by direct experimentation, a situation that has made it difficult to judge the accuracy of the computational findings of the dynamics simulations.

The force-field potential functions forming the basis for the calculations are in a continuing state of evolution, being improved when better correlations between theory and experiment are established. At present the components that make up the energy expression used in the calculations vary in their quantitative reliability. For instance, energies describing covalent interactions (stretching, bending, and torsional forces) are well known from spectroscopic and small molecule crystal data. The terms that are least well quantified involve non-bonded interactions (van der Waals, electrostatic, and hydrogen-bonding forces) and the interplay of solvent in the whole picture. Accurate description of the magnitude of these terms is also complicated by the fact that they are modulated by dielectric effects, which are themselves poorly understood as they apply to protein systems. There is disagreement in the literature about how to deal with these effects (Guenot & Kollman, 1992; Schreiber & Stenhauser, 1992; Wesson & Eisenberg, 1992; Williams *et al.*, 1992; Daggett & Levitt, 1993; Elofsson & Nilsson, 1993; Kitson *et al.*, 1993). Clearly a balance needs to be struck between the underlying influence that the electrostatic terms have on the total energy function and how accurately these forces can be approximated. Thus, it is crucial to develop some experimental touchstone to evaluate the accuracy of the individual energy parameters.

Although X-ray protein structures provide a wealth of information about stereochemical details of the time-averaged structure, it is difficult to sort out the relative importance of steric and electrostatic effects in defining certain conformations. Although very few conformations within a polypeptide chain are isolated from some long-range factors, certain categories of interactions exist that can be separated and analyzed for direct short-range effects. Particularly informative groups in this type of assessment are hydroxyl hydrogen atoms (–O–H) and water molecules (H–O–H) (Figure 2.7-1). In a sense, they act as electrostatic probes having degrees of freedom that allow them to orient themselves optimally within the local electrostatic environment. The interior of a protein

represents a well-defined environment in which short-range effects are expected to primarily determine the positions of such hydrogen atoms. Unfortunately, in even ultra-high resolution in X-ray structures hydroxyl and water hydrogen positions are not observable, and therefore assigning an orientation to these groups is not possible. In neutron diffraction, however, the scattering properties of hydrogen and deuterium are sufficient to allow them to be located in density maps, facilitating the determination of the orientation of hydroxyl groups and water molecules when they are well ordered and the analysis is done at high resolution.

A detailed analysis comparing observed hydroxyl and water orientations based on the high resolution neutron structure of the enzyme, trypsin, and those predicted based on an extensive molecular dynamics simulation of the molecule was reported by McDowell and Kossiakoff (McDowell & Kossiakoff, 1995). The hydroxyl orientations determined by sampling the neutron density maps are graphically compared to the results of the dynamics simulation using a polar scatter plot (Fig. 2.7-2). The variations in the dihedral angles over the trajectory of the simulation are generally the result of several possible hydrogen bonding solutions. Overall, the results from the simulation and the neutron density maps are in agreement within experimental error. (An extensive and detailed analysis can be obtained in other papers by these authors (Kossiakoff *et al.*, 1990; Kossiakoff *et al.*, 1991; McDowell & Kossiakoff, 1995). Note however, for example, that the observed and predicted orientation of Tyr234 hydroxyl hydrogen differs by about 30°. On further examination it was determined that this discrepancy was due to an error in a force-field parameter, which has been subsequently corrected. This is an example of the type of input that neutron diffraction structures can contribute to the field of computational chemistry. However, this force field/ structure database is based on a single structure and by its nature is highly incomplete. What is ultimately needed to fill it out is a series of additional comparisons of molecular dynamics hydroxyl and water orientation predictions with their complementary high resolution neutron structures.

The binding modes of inhibitors at protein binding sites can be very sensitive to the protonation states of the residues and functional groups involved in the interactions. The impact of neutron diffraction on drug discovery can accordingly be very significant, due to its ability to provide the correct proton locations. Moreover, as noted above, the availability of neutron structures with correct hydrogen and proton positions will provide an important testing ground for theoretical predictions and will help computational chemists to identify the deficiencies in the current theoretical approaches (*e.g.*, force fields and scoring functions) and to make better predictions in the future.

As an illustration of the importance of correct proton locations and protonation states, the interaction of a transition state analog (zebularine 3,4-hydrate or ZEB-H_2O) with the active site residues of cytidine deaminase (CDA) has been examined using quantum mechanical/molecular mechanical (QM/MM) molecular dynamics (MD) simulations. The QM/MM treatment of the enzyme-TSA complex allows the QM part to undergo chemical transformations (including proton transfers) in the search for stable chemical structure(s) under a given environment. CDA catalyzes the hydrolytic deamination of cytidine to uridine (see Scheme 1A) and accelerates the rate of the

reaction by 10^{11}-fold (Frick *et al.*, 1987). Zebularine (ZEB) binds CDA in a hydrated form (ZEB-H_2O) (Xiang *et al.*, 1995). The hydration process seems to be catalyzed by CDA via a mechanism that is similar to the formation of the tetrahedral intermediate during the CDA-catalyzed reaction (see Scheme 1B). CDA is strongly inhibited by ZEB-H_2O (3 or 4 in Scheme 1B), and the enzyme's affinity (K_i = 1.2 x 10^{-12}M) for ZEB-H_2O exceeds the affinity for the product uridine by a factor of approximately 10^8 (Betts *et al.*, 1994).

Scheme 1

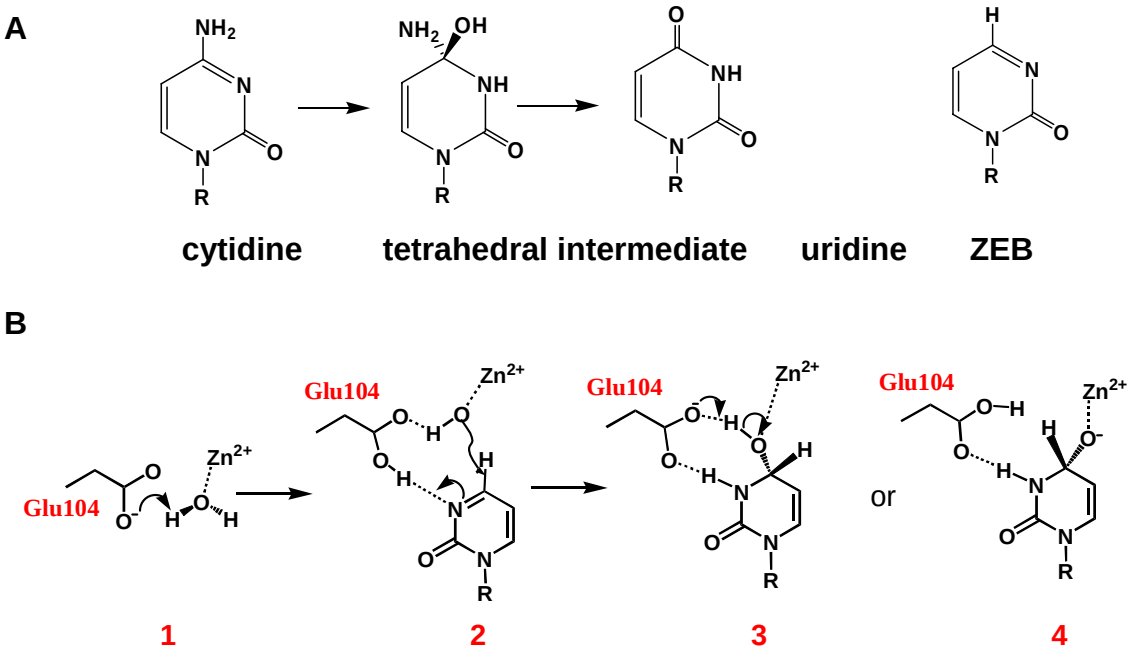

The interaction of ZEB-H_2O with the active site residues obtained from the X-ray structure of the CDA complex (2) is shown in Figure 2.7-3A. One interesting observation is that the covalent bond between C_4 and O_4 (1.6 Å shown in red in Fig. 2.7-3A) is longer than a normal C-O bond (~1.45 Å). In fact, Xiang *et al*. (Xiang *et al.*, 1995) used a restraint of 1.43 Å during the refinement, but the distance changed to 1.6 Å in the final structure. Figure 2.7-3B shows the average structure obtained from molecular dynamics (MD) simulations (Xu & Guo, 2004) based on the assumptions that there exists a zinc-hydroxide in the CDA-ZEB-H2O complex and that Glu104 is deprotonated (as generally accepted and used in the X-ray structure refinement). As can be seen from Figure 2.7-3B, the average structure is rather similar to the one determined experimentally (*e.g.*, the C_4-O_4 distance is 1.57 Å). However, the structure is unstable, and the C_4-O_4 bond undergoes transient bond-breaking and making during the MD simulations; the bond distance approaches or exceeds 2.0 Å about 2-3% of the times (see Figure 2.7-4, the blue line). Figure 2.7-3C shows the average structure from the

simulations when the above assumptions concerning the protonation states are not used. Glu104 is now treated quantum mechanically along with ZEB-H_2O, Zn and the hydroxide. As a result, the proton can move freely between O_4 and Glu104 during the simulations. As is evident from Figure 2.7-3C, the protonation states for Glu104 and Zn-hydroxide as well as the mode of the inhibitor binding have been changed from the earlier simulations. The proton is now located on Glu104 rather than O_4. Figure 2.7-4 shows that the active site structure is now stable without the transient bond-breaking and making (red line). Free energy simulations have also been performed, and it was shown that there may be an extra stabilization of as much as 12 kcal/mol due to the relocation of the proton to Glu104. The prediction for the existence of the different binding mode for ZEB-H_2O in the CDA active site still needs to be confirmed experimentally.

The results of the QM/MM MD simulations suggest that the location of protons as well as the protonation states of active site residues may have a significant effect on protein-inhibitor interactions. The availability of neutron structures with correct hydrogen and proton positions will not only provide a better understanding of protein-inhibitor interactions during the process of drug discovery, but also help to develop effective computational tools for drug discovery.

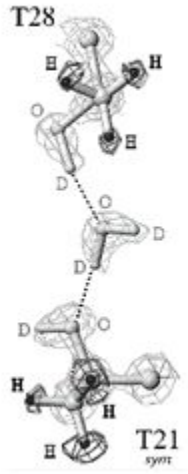

Figure 2.7-1. Orientation of a pair of hydroxyl groups coordinating an intervening water molecule. The hydroxyl group of T28 acts as a H-bonding donor while the hydroxyl of T21 is a H-bonding acceptor.

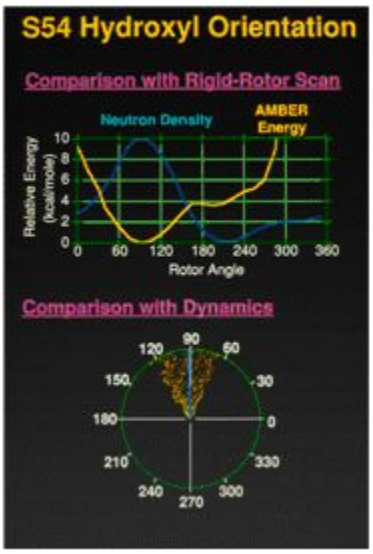

Figure 2.7-2. Comparison of the positioning of a hydroxyl rotor (Ser54), as determined experimentally from the neutron density map, with that predicted from a molecular dynamics simulation. The simulation was interrogated at intervals of 1 psec over the full simulation time of 120 psec. The experimental position matches very well the low-energy position predicted theoretically based on the Amber force-field (upper panel). The lower panel shows a scatter plot of points taken from the MD simulations, the average of which coincide with the experimentally determined torsion angle of 90º.

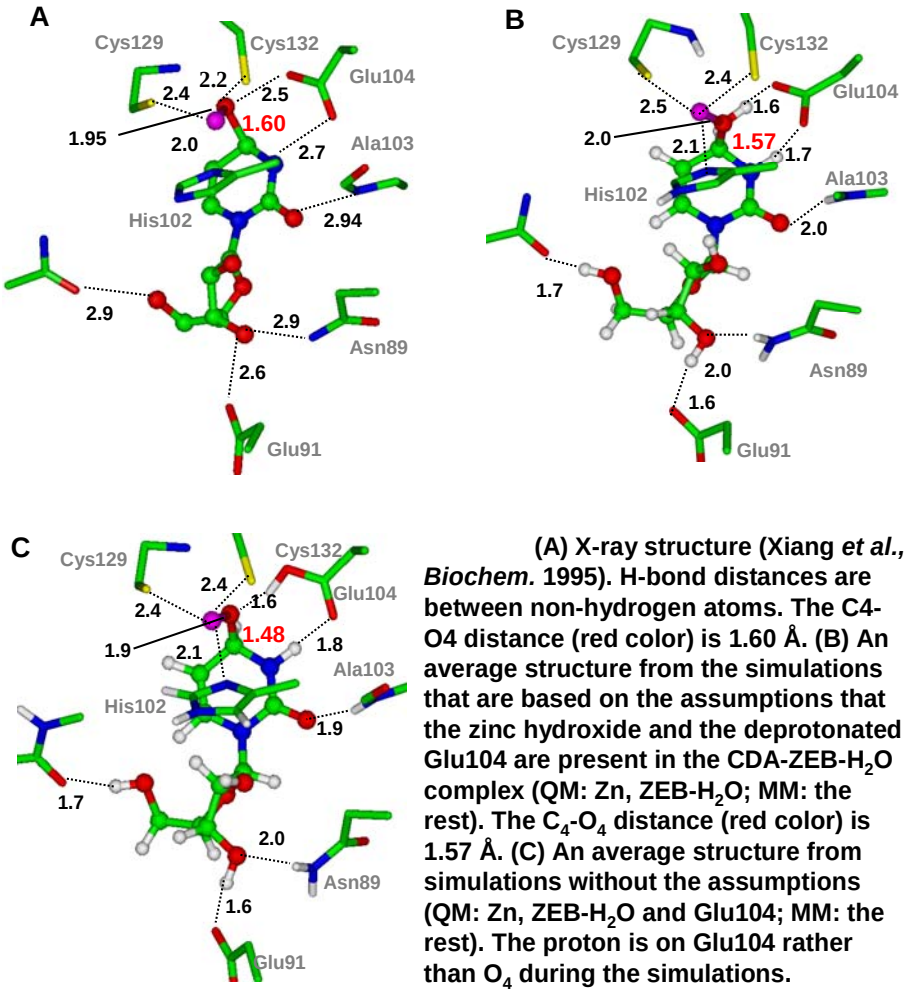

(A) X-ray structure (Xiang *et al., Biochem.* 1995). H-bond distances are between non-hydrogen atoms. The C4-O4 distance (red color) is 1.60 Å. (B) An average structure from the simulations that are based on the assumptions that the zinc hydroxide and the deprotonated Glu104 are present in the CDA-ZEB-H_2O complex (QM: Zn, ZEB-H_2O; MM: the rest). The C_4-O_4 distance (red color) is 1.57 Å. (C) An average structure from simulations without the assumptions (QM: Zn, ZEB-H_2O and Glu104; MM: the rest). The proton is on Glu104 rather than O_4 during the simulations.

Figure 2.7-3. Structural details in CDA.

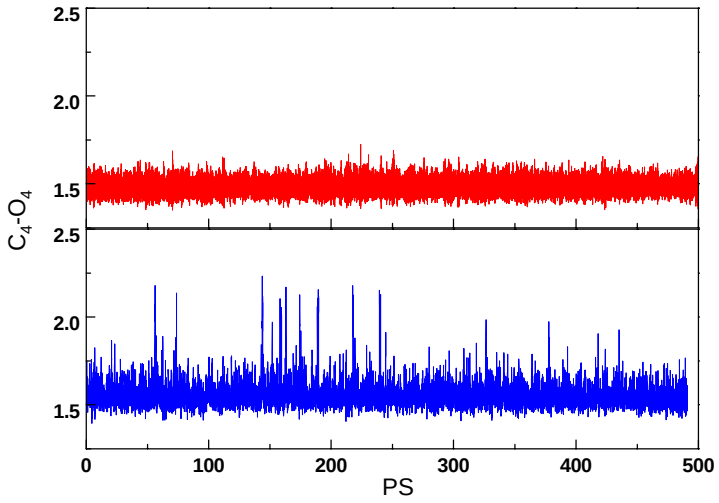

The motion of ZEB-H2O in the active site of CDA as a function of time monitored by the C_4-O_4 distance. Blue: based on the assumptions that there exists a zinc-hydroxide in the CDA-ZEB-H2O complex and that Glu104 is deprotonated; Red: without such assumptions.

Figure 2.7-4. The motion of ZEB-H_2O in the active site of CDA.

2.8 New Opportunities for Neutron Fiber Diffraction

Fiber diffraction (X-ray and neutron) is principally used as a method for determining the structure of filamentous systems at a molecular level. Fiber studies have always formed a lower resolution subset of diffraction studies, providing key information about orientation and positioning of subunits within the fiber, perhaps most famously in Rosalind Franklin's diffraction image of DNA that was essential for deducing the structure. Fiber studies often serve as a bridge between the materials and biological sciences by facilitating the design of synthetic mimics of biological products and improving the biocompatibility of synthetic materials used in biological and medical applications.

As with other X-ray techniques, fiber diffraction can elucidate the position of subunits, but the role of solvent, especially in the condensation of the fiber, is much more difficult to assess. However, in fibers the large neutron scattering power of D and the ability to replace H by D, or H_2O by D_2O, mean that there are important advantages in using neutrons rather than X-rays in order to study hydrogen bonding and hydration and the central roles they play in controlling biologically important structures.

Neutron fiber diffraction studies have provided important information on the location of water molecules or of hydrogen atoms in biological polymers such as DNA and hyaluronic acid (water is a key determinant of structure in these systems), cellulose (hydrogen bonding plays a vital role in determining its unique physical properties), and filamentous viruses. These studies have been reviewed recently as being of "special

interest" and "outstanding interest" (Niimura, 1999b; Stubbs, 1999). The expected gains in data collection efficiency on *MaNDi* at the SNS will open up exciting new opportunities for neutron fiber diffraction.

One new opportunity will be the use of specifically deuterated components in polynucleotide fibers. In addition to replacing labile H on water molecules by D, there is the possibility of replacing covalently bound H by D on specific scattering groups or ligands. Labeling or "highlighting" structural groups in this way can provide unique information on individual chains in triplexes, base sequence dependent conformational variations, and drug binding. Specific deuteration has up until now been prohibitively expensive, but it will become practicable with the smaller sample sizes anticipated at SNS.

Smaller samples also mean new opportunities for studying systems that are currently studied with X-rays but which can only be practically extracted and prepared in small quantities (including bacterial capsid polysaccharides, amyloid fibrils, certain silks, cytoskeletal components, and filamentous viruses). For filamentous systems that can be prepared as large samples, the projected gains in data collection efficiency open up the exciting opportunity of following rearrangements in hydration and hydrogen bonding during structural transitions in fibers.

2.9 Impact of Low-Resolution Neutron Diffraction Studies in the Biological Sciences

Low-resolution crystallography using neutron diffraction and contrast variation is a unique method for determining molecular arrangements in large multi-component macromolecular complexes. This technique has been especially valuable for studies of crystals of membrane proteins. In such crystals, various types of detergents are essential components, but X-ray diffraction provides little information on detergent locations, due to disorder. Using contrast variation, all disordered components, including disordered parts of the protein, can be located with only low-resolution data.

A dedicated instrument for low-resolution NMC, DB21, has operated at the ILL since 1985. This instrument uses a wavelength of 7.5 Å, and it can measure on systems with unit cell repeats up to 300 Å while still requiring crystals of only 0.1mm^3 in volume. DB21 currently is the only instrument anywhere for such studies, although some earlier studies were made using small-angle neutron scattering instruments. *It is therefore critical that MaNDi be designed to operate in low-resolution mode using long-wavelength neutrons, vide infra*. To date, low-resolution NMC has been used in studies including the following: a) membrane protein/detergent complexes (Zulauf *et al.*, 1986; Roth *et al.*, 1989; Roth *et al.*, 1991; Pebay-Peyroula *et al.*, 1995; Penel *et al.*, 1998; Snijder *et al.*, 2002; Prince *et al.*, 2003), b) protein/nucleic acid complexes such as viruses (Timmins *et al.*, 1994) and nucleosomes (Finch *et al.*, 1980; Bentley *et al.*, 1981; Bentley *et al.*, 1984), c) heterooligomeric proteins using specific deuteration of certain proteins or fragments (Trewhella *et al.*, 1986), and d) macromolecular shape

determination (surface envelopes) for *ab initio* phasing of X-ray diffraction data (Badger, 1996).

The methods of contrast variation, selective deuteration, and neutron diffraction have also been extensively used to locate molecular constituents in partially ordered structures such as membrane stacks (Saibil *et al.*, 1976), two-dimensional membrane crystals (Trewhella *et al.*, 1986), and protein or protein/nucleic acid fibers.

Clearly, a protein crystallography instrument at SNS that has the capability of measuring on materials with unit cell repeats up to 250 or 300 Å would be of great value for the analysis of macromolecular complexes. Technical requirements for these large unit cells are largely compensated by the need for only low-resolution data, *e.g.*, 10 to 15 Å. An essential requirement for low-resolution, contrast variation studies is that the instrument be capable of measuring all the low-Q data. Appropriate combination of collimation and wavelength range would make such studies an option on the *MaNDi* instrument that would normally be used for smaller protein structures at higher resolution.

DESIGN OF *MaNDi*

3.1 Introduction

MaNDi will be designed to be the best-in-class diffractometer for fast and efficient measurements of a full hemisphere of Bragg data with a resolution of 1.5 Å on macromolecular crystals with lattice constants in the range of 150 Å ($\Delta d/d$ = 1%). With larger crystals, it will be able to obtain useful data in the resolution range of 2.0-2.5 Å for unit cell repeats of up to 300 Å. Based on both analytical and Monte Carlo simulations the design will ensure that, for a given resolution, *MaNDi* will achieve the highest throughput, minimal peak overlap, and high signal-to-noise ratio. A three-dimensional computer model of *MaNDi* is shown in Figure 3.1-1.

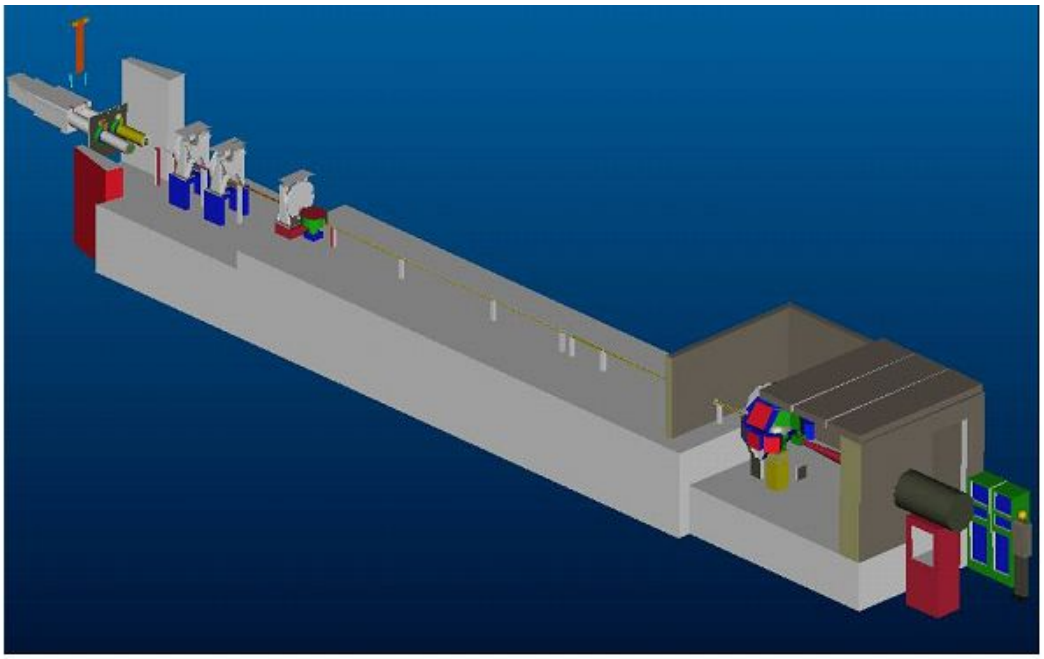

Figure 3.1-1. Three-dimensional model of MaNDi.

The performance of *MaNDi* at both the coupled and decoupled liquid hydrogen and water moderators at the SNS has been investigated by employing well established analytical procedures and Monte Carlo simulations as described in Sections **3.3** and **3.4**. Water moderators have lower flux than cryogenic liquid hydrogen moderators in the useful wavelength region for neutron macromolecular crystallography. A coupled hydrogen moderator can provide higher neutron flux in the wavelength region 1.5 – 5.0 Å, but the longer pulse widths significantly compromise the resolution for larger unit cell systems. Our calculations show that the high resolution applications in structural biology requires a moderator that provides high neutron flux in the wavelength region 1.5 to 5 Å and narrow pulse widths such as the decoupled liquid hydrogen moderator at SNS. Furthermore, the improved signal-to-noise of the decoupled moderator leads to shorter experimental beam times than with the coupled moderator for medium to large unit cells with lattice constants of ~100 Å or greater (see Sections 3.3 and 3.4).

Based on these evaluations, *MaNDi* has been designed for a decoupled hydrogen moderator with a 24.5 m flight path allowing a wavelength bandwidth of about 2.7 Å (without any frame overlap) for the source frequency of 60 Hz at SNS. It will employ a set of three choppers located at 7.2 m, 8.2 m, and 10.4 m downstream from the moderator, respectively, for the selection of wavelength bandwidth. State-of-the-art high index neutron supermirror guides will be used for the efficient beam transport leading to a flux gain at the sample position in the range of 2-10 when compared to that with no guide. A curved guide in the middle section will reduce the overall instrument background and will eliminate any potential radiation damage by γ rays and high energy neutrons from the target to the crystals of biological samples. The combination of a wide wavelength bandwidth, sharp pulse width at each wavelength and large solid angle detector coverage will provide unprecedented high through-put and resolution for *MaNDi* in comparison to the current facilities for NMC. Indeed *MaNDi* for the first time will push the envelope in NMC on two fronts: smaller crystals (<1 mm^3 normal and ~ 0.1 mm^3 perdeuterated proteins) and large unit cell edges (> 100 Å), both of which are beyond the limits of the current limited facilities.

3.2 Conceptual Design

The main features of the conceptual design include:

- **Moderator choice**
  It has been suggested that a coupled moderator should be used for NMC applications since NMC is a highly flux limited technique. However, our calculations (described below) show that the decoupled cold hydrogen moderator has superior pulse resolution *and* signal-to-noise.

- **Neutron guide system**
  As part of a neutron guide system, a curved guide takes the sample out of the moderator's direct line-of-sight and will thus reduce background and eliminate radiation damage to the biological samples by γ rays and high energy neutrons. Together with a subsequently following straight guide, such a guide system will provide an efficient beam transport of cold neutrons as well as the tunability of angular divergence as required at the sample position.

- **Bandwidth choppers**
  Choppers with variable phase settings will be used to provide access to different wavelength bandwidths of neutrons sorted by time-of-flight (TOF).

- **Beam defining optical components**
  The use of a variety of beam defining optical components will give flexibility to match the flux, angular divergence, and consequently instrument resolution to different experimental requirements.

- **Sample stage**
  A kappa goniometer on a positioning table will be used for mounting and orienting the crystals.

- **Detectors**
  An array of state-of-the-art position-sensitive area detectors will be used to cover a wide solid angle around the sample.

3.2.1 Layout of MaNDi

Figure 3.2.1-1 shows the schematic layout of an optimized high throughput and high resolution *MaNDi* instrument determined from analytical calculations and Monte Carlo simulations and Table 3.2.1-1 provides the preliminary instrument parameters. *MaNDi* will be positioned next to the *Single Crystal Diffractometer* (to be built at SNS beam line 12), sharing beam port 11 with the high resolution *Powder Diffractometer (POWGEN3)*.

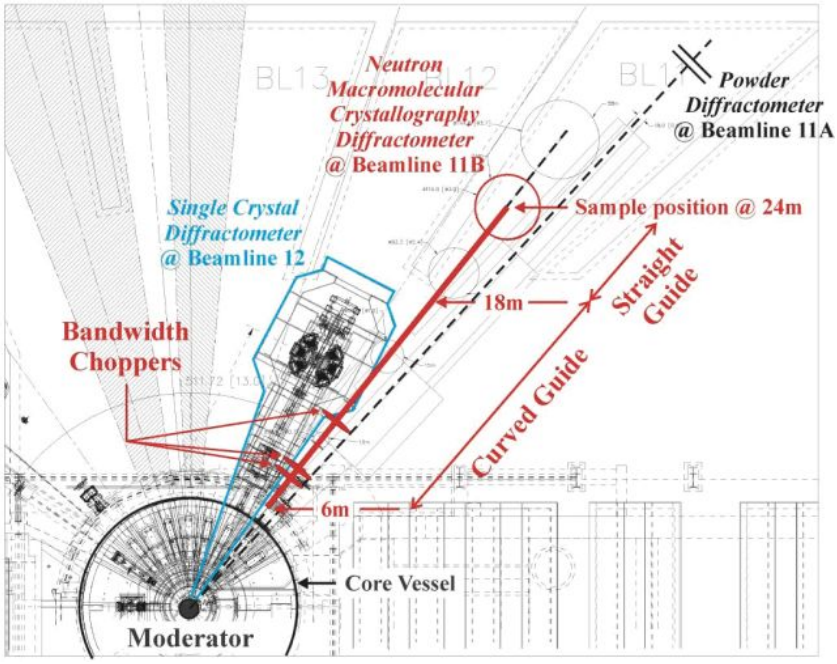

Figure 3.2.1-1. Schematic layout of the *MaNDi* instrument

Table 3.2.1-1. Preliminary instrument parameters of *MaNDi*

Moderator	Moderator type	Top Upstream
	Material	Para-Hydrogen
	Decoupler	Cadmium
	Poison	Gadolinium
	Poison depth	27 mm
	Width	0.10 m
	Height	0.12 m
Curved Guide	Starting point	6 m downstream
	Width	1.5 cm
	Height	1.5 cm
	Length	12 m
	Supermirror coating	m=3
	Total turn angle	0.43°
	Radius of curvature	1599 m
	Line-of-sight lost	≈20 m
Straight Guide	Starting point	18 m downstream
	Width	1.5 cm
	Height	1.5 cm
	Length	Variable: Depends on resolution requirement
	Supermirror coating	m=3
Bandwidth Choppers	Positions	7.2 m, 8.2 m, 10.4 m
Moderator-to-sample distance		24 m
Wavelength range	2.0 Å ≤ λ ≤ 4.69 Å	$\Delta\lambda$ = 2.69 Å
Wavelength resolution		≈ 0.15%
Sample-to-detector distance		0.5 m
Detectors	Array of 2-D PSDs	1 mm resolution scintillation detectors

3.2.2 Neutron Guide System

To efficiently transport cold neutrons from the moderator to the sample position, *MaNDi* will use high index curved and straight guides because of their following advantages:

- Neutron guides offer significant gain in flux when compared to natural collimation viewing the whole moderator.
- Curved guides in the middle section of the beam line make it possible to gently steer the neutron beam such that the sample is completely out of line-of-sight of the source.

- Small widths of the beam allow for the more efficient operation of bandwidth choppers for wavelength selection.

A curved guide provides two advantages: (1) It has a clear cut-off wavelength, i.e. it prevents leakage of high-energy neutrons through absorbing beam conditioning devices (chopper blades, slits etc.), and (2) It will make the operation of *MaNDi* easier from the safety point of view because it will allow only cold neutrons in the beam at the sample position.

3.2.3 Guide Layout

Monte Carlo (MC) simulations using the IDEAS package (Lee & Wang, 2002) were used to optimize the length, location, curvature, and type of supermirror coating of the neutron guide system, and the distance from the guide exit to the sample. *MaNDi*'s guide system starts at a distance of 6 m from the moderator, and consists of a 12 m long curved guide followed by a straight guide (Fig. 3.2.3-1) whose length can be selected based on the resolution requirement. The sample position is at 24 m and the distance between sample and detector will be 0.5 m or less. The sample-to-detector distance will be defined at a later stage giving due consideration to the spatial resolution of the detector, cost, ΔQ resolution, etc.

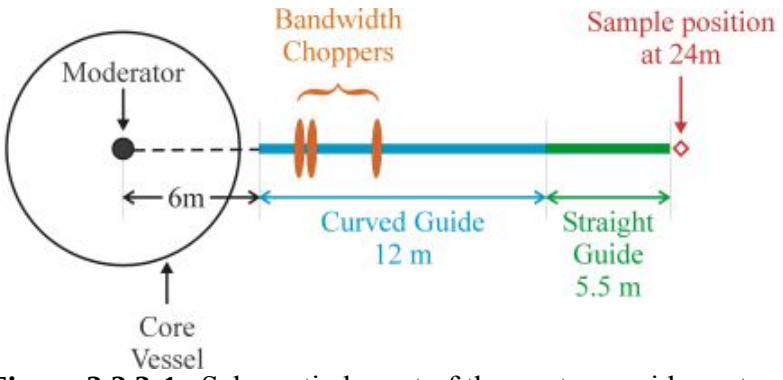

Figure 3.2.3-1. Schematic layout of the neutron guide system.

Figure 3.2.3-2 shows the ratio of the intensity values at sample position with and without guides as a function of wavelength. It follows that substantial gain in flux (up to a factor of 12) can be achieved by using a guide system (supermirror coating $m = 3$) when compared to the natural collimation. The gain in intensity is related to the increase in the angular divergence of the beam as shown in Figure 3.2.3-3 (e.g. for neutrons with $\lambda = 2$ Å the FWHM beam divergence is $\approx 0.4°$). However, the incident neutron beam divergence can be adjusted to match the resolution requirements of a given experiment by using interchangeable sections of guide and/or a variety of collimators before the sample position.

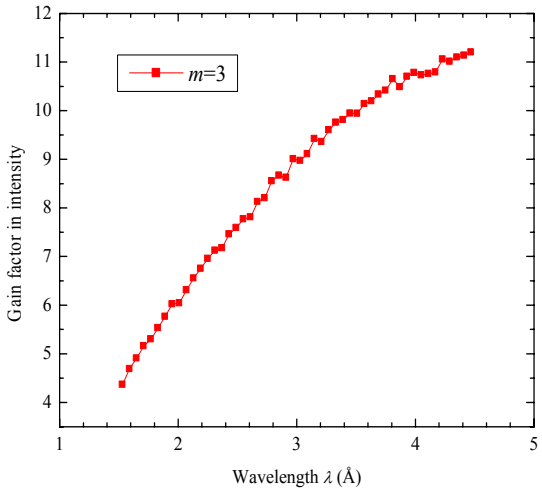

Figure 3.2.3-2. Gain vs. wavelength for the neutron guide system.

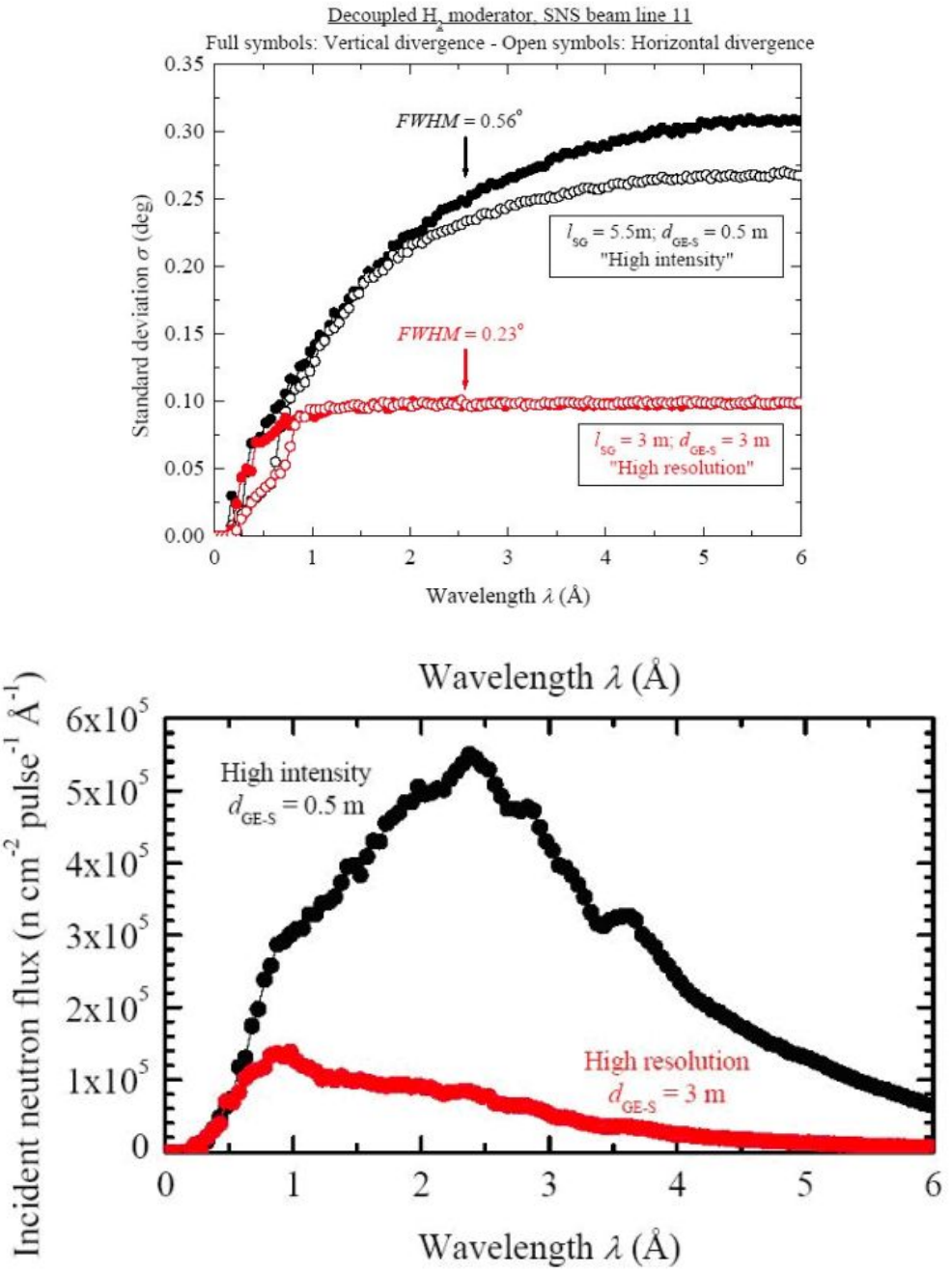

Figure 3.2.3-3. Upper panel: beam divergence at the crystal position for a guide ending 0.5 m upstream from the sample position (black) and for a guide ending 3 m upstream (red). Lower panel: incident fluxes for the two guide ending positions.

3.2.4 The Sample Position

The moderator-to-detector length of 24.5 m of the instrument has been chosen to utilize a large wavelength band of neutrons ($\Delta\lambda$ = 2.69 Å) that can be sorted by time-of-flight with a reasonable time resolution.

Figure 3.2.4-1 shows a MC simulation of neutron flux at *MaNDi*'s sample position (24 m downstream from the moderator, sampling area 1 cm × 1 cm). The black curve represents intensity calculated without a guide system. Data shown in red represent intensities of wavelengths 0.1 Å ≤ λ ≤ 5 Å (open symbols) and intensities of the useful wavelength range $\Delta\lambda$ (closed symbols), respectively. The integrated intensity in consideration of the useful wavelength bandwidth amounts to 6.8×10^7 n cm^{-2} s^{-1} (high intensity guide setting).

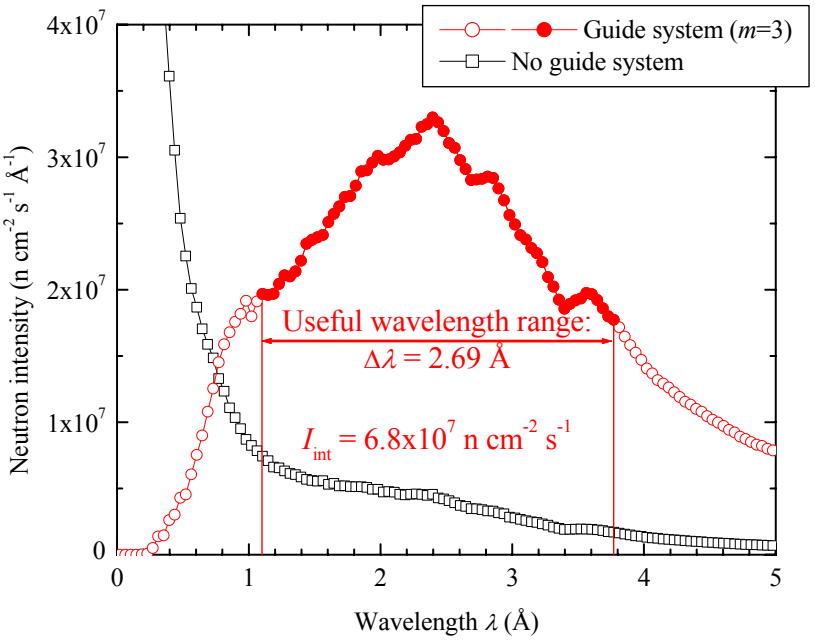

Fig. 3.2.4-1. Calculated neutron flux at sample position for high intensity guide setting.

3.2.5 Beam Defining Optics

The beam divergence can be readily tuned by addition/removal of 0.5 m long guide sections between the guide exit and the sample. In addition, beam defining optics such as Soller collimators, polycapillary focusing optics (Gibson *et al.*, 2002; Mildner *et al.*, 2002), tapered guides and pinhole collimators, will be designed for insertion between the guide exit and the sample to further optimize the beam divergence to experimental requirements.

3.2.6 Detectors

An array of state-of-the-art high efficiency position sensitive area detectors with a spatial resolution of ~1 mm will be used to cover a wide solid angle around the sample. Recently developed scintillation detectors for time-of-flight single crystal neutron

diffractometer SCD at IPNS can potentially be used on *MaNDi*. New detector technology being developed at IPNS will enable the use of tiled area detectors with minimal gaps.

3.3 Moderator Choice – Analytical Calculations

The two conflicting parameters, intrinsic flux limitation and the high resolution requirement for structural biology, pose a challenge in the selection of the best moderator for NMC applications at SNS. In the following we carefully analyze the performances of both a coupled hydrogen, a decoupled hydrogen and two decoupled water moderators for protein diffraction applications at the high-power target station (HPTS) at SNS, giving due consideration to:

- Resolution
- Emission times
- Effective FWHM of the pulses
- Counting statistics

Since high resolution structural biology requires high flux of cold neutrons, a coupled hydrogen moderator has been proposed by many for NMC applications. However, when high resolution data for crystals with unit cell size greater than 100 Å are required our calculations show that it is important to consider both the flux and the resolution (pulse lengths of the emission time) of the moderator. The increased flux from the coupled moderator (8 times that of the decoupled moderator at $\lambda > 2.5$ Å) comes at the cost of a pulse width that is about 8 times larger than that of the decoupled moderator. Monte Carlo simulations show that if *MaNDi* views a coupled hydrogen moderator the long tails in the emission times (pulse width) will be detrimental to both its resolution and the counting statistics (signal-to-noise).

Table 3.3-1 provides a list of the moderators and beamlines which have been simulated and for which "metrics" and "source" files are available on the SNS web site (Iverson, 2002). These files contain the flux and pulse shape data that are used in the calculations and simulations described in this proposal. The decoupled hydrogen moderator refers to beamline 11 and the coupled hydrogen refers to beamline 5. We also performed Monte Carlo simulations for the water moderators on beamline 8 (high resolution water) and beamline 17 (high intensity water). The list of comparable beamlines, which are currently assigned to no instrument, are also listed in Table 3.3-1.

Table 3.3-1. Simulated and available beamlines at the SNS High Power Target Station

Moderator	Material	Decoupler	Poison	Poison Depth	Beamline Simulated	Beamline Available
Top Upstream	para-hydrogen	cadmium	gadolinium	27 mm	11	11B
Top Downstream	para-hydrogen	none	none	n/a	5	14A
Bottom Upstream	water	cadmium	gadolinium	15 mm	8	8 or 9
Bottom Upstream	water	cadmium	gadolinium	25 mm	17	16

*The choice of the moderator was evaluated by two independent approaches. The first approach described in this section (***3.3***) is based primarily on well-established*

analytical expressions, which are used to calculate resolution, flux and count rates. In section **3.4***, all moderator options were simulated by Monte Carlo techniques and the results were evaluated by deriving a Figure-of-Merit for each possible instrument configuration. Based on both approaches, it has been found that the decoupled hydrogen moderator is superior to other moderators for MaNDi.*

3.3.1 Effective Flux of the Decoupled Hydrogen Moderator

In order to make decisions on the optimal wavelength range for the diffraction experiments an effective flux is calculated by weighting the flux from the moderator for the reflectivity of neutrons.

The integrated intensities I_{hkl} are related to structure factor amplitudes $|F_{hkl}|$ based on the Laue formula:

$$I_{hkl} = \phi(\lambda)\frac{V_s}{V_c}\frac{\left|F_{hkl}\right|^2}{V_c}\frac{\lambda^4}{2\sin^2\theta} \tag{1}$$

where $\phi(\lambda)$ is the incident neutron intensity per unit wavelength range at wavelength λ ($n \cdot cm^{-2} \cdot sec^{-1} \cdot Å^{-1}$), V_s is the sample volume, V_c is the crystal unit cell volume, F_{hkl} is the structure factor, and 2θ is the Bragg angle. Terms for the detector efficiency, sample absorption and extinction have not been included.

Equation (1) can be rewritten as

$$I_{hkl} = \phi(\lambda)\frac{V_s}{V_c^2}\left|F_{hkl}\right|^2 \lambda^2 d_{hkl}^2 \tag{2}$$

This leads to an effective flux (Jauch, 1997; Wilson *et al.*, 2001) of

$$\phi_{eff}(\lambda) = \phi(\lambda)\cdot\lambda^2 \tag{3}$$

In this case, one takes into account that for any *hkl*, the *d*-spacing is constant regardless of the angle. Then, the optimal wavelength for measuring all Bragg peaks is the same, but the optimal angle will be different for each *hkl*.

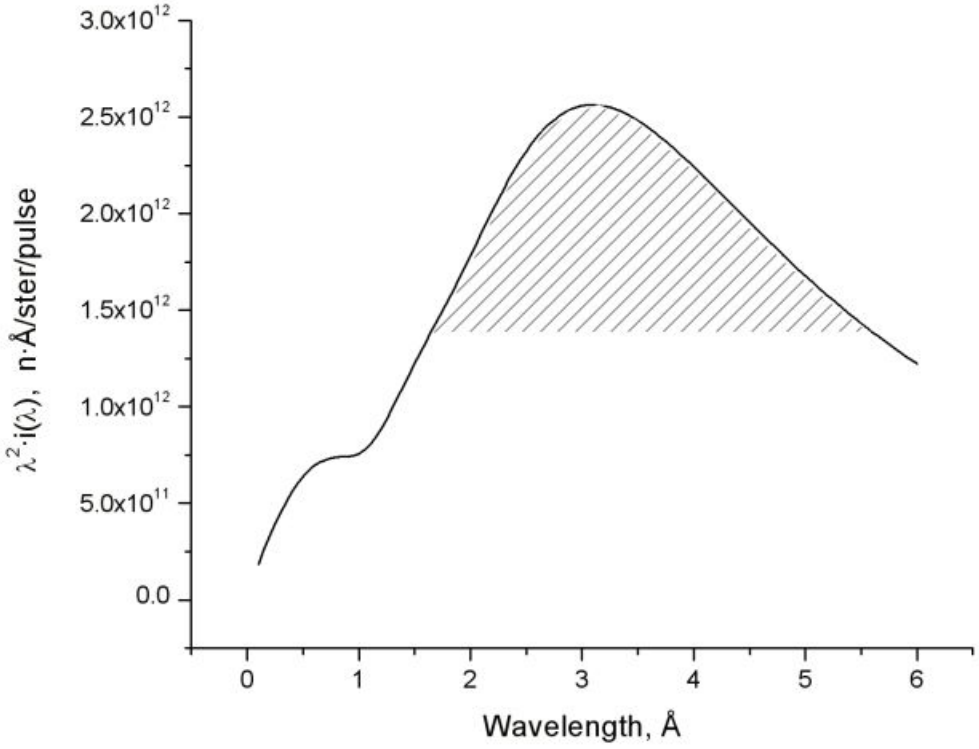

Figure 3.3.1-1. Plot of $\lambda^2 \cdot \phi(\lambda)$ versus wavelength at the moderator surface for the decoupled, poisoned hydrogen moderator.

At the longer wavelengths that we are interested in, the sampling of simulated data points in the moderator data files posted on the SNS web site (Iverson, 2002) becomes sparse and there appears to be quite a bit of random "noise" in the spectra. Therefore, we have used the equations and parameters in Iverson *et al*. (Iverson *et al.*, 2002) to obtain smoothed spectral curves. Multiplying the flux for the decoupled hydrogen moderator by λ^2 at each wavelength gives the curve shown in Figure 3.3.1-1. It is clear from Figure 3.3.1-1 that wavelengths in the range of 1.5 to 5.0 Å provide the highest effective flux.

3.3.2 Gain vs. Wavelength for Coupled Hydrogen Moderator

In Figure 3.3.2-1, the wavelength dependence of the ratios of the total intensity from the coupled and decoupled hydrogen moderators is plotted. This is the gain in total intensity provided by the coupled hydrogen moderator. It is seen that for wavelengths of about 2.5 Å or greater a flux gain of eight can be obtained with the coupled moderator. However, the overall flux gain for the coupled moderator is greatly diminished in the important wavelength range of 1.5 – 2.5 Å.

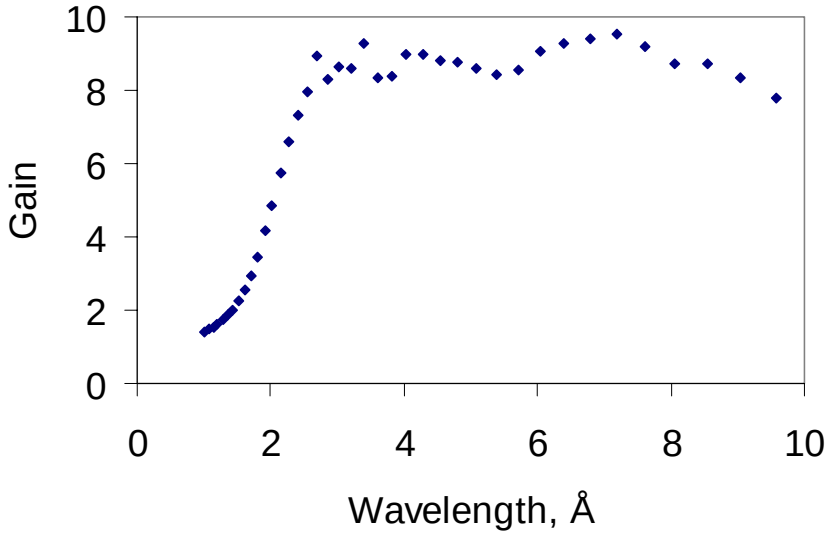

Figure 3.3.2-1. Intensity gain for the coupled hydrogen moderator obtained by calculating the ratio of the total intensities of the pulse at each wavelength of the coupled and decoupled moderators.

3.3.3 Resolution with Different Moderators

For diffraction, the Bragg equation is

$$2d\sin\theta = \lambda \tag{4}$$

In Q space, this becomes

$$Q = \frac{2\pi}{d} = \frac{4\pi\sin\theta}{\lambda} \tag{5}$$

Since

$$\lambda = \frac{h}{m}\frac{t}{L} \tag{6}$$

substituting (6) into (5) gives

$$Q = 4\pi\frac{m}{h}\frac{L}{t}\sin\theta \tag{7}$$

As shown by Crawford (Crawford, 1978), differentiating Equation 7 gives the resolution

$$R = \frac{\Delta Q}{Q} = \left[\left(\frac{\Delta t}{t}\right)^2 + \left(\frac{\Delta L}{L}\right)^2 + \left(\tfrac{1}{2}\Delta 2\theta\cot\theta\right)^2\right]^{1/2} \tag{8}$$

In terms of d-spacings in real space, it can be shown that R also equals $\Delta d/d$ in the following manner, where $d_1 < d_2$:

$$R = \frac{\Delta Q}{Q} = \frac{\left(\frac{1}{d_1} - \frac{1}{d_2}\right)}{\frac{1}{d_1}} = 1 - \frac{d_1}{d_2} = \frac{d_2 - d_1}{d_2} \tag{9}$$

which can be rewritten as

$$R = \frac{\Delta d}{d} \tag{10}$$

Resolution in macromolecular crystallography refers to a minimum *d*-spacing ($d_{\min}$) to which observed data are obtained ($Q_{\max}$), which is then also related to the ability to resolve features in the structure in real space. Let us take the example of a cubic unit cell with unit cell dimensions of $a = b = c$. Then it can be shown that to resolve two Bragg peaks at $d_{\min}$

$$R < \frac{d_{\min}}{a} \tag{11}$$

However, the resolution R as derived from Eq. 8 is based on a Gaussian distribution where the summed terms are standard deviations (σ). For single crystal diffraction, it is not sufficient to resolve peaks, but we need to integrate the peak such that peaks have to be fully separated. Therefore the resolution requirement is

$$R < \frac{d_{\min}}{5a} \tag{12}$$

since from -2.5σ to +2.5σ about the mean contains almost 99% of a Gaussian peak (Jauch, 1986; Jauch, 1993).

One complication is that often the delta terms in (8) are *FWHM* terms and not standard deviations. Since

$$FWHM = 2.354\sigma \tag{12}$$

then 5σ = 2.12 x *FWHM*, such that

$$R_{FWHM} < \frac{d_{\min}}{2.12a} \tag{13}$$

The pulse width time resolution contributes primarily to the resolution parallel to the diffraction vector, whereas the angular resolution primarily contributes to that in the perpendicular direction. From Jauch (Jauch, 1997), the condition

$$\Delta t_{pulse}(FWHM) \le 238.1L\left(\frac{d_{\min}^2}{a}\right)\sin\theta \tag{14}$$

must be met for peaks to be completely separated in the direction of the reciprocal lattice vector at $d_{\min}$ for a crystal with a unit cell axis length of a. In this equation, the units are: t, μs; L, m; $d_{\min}$ and a, Å. For a Gaussian peak, the full width of 5σ is then 2.12 times the $\Delta t_{\text{pulse}}(FWHM)$ obtained from equation (14).

Equation (14) can be derived in the following manner. We begin with the following equations:

$$\frac{\sigma(t)}{T} = \frac{d_{\min}}{5a} \tag{15}$$

$$2d\sin\theta = \lambda \tag{16}$$

$$\lambda = \frac{h}{m}\frac{T}{L} \tag{17}$$

$$T = 2\frac{m}{h}Ld_{\min}\sin\theta \tag{18}$$

Making the appropriate substitutions, we obtain

$$\sigma(t) = \frac{2}{5}\frac{m}{h}L(\frac{d_{\min}^2}{a})\sin\theta \tag{19}$$

Since $FWHM = 2.354\sigma$,

$$\Delta t_{pulse}(FWHM) = \left[2.354(\frac{2}{5})\frac{m}{h}\right]L(\frac{d_{\min}^2}{a})\sin\theta \tag{20}$$

Evaluating the terms in the brackets leads to equation (14).

3.3.4 Effective FWHM of the Pulses

Figure 3.3.4-1 shows the pulse shapes for 2.55 Å neutrons from the coupled and decoupled hydrogen moderators. For the coupled liquid hydrogen moderator, the intensity at the peak region of the pulse is only about 1.5 times greater than that from a decoupled liquid hydrogen moderator. However, the pulse width is over 8 times larger for the coupled moderator. Thus the pulse shapes are not Gaussian so that 2.13*FWHM* does not contain 99% of the peak. The values for the coupled and decoupled hydrogen moderators are compared in Table 3.3.4-1. Since 99% can be considered as too difficult to achieve, we have adopted a goal of 90% of the total intensity, or 10% of the maximum, whichever is longer. It is seen from Table 3.2.6-1 that the eightfold gain in intensity with the coupled moderator results at the expense of nearly ten times larger pulse width for the decoupled moderator. The longer pulse widths at the coupled moderator, in addition to affecting the resolution parallel to the *q*-vector, will increase the background by about 8 times, thus affecting the signal to noise ratio of the diffraction peaks.

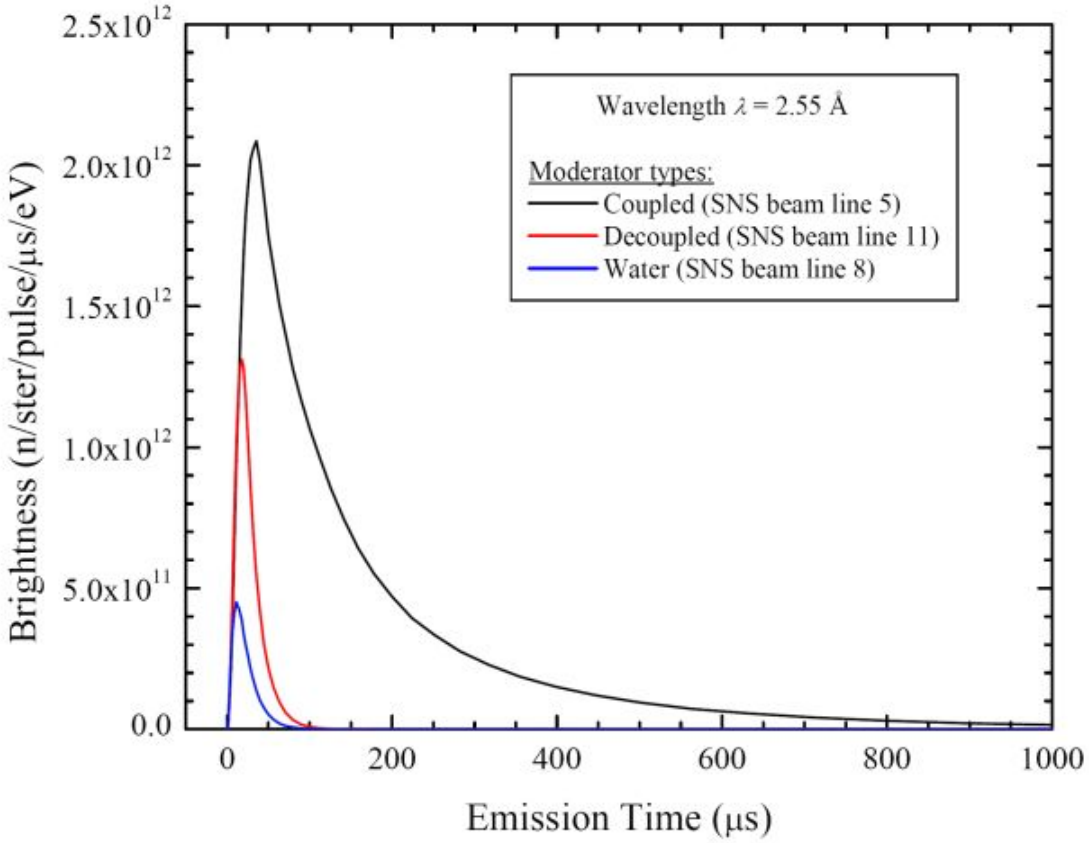

Figure 3.3.4-1. Pulse emission distribution for neutrons with λ = 2.55 Å for the coupled and decoupled liquid hydrogen moderators (and water) at the HPTS at SNS.

Table 3.3.4-1. Comparison of coupled and decoupled H_2 moderators for the pulse corresponding to $\lambda = 2.55$ Å

Parameter	**Coupled H_2**	**Decoupled H_2**	**Ratio**
Total intensity (n/ster/pulse/eV)	3.06×10^{14}	3.84×10^{13}	8.0
FW at 90% of total intensity (μsec)	430	45	9.6
FW at 10% of max (μsec)	335	58	5.8

Table 3.3.4-2 provides the maximum allowable pulse full widths derived from equation (14) for different wavelengths and corresponding Bragg angles to resolve peaks for a cubic system with $a = 150$ Å, $d_{min} = 1.5$ Å, and $L = 24.5$ m. Also shown are the full widths corresponding to 90% of the total intensity, or 10% of the maximum, whichever is longer, for the pulse from each moderator.

Table 3.3.4-2. Calculated maximum allowed pulse full widths (Eq. (14)) and ratios of the pulse full widths and intensities of the coupled and decoupled hydrogen moderators at different wavelengths for a 24.5 m instrument (a = 150 Å, d_{min} = 1.5 Å,).

2θ (deg)	λ (Å)	Equation (14) FW (μsec)	Coupled FW (μsec)	Decoupled FW (μsec)	FW Ratio	Intensity Ratio
30	0.776	49	33	17	1.9	1.1
60	1.500	94	300	27	11.1	2.2
90	2.121	132	400	44	9.1	5.8
120	2.598	162	430	58	7.4	8.0
150	2.898	181	445	66	6.7	8.3

The data in Table 3.3.4-2 leads to the following conclusions:

- *The pulse width of the decoupled moderator is more than adequate at all wavelengths. Perhaps a partially coupled moderator or one with a greater poison depth that can provide higher flux could be useful, but such a moderator is not available at the SNS.*
- *The effective FWHM values for the coupled moderator are higher than the values in Equation (14) and hence a 24.5 m long instrument cannot take advantage of the higher flux with coupled moderator.*

One way to take advantage of the higher flux from the coupled hydrogen moderator for NMC is by increasing the length of the flight path to 75 m (see Equation (14)). Although such a long flight path instrument can be useful for NMC applications, there are several disadvantages.

- Resolution is still borderline as can be seen in Figure 3.3.7.1-3, where we have shown the peak shapes for a top hat function corresponding to a d_{min} = 1.5 Å for a cubic unit cell of 150 Å (*vide infra*). The peaks are well separated for a 24 m long instrument with a decoupled liquid hydrogen moderator, while there is a large peak overlap for a similar length instrument viewing a coupled moderator. Although the peak overlap has improved for a 75 m long instrument, it is still inferior to the decoupled moderator case.
- The usable wavelength bandwidth ($\Delta\lambda$) will be reduced due to frame-overlap condition,

$$\Delta\lambda = 3955/(f \cdot L) \tag{21}$$

  where, L is the instrument flight path length (m) and f is the source frequency (60 at SNS).
- Total guide efficiency for longer wavelengths at 75 m will be about 60% (based on MC simulations) and much less for shorter wavelengths.

- There is a large additional cost associated with the construction of a 75 m long instrument.

3.3.5 Counting Statistics

For protein crystals, the large unit cells lead to weak average peak intensities. In addition, there is a high background due to the incoherent scattering of hydrogen atoms (unless the entire protein is deuterated). For weak peaks with small signal-to-background ratios, the standard deviation of an integrated peak $\sigma(I)$ based on counting statistics is essentially the square root of the background counts B (Wilkinson & Lehmann, 1991; Jauch, 1997; Wilson *et al.*, 2001).

Increasing the integrated flux by a factor of 8 in the case of the coupled moderator will increase the background by a similar factor such that

$$\frac{I_c}{\sigma(I_c)} = \frac{8I_d}{(8B_d)^{1/2}} = 2.8\frac{I_d}{\sigma(I_d)} \tag{22}$$

where I_c is the Bragg peak integrated intensity with the coupled moderator and I_d is the intensity with the decoupled moderator. Thus, there would appear to be a 2.8 times improvement in signal-to-noise ratio. The signal-to-noise gain is true only if the peak widths are the same, so that the number of points (time channels) that are sampled is identical. However, the effective pulse widths for the coupled moderator (see Table 3.3.4-2) is about 8 times larger than that for the decoupled moderator and hence it would require sampling that many more time channels to determine the background properly. In Equation (22), increasing the background counts B by another factor of 8 essentially cancels the effective increase in the signal due to a larger flux with the coupled moderator. However, for cases where $\sigma(I)$ is not dominated by the background, such as crystals with small unit cells, the coupled moderator could offer a modest advantage over the decoupled moderator as discussed in Section 3.4.

Based on the superior pulse resolution of the decoupled moderator and the minimal advantage in overall counting statistics of the coupled moderator, we have concluded that the decoupled hydrogen moderator is the best choice for MaNDi.

3.3.6 Effective Flux Comparison for Water vs. Hydrogen Moderators

A comparison of the room temperature water moderator with the cold hydrogen moderator was also examined. As described above, the plot in Figure 3.2.8-1 was obtained by multiplying the flux $\phi(\lambda)$ in units of n/ster/pulse/Å by the square of the wavelength λ^2 (Å^2) at each wavelength to give an effective flux:

The data shown in Figure 3.3.6-1 are calculated using the equations and parameters in Iversen *et al*. (Iverson *et al.*, 2002) and Equation (2).

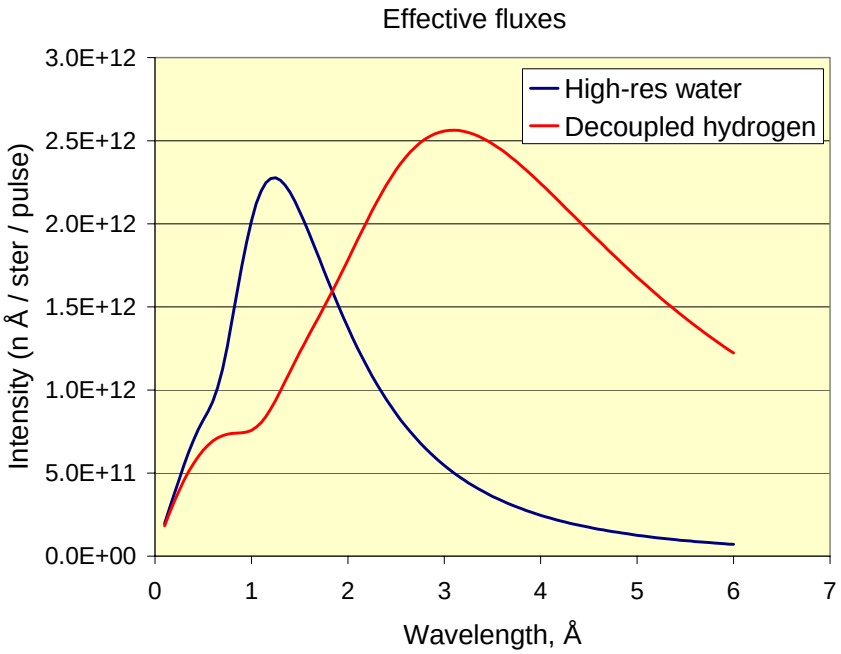

Figure 3.3.6-1. Plots of effective flux at the moderator surface for the high resolution water and the decoupled hydrogen moderators at SNS.

The maxima for the effective flux spectra of water and hydrogen are at wavelengths of 1.25 and 3.10 Å, respectively. For a d-spacing of 2.0 Å, the corresponding 2θ angles are 36° and 102°, respectively, as shown in Table 3.2.8-2. The resolution is evaluated using equation (8).

Table 3.3.6-1. Largest resolvable lattice constants at the peaks in the effective flux for water and hydrogen moderators, all else being equivalent.

	Water	**Hydrogen**
λ at peak in effective flux spectrum, Å	1.25	3.10
2θ, deg.	36	102
Resolution, $\Delta d/d$	0.011	0.0034
d_{min}, Å	2.0	2.0
a, largest resolvable lattice constant at d_{min}, Å	85	275

The values in Table 3.3.6-1 indicate that a cold moderator such as decoupled hydrogen moderator has the advantage of being able to measure data at higher scattering angles where the resolution is much better than at lower scattering angles. The cot(θ) term in equation (8) greatly reduces the resolution and, consequently, the usable detector area for the room temperature water moderator.

3.3.7 Instrument Performance

In this section the expected performance of the *MaNDi* instrument is discussed with respect to

- Resolution
- Data collection times

3.3.7.1 Resolution from Reflectivity Calculations

In order to determine the resolution (and possible overlap) of such peaks, we calculated the reflectivity of a sample (*i.e.*, a mirror), which reflects neutrons in the horizontal plane. The mirror is set up at a nominal angle of 45° relative to the beam and the detector is at 90° horizontally.

Figure 3.3.7.1-1 shows a diagram of the reflectivity input file with three peaks q_{i-1}, q_i, q_{i+1}. These peaks represent three peaks centered at d = 1.5 Å ($q = 2\pi/d$ = 4.19 Å^{-1}) with a unit cell repeat of 150 Å. Then the three peaks correspond to the Bragg index h = 99, 100, and 101. A TOF-instrument with infinite angular and time-of-flight resolution will be able to reproduce this spectrum. If angular and TOF resolution are limited (like in every real experiment), a smearing of the sharp peaks is expected.

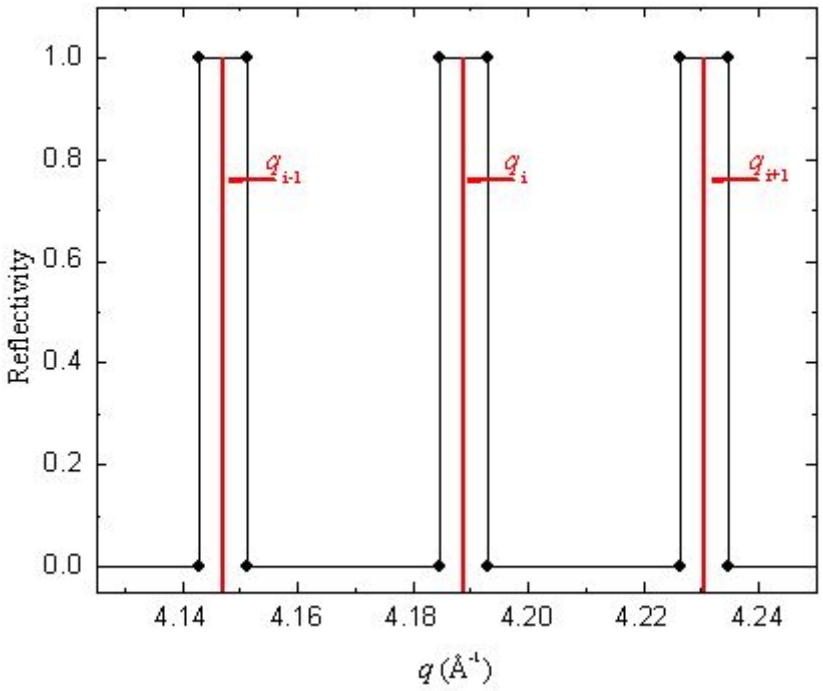

Figure 3.3.7.1-1. Reflectivity input file for IDEAS.

Note that for all calculations,

- *IDEAS* takes the time-dependence of the moderator emission into account.
- *IDEAS* "measures" in time-of-flight mode, i.e. the detector arrival time of neutrons is determined, and data are grouped in small time bins (as it is done at a real instrument). The *q*-values are calculated afterwards. The conversion from time-of-flight to wavelength is not straight forward. The different moderators have a wavelength-dependent emission delay time, which needs to be taken into account.
- The neutron arrival times are measured with a constant time-of-flight resolution of $\Delta t/t$ = 0.035% (i.e. the detector has logarithmic time binning). This provides that all peaks are calculated with approximately the same number of data points.
- The *IDEAS* detector module determines *intensity per TOF bin* per pulse. The data were normalized to obtain the unit: neutrons per second per TOF bin per cm^{-2} of detector area (n cm^{-2} s^{-1} bin^{-1}).
- Sample width is to be understood "transverse relative to neutron beam".
- The "no guide" option means a full view of the moderator (10 cm wide, 12 cm high).
- The "natural" beam divergence calculated at the sample position is determined by viewing the full moderator size, the distance between moderator and sample, and the sample size.
- The "natural" divergence calculated at the detector is determined by the sample size, the distance between sample and detector, and the detector pixel size.

Figure 3.3.7.1-2 shows schematically three different *MaNDi* instrument configurations.

- Blue: A 75.5-m-long instrument at a coupled moderator, $\Delta\lambda$ = 0.87 Å
- Green: A 24.5-m-long instrument at a coupled moderator, $\Delta\lambda$ = 2.69 Å
- Red: A 24.5-m-long instrument at a decoupled moderator, $\Delta\lambda$ = 2.69 Å

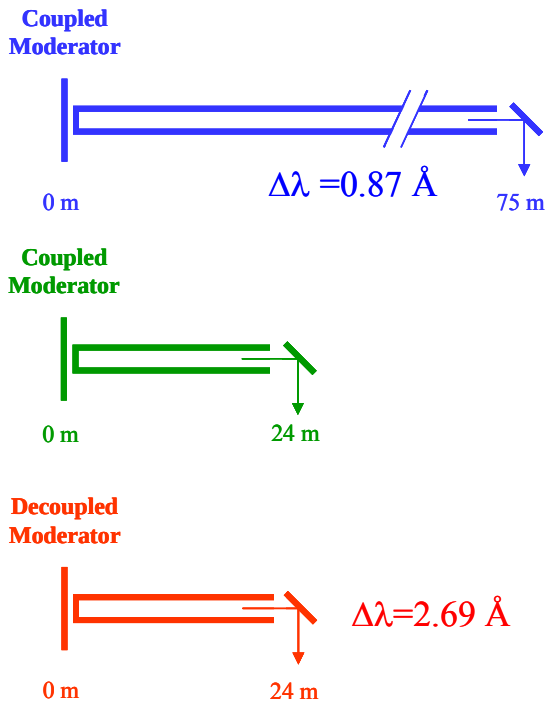

Figure 3.3.7.1-2. Three different *MaNDi* instrument configurations at liquid hydrogen moderators at SNS.

Figure 3.3.7.1-3 shows peak shapes calculated for the three different instrument configurations. It follows from Figure 3.3.7.1-3 that using a decoupled moderator at a 24.5-m-long instrument (red curve) would be the best choice for measuring a set of high-resolution Bragg data. Although a coupled moderator has higher flux, this extra intensity is not useful since it results in an increased background (and therefore making the desired separation of the peaks impossible). Compared to a 24.5-m-long instrument for the coupled moderator, the 75.5-m-long instrument shows a better (but not complete) separation of the peaks. This, however, comes at the expense of reduced bandwidth (factor 3) and at the expense of much higher cost for the instrument (longer neutron guide, much larger shielding volume).

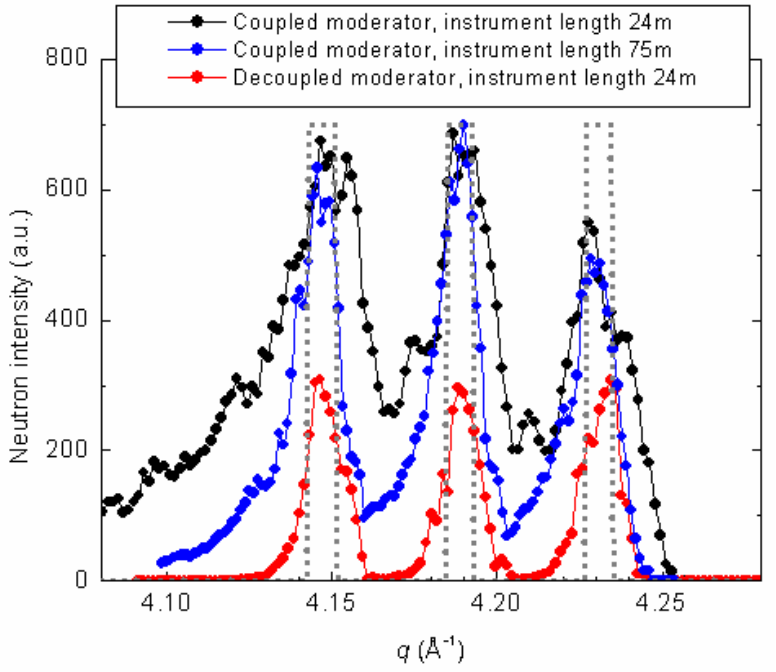

Figure 3.3.7.1-3. Peak shapes for a top hat function corresponding to a d_{min} = 1.5 Å for a cubic unit cell of 150 Å for configurations of MaNDi in Figure 3.3.7.1-2.

The presented data in Figure 3.3.7.1-3 confirm the results from analytical calculations. If *MaNDi* views a coupled moderator, the instrument length would need to be more than 100 m in order to achieve a similar resolution as a 24 m long instrument at a decoupled moderator.

3.3.7.2 Data Collection Times

The performance of *MaNDi* has been calculated based on counting times necessary to obtain a complete data set for protein crystals with different unit cell sizes, by taking into consideration of the data precision, Debye-Waller factor, flux and incoherent background.

We calculated counting times based on an Equation 23 proposed by Jauch (Jauch, 1997):

$$t = \frac{V^2}{5\varepsilon^2\phi(\lambda)\lambda^2 V_s AN\langle b^2\rangle}\frac{N_{inc}}{N}\frac{\sigma_{inc}/4\pi}{\langle b^2\rangle}H_0^2\frac{f(BH_0^2/2)}{\langle T_H\rangle} \qquad (23)$$

The parameters in Equation 23 are defined in Table 3.3.7.2-1

Table 3.3.7.2-1. Parameter definitions for Equation 23.

Parameter	Description
V	unit cell volume
V_s	crystal volume
N	number of atoms in the unit cell
B	isotropic temperature factor
N_{inc}/N	ratio of incoherent (hydrogen) atoms to total atoms
σ_{inc}	incoherent cross section
A	transmission due to sample absorption
ε	precision of the data set ($\varepsilon = 0.1$)
$\varphi(\lambda)\cdot\lambda^2$	average flux at sample
$<b^2>$	average scattering length squared per atom
H_0	$1/d_{min}$
x	$0.5*B/d_{min}^2$
$f(x)$	see Jauch (1997), bottom of p. 165
$<T_H>$	overall Debye-Waller factor
t	time per setting

Figure 3.3.7.2-1 is a plot of data collection times for *MaNDi*. Validation of this approach was achieved by using the published beam time data used for a few protein crystals of known volume from PCS, BIX3 and LADI.

For crystals of deuterated proteins with a volume of 0.125 mm^3, a complete data set for a d_{min} = 2 Å can be obtained from *MaNDi* in a few days (Fig. 3.3.7.2-1). Our calculations indicate that similar amount of beam time will be required to obtain data of similar precision for ~1 mm^3 normal protein crystals. The counting times for a d_{min} = 1.5 Å for the above systems will be an order of magnitude higher than that for d_{min} = 2.0 Å.

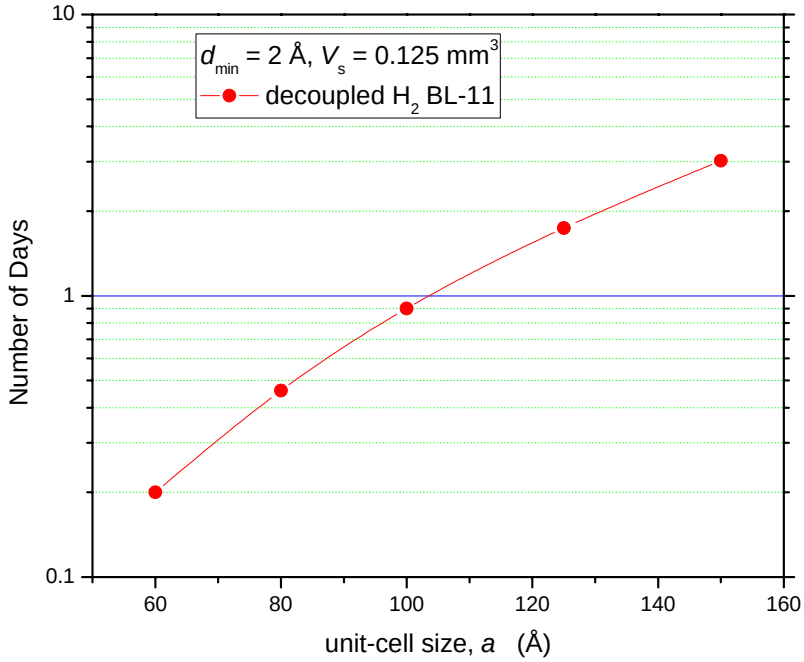

Figure 3.3.7.2-1. Data collection times for MaNDi for 0.125 mm^3 95% deuterated protein crystals with different unit cell dimensions.

3.4 Figures-of-Merit for MaNDi on SNS Beam Lines Viewing Different Moderators

In order to evaluate all possible moderator options for the MaNDi instrument at the SNS, Monte Carlo simulations and calculations of experiment beam times and performance were carried out for the four types of available moderators at the SNS (Table 3.3-1). This treatment takes into consideration of the expectation that most of the crystalline samples will be deuterated and therefore background will not be primarily from incoherent scattering from hydrogen as in equation (23) above. In the case of deuterated crystals, additional background contributions from both ordered and disordered water need to be included as discussed below.

3.4.1 Definition of Figure-of-Merit for a Macromolecular Diffractometer

It is useful to evaluate a figure-of-merit, M, for each design choice. In the case of neutron protein crystal diffraction experiments, the figure of merit should be inversely proportional to experiment duration, D_{expt}, for a given protein crystal of volume, V_{s}. In the regime where all background is intrinsic to the protein crystal Eqn. (24) is the simplest relationship that possesses the required properties.

$$MV_s D_{\text{expt}} = 1 \tag{24}$$

For the collection of a complete data set, which encompasses a hemisphere of reciprocal space out to resolution shell d_{min} of interest (typically d_{min} = 2 Å), the beam time required is

$$D_{\text{expt}} = St \tag{25}$$

where S is the number of different crystal orientation settings and t is the measurement time for a single crystal setting.

The number of crystal orientation settings, S, can be estimated from the usable detector coverage as it sweeps across the outermost reciprocal resolution shell with optimum instrument wavelength band, λ_{min} to λ_{max}. The usable detector coverage is the volume of reciprocal space where neighboring Bragg reflections are separated and is determined by the instrument resolution function and protein crystal unit cell symmetry and dimensions. For the analysis presented here, protein crystals will be assumed to be of primitive symmetry (no systematic absences) and cubic of unit cell dimension a_{c} and volume v_{uc}.

The measurement time for a single crystal setting, t, is dictated by the rate limiting component of the measurement. This, in the case of Laue single crystal time-of-flight technique at a pulsed spallation neutron source, is the measurement of Bragg reflections belonging to the outermost resolution shell with sufficient statistical precision. The Bragg reflections belonging to the inner resolution shells have, on average, greater intensity and therefore for a given measurement time will be determined to a higher precision than the

outer resolution shell reflections. Thus, the measurement time for a single crystal setting can be estimated by combining expressions for signal and background at the outer resolution shell together to form a statistical expression for counting precision.

3.4.2 Intensity of Bragg Peaks

For the purpose of determining required measurement time for a single crystal setting, we can average over the nonsystematic variation of structure factors and use the following expression for average Bragg peak intensity

$$I_{\mathrm{pk}} = t\varphi\varepsilon\kappa N_s \frac{\lambda^4}{2v_{uc}\sin^2\theta}\mathrm{T}_{DW}\left\langle\left|F_{hkl}\right|^2\right\rangle \tag{24}$$

$$= t\varphi\varepsilon\kappa N_s \frac{\lambda^4}{2v_{uc}\sin^2\theta}\mathrm{T}_{DW}\, n_{\mathrm{ord}}\left\langle b_j^2\right\rangle \tag{25}$$

$$= t\varphi\varepsilon\kappa N_s \lambda^4\left[\frac{\mathrm{T}_{DW}}{2\sin^2\theta}\right]\tau_{\mathrm{ord}} \tag{26}$$

where
- I_{pk} = integrated intensity for an average Bragg peak (n)
- t = duration of measurement (s),
- $\varphi(\lambda)$ = incident neutron flux at sample (n.cm^{-2}.s^{-1}.Å^{-1}),
- $\varepsilon(\lambda)$ = detector efficiency,
- κ = conversion factor 1×10^{24} (cm^2.bn^{-1}),
- N_s = no. of unit cells in sample,
- 2θ = Bragg angle for reflection,
- v_{uc} = unit cell volume (Å^3),
- T_{DW} = temperature factor,
- $|F_{\mathrm{hkl}}|^2$ = structure factor modulus of reflection *hkl* squared (bn),
- n_{ord} = number of ordered atoms in a single protein crystal unit-cell
- $\langle b_j^2\rangle$ = mean coherent scattering length of atoms in ordered crystal structure (bn)
- τ_{ord} = $n_{\mathrm{ord}}\left\langle b_j^2\right\rangle / v_{uc}$
  = average ordered crystal structure scattering strength density (bn.Å^{-3}).

For a non-deuterated protein crystal with 35% of the solvent water molecules crystallographically ordered, τ_{ord} = 0.0223 bn·Å^{-3} and similarly, for a fully deuterated protein crystal with D_2O solvent, τ_{ord} = 0.0358 bn·Å^{-3}.

3.4.3 Sample Background

Since, non-deuterated protein crystals require ~10 times more beam time than deuterated crystals it is rational to optimize MaNDi for deuterated crystals. The cost of

protein deuteration by exchange or special synthesis is insignificant when compared to the real cost of extended beam time required. This then necessitates a more detailed model of the intrinsic sample background, rather than assuming that all the background is simply due to the total incoherent scattering cross-section of the protein crystal as in Equation (23).

For estimating Bragg peak precision and consequently counting time required for a single orientation, t, it is the background intensity located beneath a Bragg peak, B_{pk}, which is decisive. This is given by multiplying the background per volume element by the normalized reciprocal volume, where the background includes contributions from ordered atoms, τ_{ord}, disordered atoms, τ_{dis}, and incoherent scattering from all atoms, τ_{inc}:

$$\begin{aligned} B_{\mathrm{pk}} &= B n_{v*} \\ &= t\phi\varepsilon\kappa\lambda^4 N_s \left[T'_{\mathrm{diff}}\,\tau_{\mathrm{ord}} + \tau_{\mathrm{dis}} + \tau_{\mathrm{inc}}\right] n_{v*} \end{aligned} \qquad (29)$$

where n_{v*} = the fraction of reciprocal volume that is used for integration (peak intensity and background)

$$T'_{\mathrm{diff}} = \left\langle \frac{\left(1 - T_{\mathrm{DW}}\right)}{2\sin^2\theta} \right\rangle_{\mathrm{shell}}$$

In Equation (29), n_{v*} will increase as peaks become broadened due to moderator pulse shape, incident beam divergence and crystal mosaicity.

3.4.4 Estimated Performance and Comparison of MaNDi on SNS Beam Lines Viewing Different Moderators

The ultimate design, performance and scientific range of the MaNDi instrument will be intimately tied to the choice of SNS moderator. The Figure-of-Merit analysis and performance estimates presented here are to determine the optimum moderator for a MaNDi instrument and also yield a baseline estimate of performance (measurement time) and range of sample and unit cell sizes. The different moderator types and respective available beam lines compared here are those listed in Table 3.3-1.

Table 3.4.4-1. Protein crystal and beamline layout parameters used in the MC simulations.

	values					
protein crystal						
mosaicity (FWHM, °)	0.2					
strain (FWHM, %)	0.1					
B_{iso} (Å^2)	20.0					
diameter (mm)	1.0					
moderator (beamline)	dec-H_2 (11)		cou-H_2 (5)		HR-H_2O (8) HI-H_2O (17)	
beamline layout	high resolution	medium intensity	high resolution	medium intensity	high resolution	medium intensity
moderator-guide distance (m)	6.0	6.0	6.0	6.0	6.0	6.0
curved guide section (m)	12.0	12.0	12.0	12.0	0.0	0.0
straight guide section (m)	3.0	4.5	54.0†	55.5†	15.0	16.5
guide-sample distance (m)	3.0	1.5	3.0	1.5	3.0	1.5
sample-detector distance (m)	0.5	0.5	0.5	0.5	0.5	0.5
moderator-sample distance (m)	24.0	24.0	75.0	75.0	24.0	24.0

Curved and straight guide sections are of 15 × 15 mm^2 cross-section except † where straight guide section is of ballistic type (first and final 10 m are tapered, central ballistic section is of 25 × 25 mm^2 cross-section).

Monte Carlo simulations for a MaNDi instrument located on the four available beamlines were performed using the IDEAS program. A summary of the protein crystal and beamline layout parameters for each of the instrument configurations simulated is given in Table 3.4.4-1. Principally, the Monte Carlo resolution simulations for each possible instrument configuration map the usable detector coverage (2θ range) as a function of unit cell parameter, a, and outer resolution shell parameter, d_{min}. Such a map is shown in Figure 3.4.4-1 for the medium intensity guide system setting (see Table 3.4.4-1) for protein crystals ranging in unit-cell parameter a = 75 – 200 Å and an outer resolution shell requirement for resolving Bragg peaks of d_{min} = 2 Å.

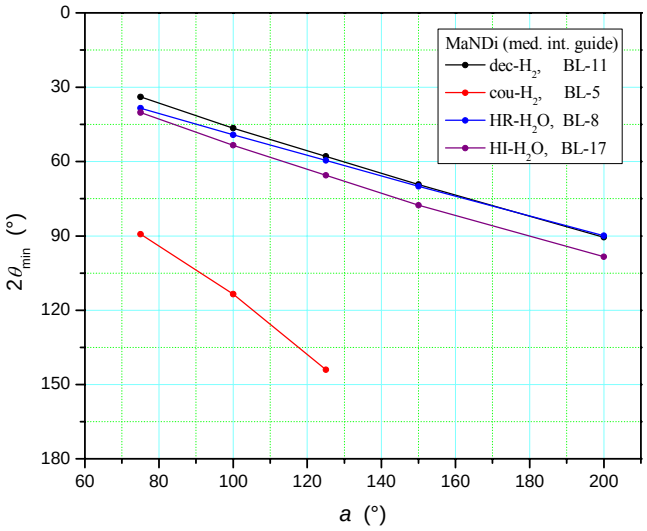

Figure 3.4.4-1. Minimum usable detector angle, $2\theta_{min}$, for resolvable Bragg peaks determined for MaNDi located on the comparison set of SNS beamlines. The Monte Carlo simulations were performed for outer resolution shell d_{min} = 2 Å.

The medium intensity guide setting configuration is appropriate for a wide range of protein unit-cell volumes and is used here to compare the performance of a MaNDi instrument on each of the simulated beamlines. With the supermirror guide configuration set to medium intensity mode the incident neutron divergence is Ω_{inc} = 0.565° × 0.565° for $\lambda \geq 2.0$ Å and the respective neutron fluxes calculated for each beamline are shown in Figure 3.4.4-2. A typical set of outer resolution shell Bragg peaks (d_{min} = 2 Å) revealing the transverse resolution is shown for detector 2θ = 90° module and beamline-11 MaNDi simulation in Figure 3.4.4-3. The spatial widths of the Bragg peaks, all ~ 7 mm, are very close to that estimated from convoluting the neutron incident divergence (FW = 0.565°) with the crystal mosaicity (FW ~ 0.6°) and applying a sample-detector distance of 0.5 m, which yields an expected transverse peak width of 7.2 mm. Using the approach described in the previous section, Figure-of-Merit values for fully deuterated protein crystals were determined for unit-cell size range, a = 100 – 150 Å; these are plotted in Figure 3.4.4-4 and stated also in Table 3.4.4-2. From inspection of Figure 3.4.4-3 it is immediately apparent that the performance of a MaNDi instrument is greatly affected by the choice of beamline/moderator. Comparison between the Figure-of-Merit functions and their respective beamline fluxes (see Figure 3.4.4-2) shows that flux on sample is not the dominant factor driving the performance of a macromolecular diffractometer.

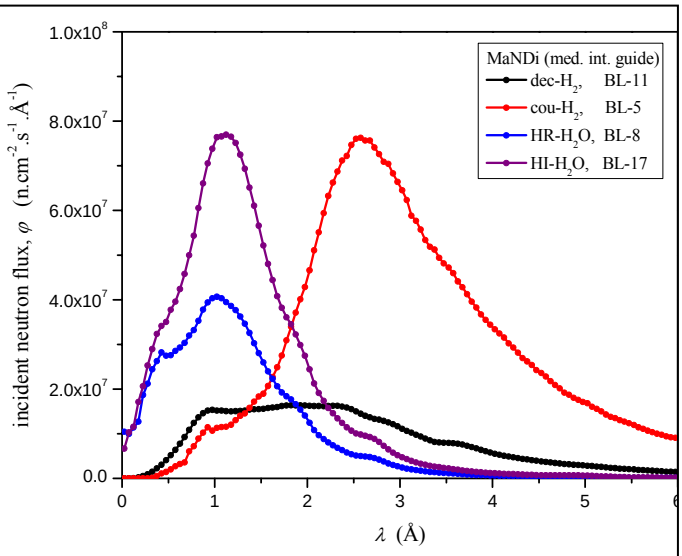

Figure 3.4.4-2. Neutron fluxes at sample for the comparison set of SNS beamlines with medium intensity guide configuration.

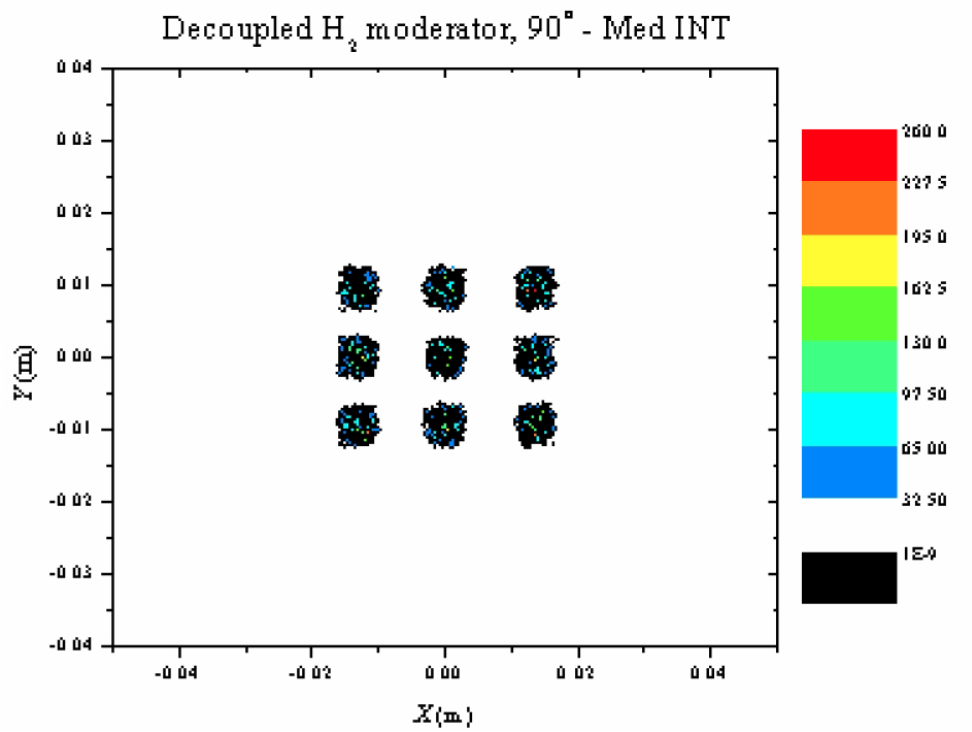

Figure 3.4.4-3. Simulated Bragg peaks at the detector plane calculated for SNS beamline-11 (decoupled-H_2 moderator) for protein crystal with a = 150 Å.

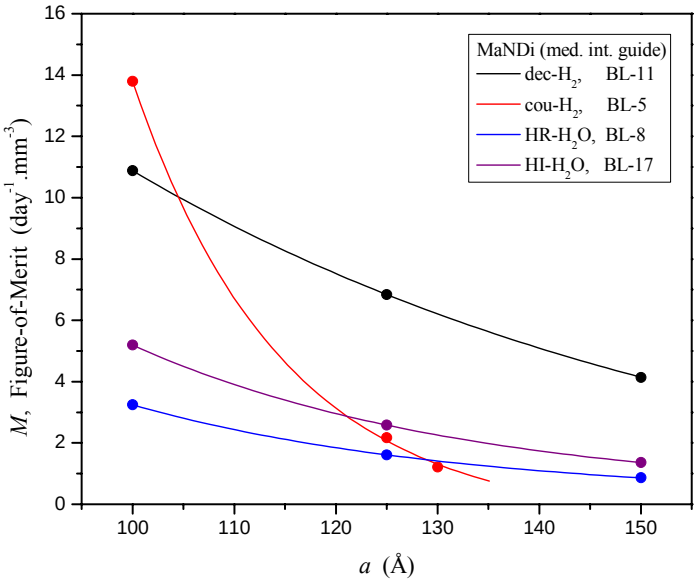

Figure 3.4.4-4. Figure-of-Merit functions determined for fully deuterated protein crystals, d_{min} = 2 Å and MaNDi located on the comparison set of SNS beam lines with medium intensity guide configuration.

Table 3.4.4-2. Figure-of-Merit values and derived measurement time parameters S, t and D_{expt} for fully deuterated protein crystal of volume 0.125 mm^3 and MaNDi located on the comparison set of SNS beam lines with medium intensity guide configuration.

		MaNDi (moderator, beam line)			
		dec-H_2 BL-11	**cou-H_2 BL-5**	**HR-H_2O BL-8**	**HI-H_2O BL-17**
a = 100 Å	M	10.88	13.79	3.24	5.19
	S	1.64	6.44	1.64	1.82
	t	0.45	0.09	1.51	0.85
	D_{expt}	**0.74**	**0.58**	**2.47**	**1.54**
a = 125 Å	M	6.84	2.17	1.61	2.58
	S	1.96	24.00	2.03	2.20
	t	1.17	0.30	4.78	2.75
	D_{expt}	**2.29**	**7.19**	**9.70**	**6.05**
a = 130 Å	M	*6.20*	1.21	*1.41*	*2.25*
	S	2.05	39.20	2.09	2.31
	t	*1.39*	0.37	*5.98*	*3.39*
	D_{expt}	***2.84***	**14.50**	***12.50***	***7.82***
a = 150 Å	M	4.14	-	0.86	1.36
	S	2.39	-	2.39	2.61
	t	2.73	-	13.10	7.60
	D_{expt}	**6.52**	**-**	**31.30**	**19.80**

values in italics are derived by interpolation, see Figure 3.4.4-4.

With consideration to the biological community's desire to reduce the required size of protein crystals for neutron diffraction, by setting V_s = 0.125 mm^3 the time per crystal orientation and overall data collection time can be derived from the above determined Figure-of-Merit values (the number of crystal orientation settings, S, is independent of sample volume). The respective values are given in Table 3.4.4-2.

The calculated performance of each MaNDi instrument is best represented and assessed by a plot of estimated experiment duration versus protein unit-cell parameter; this is shown in Figure 3.4.4-5. *Clearly, the performance of a MaNDi instrument located on the decoupled cryogenic-H_2 moderator beamline-11 is far superior to all the other candidate beamlines shown.* The difference in performance between the beamline choices is revealed by charting each detector band contribution, M_{band}, to the overall Figure-of-Merit, as shown in Figure 3.4.4-6 for a = 100 Å. Selecting a coupled cryogenic-H_2 beamline-5 for MaNDi would lead to the quickest measurement times for a single orientation, as signified by the highest $M_{band}/\Delta 2\theta$ line in Figure 3.4.4-6. However, this choice of moderator imposes broad Bragg peaks in time (poor longitudinal resolution) and reduced usable detector coverage. Consequently, the sum under the curve, which is the Figure-of-Merit, is not as high as might otherwise be expected. For the two beamlines 8 and 17 served by ambient-H_2O moderators, the difference between their performances is determined almost exclusively by the much higher neutron flux of beamline-17. However, the peak in effective flux occurs around λ = 1.55 Å, and this is unfavorable to overall instrument performance in two ways. First, the effective flux peak at λ = 1.55 Å leads to a peak in the $M_{band}/\Delta 2\theta$ function at $2\theta \sim 50°$ and due to instrument

resolution boundary conditions (see Figure 3.4.4-2) only one side of this function contributes to the overall Figure-of-Merit, see Figure 3.4.4-6. Second, independent of neutron flux, the M_{band} values at the forward scattering angles, $2\theta \sim 50°$, are relatively low because of the high peak integration volumes, n_{v*} approaches unity, and consequently much higher background integrated under the peaks (compared to respective M_{band} value at $2\theta = 90°$ appropriate for the cryogenic-H_2 moderators).

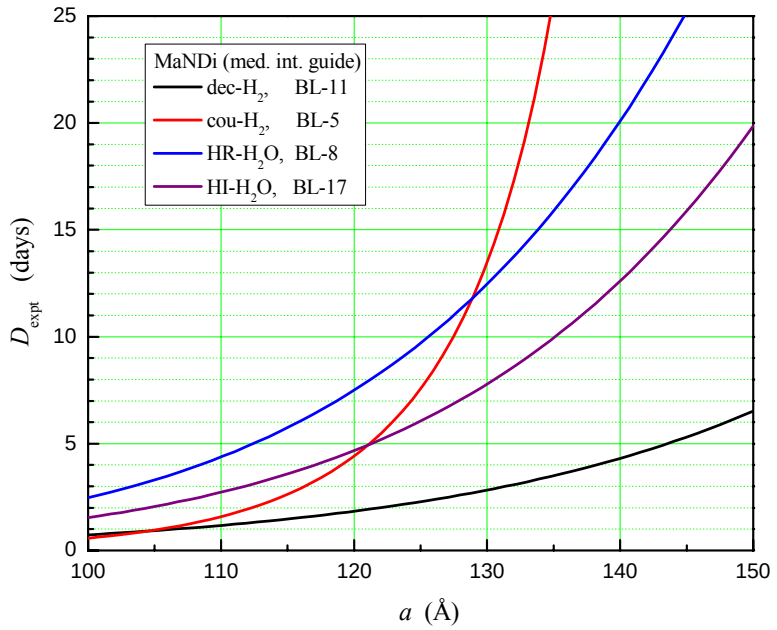

Figure 3.4.4-5. Estimated experiment durations as a function of protein unit-cell parameter for a fully deuterated protein crystal of volume 0.125 mm^3, d_{min} = 2 Å and MaNDi located on the comparison set of SNS beam lines with medium intensity guide configuration.

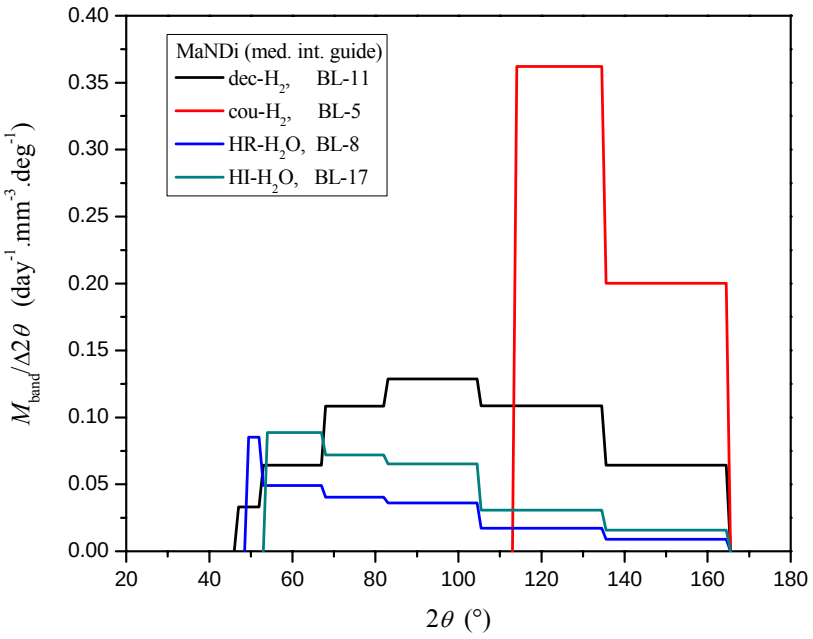

Figure 3.4.4-6. Figure-of-Merit contributions from the individual bands of detector coverage

Fundamentally, the superior performance of MaNDi located on the decoupled cryogenic-H_2 moderator beamline-11 is because this combination avoids the serious detrimental factors discussed above for the other beamline choices. With a peak in effective flux at $\lambda \sim 3.1$ Å for beamline-11, the $M_{band}/\Delta 2\theta$ function is peaked close to the center of usable detector coverage, and consequently both sides of this peaked function contribute to the overall figure-of-merit. The large usable detector coverage results in the lowest number of different crystal orientation measurements required to complete a full hemisphere of data collection. Significantly, and differing from all the other candidate beamlines, the lower resolution boundary, $2\theta_{min}$, for *MaNDi* on beamline-11 occurs away from the peak in the $M_{band}/\Delta 2\theta$ function, resulting in the lowest rise (gradient) in estimated experiment durations versus protein unit-cell parameter (see Figure 3.8.4-5).

It is of interest to compare the results in Figure 3.8.4-5 with those in Figure 3.3.7.2-1, which is based on Equation (23). For smaller unit cell crystals, the predicted experiment times are almost identical. For crystals with larger unit cells, the experiment beam time is higher by a factor of 2 when all the background contributions are considered (Fig. 3.8.4-5). *However, the overall consistency of these results gives us confidence in their validity.*

The results indicate that for both the coupled and decoupled moderators, experiment duration times for small unit cells are on the order of a day or two. *For large unit cells, the decoupled moderator has a clear advantage since counting times can be a few days for the decoupled moderator versus a few weeks for the coupled moderator. Thus it is clear that the decoupled hydrogen moderator is the best choice for the MaNDi instrument.*

DEVELOPMENT OF METHODS AND FACILITIES TO SUPPORT NMC STUDIES

4.1 Total Deuteration of Proteins

Neutron protein crystallography provides a unique non-destructive tool that is able to probe the structure and dynamics of macromolecules and their complexes, providing important information on the position of hydrogen atoms that is often difficult – or impossible – to obtain by X-ray scattering alone. Hydrogen atoms and/or its deuterium isotope are readily located in a neutron analysis because the scattering amplitudes of hydrogen (-0.37 fm) and deuterium (+0.67 fm) are closely similar to those of other common biological atoms, carbon (+0.66 fm), nitrogen (+0.94 fm), oxygen (+0.58 fm) and sulfur (+0.28 fm). Hydrogen atom positions appear as characteristic negative density peaks in neutron density maps whilst the positive density at deuterium atom positions render these as visible as (and indistinguishable from) carbon atoms in neutron protein structures. The difference in amplitude and phase mean that hydrogen and deuterium atoms can be distinguished in neutron protein structures, even at medium resolutions of 2.0 Å, providing often unique information and insight into catalysis, protein-ligand interactions and the protein-solvent interface. However, neutron diffraction analysis suffers from a large hydrogen incoherent scattering background that seriously reduces the signal to noise ratio of the data than can be collected and places limitations on sample size, data collection times, the interpretation of the data, and the quality of the final analysis.

The major challenge confronting neutron protein crystallography is the requirement for often large sample sizes (> $1mm^3$) that are needed to compensate the relatively low flux of available neutron beams. This is further exacerbated by the large incoherent scattering background from hydrogen in the solvent and in the macromolecule itself, which ultimately limits the resolution of the data that can be obtained. The incoherent scattering cross-section of hydrogen for neutrons of 80.27 barns is anomalously large, especially when compared with the cross section of deuterium, which is just 2.07 barns, and of the other light atoms carbon (0.0 barns), nitrogen (0.49 barns) and oxygen (0.0 barns). Replacing hydrogen with its deuterium isotope in biological systems thus greatly reduces the incoherent scattering background in these experiments and delivers better than an order of magnitude improvement in signal to noise.

In neutron protein crystallography, these gains are realized by deuterating the sample, either partially, by soaking protein crystals in deuterated mother liquor, or more fully, by preparing fully deuterium labeled protein samples by using modern molecular biology techniques. It is relatively straightforward to replace H_2O solvent by D_2O in protein crystals and since the solvent content is rather large – typically 50-60% - this exchange results in a significant decrease in the hydrogen incoherent scattering background of 2-3 fold. However, there is still a large problem arising from the hydrogen that is covalently bound to carbon atoms in the structure.

These problems can be overcome by production of fully D-labeled protein. Full perdeuteration of protein crystals provides an order of magnitude improvement in signal

to noise over hydrogenated systems. This enables smaller crystals and larger unit cell problems to be tackled. Perdeuteration also enhances the visibility of deuterium atom and water positions in the resulting maps. In hydrogenous materials for example, cancellation between the negative scattering density of hydrogen atoms and the positive scattering densities of the atoms to which they are bound can reduce the visibility of important functional groups in medium resolution analyses. This contrasts strongly with the analysis of deuterium labeled materials, where the strong reinforcement of positive scattering density between deuterium and neighboring atoms can greatly enhance their visibility.

These benefits have been demonstrated in experiments on perdeuterated myoglobin and on perdeuterated DNA. In their work on deuterated myoglobin, Shu *et al.* (Shu *et al.*, 2000) compare a density map based on X-ray data, in which hydrogen atoms are not visible, even at a resolution of 1.5 Å, with neutron density maps for hydrogenated protein, where hydrogen atoms can be seen but there are problems associated with cancellation of the negative density from hydrogen and positive density from the surrounding atoms, and finally with maps obtained from perdeuterated myoglobin, where deuterium and carbon positions are all clearly visible.

Provision of perdeuterated protein crystals will provide order of magnitude gains in the signal/noise ratio of data collected on the *MaNDi* instrument. This will allow data to be collected more rapidly from smaller crystals of larger and more complex biological systems. Together with improvements in instrumentation, isotope labeling will improve signal/noise ratios and reduce the size limitations that have complicated such applications in the past and will - in many cases - provide new, more sophisticated and more powerful approaches to complex problems in biology.

4.1.1 Production of Deuterated Protein

Perdeuterated protein is produced by endogenous expression of recombinant proteins in bacterial systems grown in D_2O solution using deuterated carbon sources. The positions of deuterium atoms in proteins resulting from biosynthetic incorporation are shown in Figure 4.1.1-1. This can normally be achieved quite readily for recombinant protein overexpression in systems that are well behaved in standard hydrogenated and H_2O media, but may require additional adaptation and development for systems where protein yields in hydrogenated media are atypically low (<< µg-mg/L). The usual steps in this process require first that competent cells be adapted to growth in deuterated media. This can be achieved in several

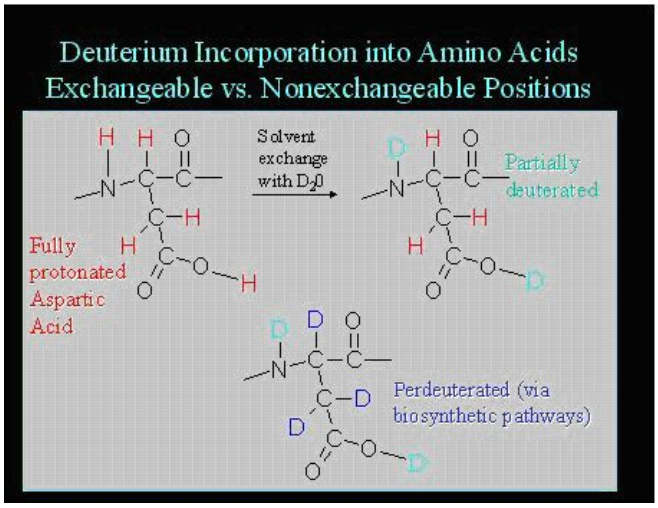

Figure 4.1.1-1. Incorporation of deuterium in proteins via biosynthetic incorporation and deuterium exchange.

ways, either by gradual step-wise increase in D_2O concentration or, more directly, by plating cells on media of choice and selecting only those colonies that perform best for subsequent culture and inoculation. Scale up growth and expression is then typically performed in standard shaker flasks using either commercial or 'home-grown' rich media (derived, for example, from cell lysates produced from algae grown in D_2O) or under more controlled conditions in defined minimal media. Cell grow is typically slower in deuterated media (< 5 times slower) and yields are correspondingly lower. Efforts at some central facilities have focused on developing methods for high cell density culture in fomenters that aim to improve yield and reduce costs. Once the target protein has been expressed, purification proceeds by the protocols developed for the hydrogenated protein. The deuteration levels of the final product are determined by mass spectrometry.

Whilst it is known that deuteration and more general H/D- isotope exchange can have subtle effects on the physiochemical properties of proteins, the crystallization behavior of perdeuterated and hydrogenated proteins are normally very closely similar and crystallization conditions are readily re-optimized using minimal amounts of perdeuterated protein. A number of high resolution X-ray and studies have demonstrated that the H and D labeled proteins examined are structurally isomorphous.

4.1.2 Deuteration Facilities for the Life Sciences

The expertise and facilities required to produce these D-labeled materials typically resides in small specialized groups working independently (& in isolation) on individual problems and is often inaccessible to new or casual users. This presents a significant "potential barrier" for new, occasional or latent users wishing to use neutron scattering techniques who lack the time, resources and/or expertise to produce labeled macromolecules. Providing users with the tools and facilities needed to produce deuterated material would enhance both the quality and quantity of neutron experiments that can be done at the *MaNDi* instrument at SNS (and for example at the PCS instrument at LANL) and would, in many cases, make feasible new and more powerful experiments than can presently be performed. The requirements for D-labeled materials are so fundamental that during the October 2003 *MaNDi* workshop, it was concluded that serious effort should be made to coordinate these activities and to explore possibilities for provision of central facilities and infrastructure for production of H-D labeled materials at SNS.

A pilot phase **Deuteration Laboratory** will be developed at ORNL in 2004 that would provide user access to the expertise and facilities necessary to prepare specifically H/D-labeled biological macromolecules for *ALL* neutron scattering applications, including production of deuterated protein for *MaNDi*. This facility will aim to:

- Provide scale-up and support facilities for *in vivo* and *in vitro* production of perdeuterated proteins/nucleic acids and other labeled bio-molecules.
- Optimize labeling strategies for readily expressed proteins and lead process development for the more difficult ones (e.g. labeled membrane proteins).

- Serve as a repository, maintainer and distributor of the expertise/systems and materials produced by the community.
- Train researchers in application of these techniques

This will provide user access to H/D-labeled materials that are precisely designed and tailored for even more demanding and innovative applications. Critically, such a facility would create a "point of access" for the wider (latent) community of structural biologists who are non-expert neutron scatterers and would introduce and train a new generation of users in application of these powerful techniques. D-labeling would therefore (i) increase throughput & efficiency and (ii) improve signal/noise & reduce size limitations (e.g. by >10 in diffraction) that have restricted the use of neutron protein crystallography in the past. Below is an example of a system under development by an IDT member who has successfully incorporated deuterium into an enzyme of important pharmaceutical interest.

4.1.3 Perdeuteration of *E. coli* Chromosomal DHFR

Structures of enzyme-ligand complexes have been extremely useful in helping to elucidate catalytic mechanisms. The contribution made by hydrogen atoms to biological function cannot be overstated. For instance, invariably a hydrogen atom is required to facilitate catalysis. Structural studies by neutron diffraction permit elucidation of H/D exchange, which in turn enables us to understand catalytic processes at the molecular level. Here we plan to study important steps in the catalytic mechanism of the ubiquitous metabolic enzyme, dihydrofolate reductase (DHFR). Chromosomal dihydrofolate reductase is important in one carbon metabolism and is an important target for drug design efforts. Despite the many structural and kinetic studies of the *E. coli* DHFR mechanism, a crucial question concerns the protonation state of the conserved Asp27 residue in the active site as well as the protonation state of the bound substrate, dihydrofolate (DHF) or inhibitors such as methotrexate (MTX). pH profiles of the catalytic hydride transfer step indicate a pKa of 6.5 (Feirke *et al.*, 1987). Does this titration describe a perturbed pKa for Asp27? Site-directed mutagenesis studies utilizing a D27S mutant indicated an approximately 3,000-fold decrease in catalytic efficiency at pH 7 (Howell *et al.*, 1986). As the pH was decreased to 5, catalytic efficiency was increased, suggesting that the D27S mutant bypassed the need for a proton donor by binding pre-protonated substrate, which becomes more available in solution as its pKa of 2.59 is approached (Maharaj *et al.*, 1990). An alternate hypothesis, based on resonance Raman studies of wild type and D27S DHFRs, suggests DHF becomes protonated upon binding to wild-type DHFR but not D27S DHFR (Chen *et al.*, 1994b). These results suggest Asp27 helps facilitate altering the N5 pKa of DHF to 6.5 when bound to the enzyme. In this scenario, the kinetic pKa of 6.5 describes the protonation state of bound substrate.

Currently we have been focusing on DHFR bound to MTX, an anti-cancer drug that is a competitive inhibitor of DHF. We would also like to independently determine the protonation state of Asp27 in a ternary complex with folate and NADP+ using neutron diffraction. This approach uses a folate~$NADP^+$ complex to mimic the productive ternary complex. While we will be unable to determine the keto/enol

tautomer state of substrate, we should be able to determine the ionization state of Asp27. Although there exists NMR and X-ray crystallographic data on these complexes (Howell *et al.*, 1986), neutron diffraction structures will help to accurately determine the true protonation states of the active site residues of DHFR, the catalytically important water molecules, and bound ligands at the reactive cleft of DHFR.

The biochemical protocols involving protein expression and purification have recently become available. The DHFR-MTX complex crystals have been grown to a size of 0.3-1.0 mm^3. After H/D exchange for more than a month, these crystals were examined in neutron diffraction experiments at the ILL. Data were observed to 2.5 Å resolution. To obtain higher resolution data, we are also actively crystallizing perdeuterated DHFR in complex with the different ligands. Crystals of the MTX complex with volumes of > 0.1 mm^3 (a 1:10 reduction in volume relative to native crystals) have been produced. Perdeuteration should dramatically improve the signal to noise in our data and help in determining the hydrogen positions in the protein. Recently data were collected to 2.2 Å resolution using 0.14 mm^3 crystals of aldose reductase (reported at the Higher Resolution Drug Design meeting, Bischenberg, France, May 2004). This experiment shows that neutron diffraction data can be collected on perdeuterated DHFR-MTX co-crystals that are $1/10^{th}$ the volume of native crystals. We are in the process of expanding perdeuterated cell growth to obtain sufficient amounts of protein for obtaining even larger perdeuterated crystals suitable for neutron diffraction experiments.

4.2 Growth of Large Crystals for Neutron Macromolecular Crystallography

Due to the low flux available at the current sources neutron macromolecular crystallography requires large protein crystals with a volume > 2 mm^3. Although the higher flux at MaNDi at SNS will enable data collection in a few days with smaller deuterated macromolecular crystals with a volume of 0.125 mm^3, it will be desirable to have larger volume crystals for studies of larger complexes and/or high resolution. A rational way to determine the proper condition to grow large single crystals is to first determine the complete crystallization phase diagram including solubility curve. Typically large single crystals are grown under the supersaturated phase close to the solubility curve (Arai *et al.*, 2002).

In general, very slow undisturbed growth of crystals for several months, and large amounts of proteins, are considered to be necessary for growth of large single crystals. However, with the knowledge of the physical chemical parameters of the crystallization process, well-ordered large single crystals can be grown in shorter times.

As an example, crystallization studies carried out on Photosystem I are described below. The techniques described will in general be useful for most systems. This trimeric complex Photosystem I with a molecular weight of 1000 kDa is the largest and most complex membrane protein crystallized to date. Each monomeric unit contains 12 proteins to which 127 cofactors are non-covalently bound. Figure 4.2-1 shows a simplified picture of Photosystem I. Only the backbone of the protein and head groups of the cofactors are shown for clarity (Jordan *et al.*, 2001).

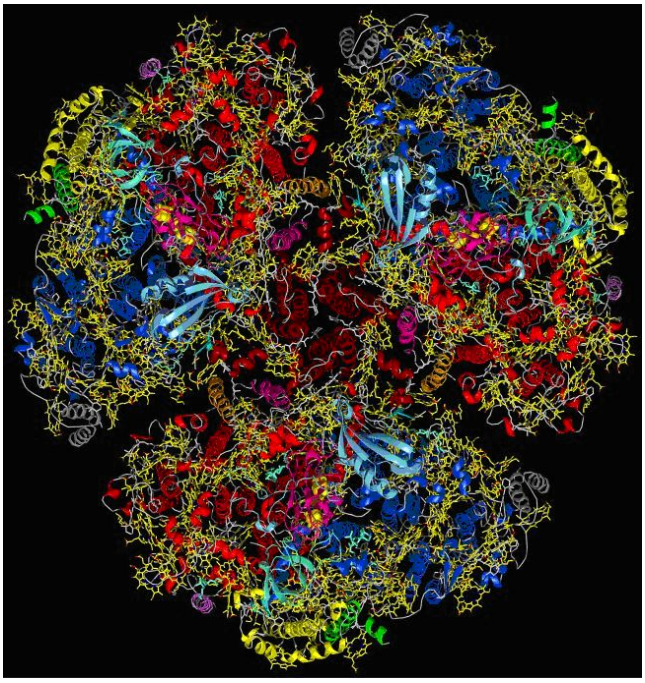

Figure 4.2-1. Structure of Photosystem I at 2.5 Å resolution.

The protein is crystallized by dialysis against low ionic strength as described in (Fromme, 1998; Fromme, 2003). The space group is $P6_3$, with cell dimensions of $a = b = 288$ Å and $c = 167$ Å. The packing of PS I in the unit cell is shown in Figure 4.2-2. The protein interactions in the unit cell are very weak, with a solvent content of 78%, and less than 2% of the protein surface is involved in crystal contact, i.e., only four salt bridges are involved in crystal contact.

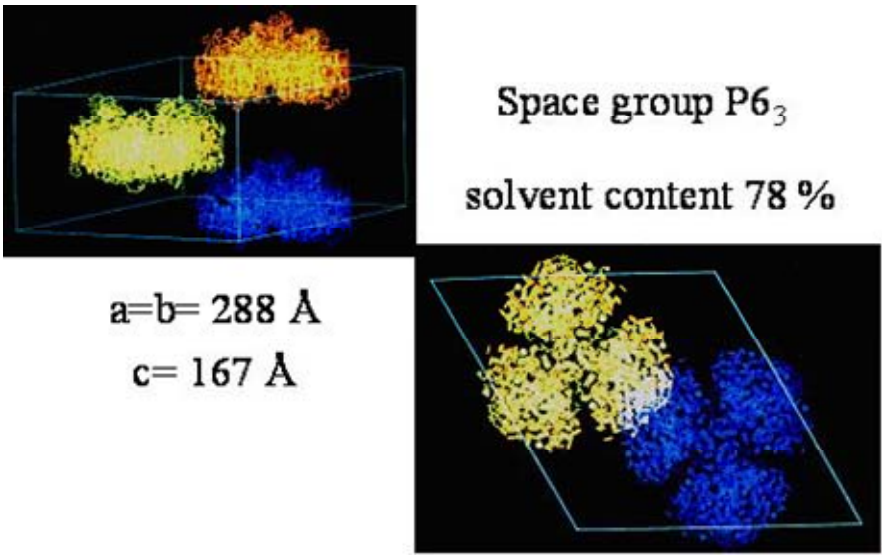

Figure 4.2-2. Crystal packing of Photosystem I

Crystallization under microgravity. The first evidence for the possibility to grow large single crystals came from crystallization experiments under microgravity. Photosystem I was successfully crystallized at the USML-2 and the STS-95 mission under microgravity. Crystals 1.5 mm in diameter and 4 mm long were grown under microgravity in two weeks. These were 20 times larger than any that had previously obtained from Photosystem I on earth. The crystals also showed an increased resolution and a decreased mosaic spread (Fromme, 1998; Klukas *et al.*, 1999a; Klukas *et al.*, 1999b; Fromme, 2003). Even if the microgravity environment is very favorable for the growth of large single crystals, the options for performing these experiments are limited by the flight opportunities and are very cost-intensive. For this reason, new methods were developed to improve the size and quality of Photosystem I crystals grown on earth.

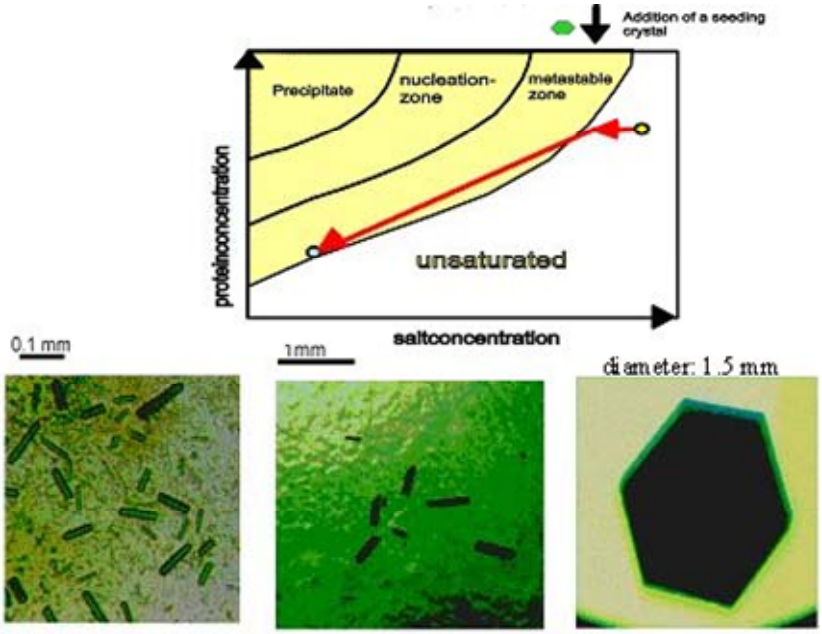

Figure 4.2-3. Schematic phase diagram of the solubility of Photosystem I as a function of salt concentration.

Growth of large single crystals for NMC by the use of seeding techniques. The determination of the phase diagram for the solubility of proteins enables growth of large single crystals by the combination of micro- and macroseeding techniques. Figure 4.2-3 shows the schematic phase diagram of the solubility of Photosystem I as a function of salt concentration.

1) In the first step, small PS I crystals (diameter ≈ 0.05 mm, length ≈ 0.1 mm) were grown by spontaneous nucleation. The protein solution was brought into the nucleation zone either by decreasing the salt or increasing the protein concentration. In this step, large amounts of small PS I crystals grow over night. They are shown in Figure 4.2-3 (bottom left).

2) In the second step, the small PS I crystals were used for microseeding. The protein solution was brought into the meta-stable zone by decreasing the salt concentration using microdialysis. After one day of equilibration, 0.5 µl of a solution containing 5-20 microcrystals was added and over a period of two days the salt concentration was further reduced by microdialysis to the final concentration. In this step 10-20 medium size crystals (diameter ≈ 0.1, length ≈ 0.1-0.3 mm) grew within 2 days. They are shown in Figure 4.2-3 (bottom, center).

3.) The third crystallisation step uses the medium size crystals for macroseeding. The salt concentration of the protein solution was slightly reduced to a concentration where the solution is still unsaturated but is close to the border of the saturation curve. When the solution had been equilibrated for one day, one single crystal of medium size was added. Dialysis against lower salt concentration started immediately. The crystal initially begins to dissolve. The partial dissolving of the seeding crystal is essential to provide fresh rough surface planes for the further growth of the crystal. Thereby secondary nucleation at the crystal surface is avoided. As the salt concentration decreases, the solution becomes supersaturated and the crystal grows. Using this procedure one large single crystal grows in the protein solution (80 mg/ml) within 2-3 days, using a volume of only 5 µl. Most frequently hexagonal needles of diameter 0.5 mm and length up to 3 mm are obtained. Hexagonal plates also are observed, although these occur less frequently (one of these plates is shown in Figure 4.2-3 bottom right). Crystals diffracting X-rays to 2.5 Å resolution, grown using this seeding procedure, formed the basis for the high resolution X-ray (Jordan *et al.*, 2001) and neutron diffraction experiments on Photosystem I.

4.3 Low Temperature NMC

4.3.1 Overview of Current Technology

The role of NMC will be to resolve the positions of hydrogen atoms at the active sites, the protonation states of certain moieties and the locations of bound water molecules. The pioneering work of Wlodawer and Hendrickson (Wlodawer & Hendrickson, 1982) clearly demonstrated that the simultaneous refinement of the data from NMC and X-ray macromolecular crystallography (XMC) results in more information content than either type of data alone. The complementarity of XMC and NMC has been exploited in several studies including bovine pancreas trypsin inhibitor (Wlodawer *et al.*, 1984), ribonuclease A:uridine vanadate complex (Borah *et al.*, 1985), and insulin (Wlodawer *et al.*, 1989). Recent studies by Helliwell's group (Deacon *et al.*, 1997; Habash *et al.*, 2000) on the sugar binding protein concanavalin A have clearly shown the power of using both NMC and UHRMXC (Deacon *et al.*, 1997) in resolving more bound water molecules than with UHRMXC alone. For instance, the NMC study of concanavalin A (Habash *et al.*, 2000) revealed the positions of over 62 bound D_2O molecules when compared to only 12 H_2O molecules by UHRXMC.

The expansion of opportunities with *MaNDi* will bring a concomitant demand for low temperature NMC studies. Experiments currently underway have shown the feasibility of low temperature studies, enabling NMC practitioners to more directly utilize

the low-temperature XMC structures as a basis for neutron structure refinement, and to derive the many benefits seen in low temperature X-ray studies, including greatly improved diffraction patterns, and the ability to do freeze trapping of reaction intermediates. .

In XMC, low temperature studies (understood to be those where crystals are cooled cryogenically, to lock and preserve the solvent in an amorphous state, usually at or below 100K) have lead to improved diffraction from well-ordered crystals. This is a direct consequence of the decrease in the atomic thermal parameters. Because of improved diffraction resolution, and extended lifetime from reduced free radical migration following exposure to ionizing radiation, low temperature data measurement has become a standard procedure for XMC. Whilst thermal neutrons do not cause observable damage to macromolecular crystals, comparable improvements in diffraction quality would mean that measurements may be obtained with smaller crystals, or alternatively higher resolution may be achieved with crystals of comparable size than otherwise would be possible at room temperature.

The unit cell parameters from the X-ray diffraction data are used to reduce and refine the neutron diffraction data, and the molecular coordinates are used for initial model building and structural refinement. In order to optimally utilize the neutron diffraction data an X-ray data set collected under similar conditions is desirable, especially since this provides the most reliable structure as a starting model in refinement. A number of very large crystals (> 1 mm^3) have been successfully cooled and maintained cryogenically at 12 K with a combination of liquid nitrogen plunge and DISPLEX refrigerator in Grenoble at the ILL LADI beam line. These 20+ crystals from four different proteins have been reliably diffracting to between 1.6 and 2.5 Å resolution. If the opportunity exists it should be possible to follow a strategy pioneered at ILL and do XMC on the same crystal after neutron data measurement is complete, thus affording an opportunity to use both X-ray and neutron diffraction to determine the structure, providing more reliable structural information.

As stated elsewhere, neutron diffraction instruments have been and will most likely continue to be oversubscribed even after *MaNDi* is built. As more successful neutron experiments are reported, and the power of neutron diffraction is better understood, this strain on resources is likely to result in an increase in the lag time between crystal growth and data collection. To minimize the effects of limited timely access to diffraction instrumentation, low temperature storage of crystals can be an option so that crystals can still be harvested at their peak size and quality. Although most protein crystals are sufficiently robust to survive the extended data measurement times associated with NMC, in some cases complete data sets have been unobtainable due to crystal dissolution during data collection, e.g. in the case of hemoglobin. Low temperature storage and data measurement would make this moot for even the most sensitive crystals.

Low temperature NMC studies are expected to have high impact. Contributions to mechanistic understanding and reaction intermediate structure will be a natural

consequence from low temperature NMC, possibly to an even greater extent than has been possible with XMC, since neutrons can image hydrogen so much more efficiently. Freeze-trapping studies with neutrons become possible with low temperature data measurement. Important early studies already underway seek comparison of water positions and water structure at room and low temperatures, to gain a better understanding of how low temperature structures and conditions may differ from structures and conditions more close to physiological. The neutron mechanistic studies could examine proton transfer; dynamics of H/D exchange, and aspects of the solvent structure surround the protein.

Currently low temperature NMC serves primarily as an adjunct to other research objectives. As mentioned, promising methodologies are under development to reliably bring large crystals to cryogenic temperatures. Additional work is needed on reproducible flash cooling protocols for large crystals with higher solvent contents and solvent channel sizes that will preserve low crystal mosaicity and avoid the formation of ice within the crystal lattice. Aspects of this research will include determining the most efficient mechanisms (cryogens, cryogen temperatures, and crystal cooling protocols) for reducing the crystal temperature to vitrify solvent without disrupting the lattice. One feature that will ease issues of flash-cooling large crystals is the use of perdeuterated proteins, since this will significantly lower the required crystal volume. Recently a 0.14 mm^3 perdeuterated protein crystal was sufficient for full data collection at the ILL LADI instrument. This is well within limits for standard XMC flash-cooling protocols.

4.3.2 Low temperature Freezing of Large Macromolecular Crystals for Neutron Diffraction

The majority of NMC data sets obtained to date have been collected at room temperature, because the freezing of large single crystals has been considered to be a serious challenge. In freezing of large single crystals for neutron diffraction, there are two parameters that are important to consider: 1) the stabilization of the crystals in the cryo-solution, and 2) the speed of freezing.

1) In large single crystals, the diffusion of the cryo-protectant into the protein crystal is an important factor that must be taken into account. Experiments with large Photosystem I crystals (> 1 mm), frozen for EPR and X-ray experiments (Brettel *et al.*, 1992; Kamlowski *et al.*, 1997a; Jordan *et al.*, 2001), have shown that these can be successfully handled. However, at least one hour is required for the solvent cavities inside the crystal to be equilibrated with the cryo-protectant. Photosystem I possesses a high solvent content of 78% and diffusion occurs via large pores. Crystals with lower solvent content may show an even slower diffusion rate and may therefore require an even longer time for full equilibration. Another important point is that mechanical stress must be limited by reducing the rate of change in the concentration of the cryo-protectant inside the crystal. This can ideally be achieved by growing the crystals in the presence of cryo-protectant. Alternatively, crystals can be brought into the cryo-protectant solution by

means of stepwise increase of the cryo-protectant concentration or dialysis against the cryo-protectant solution.

2) The speed of the freezing process is also very critical for large single crystals. The use of liquid propane as a refrigerant can increase the velocity of freezing. Propane has a much higher thermal conductivity than air or liquid nitrogen, because propane does not show the "Leidenforst phenomena" (Chandra & Aziz, 1994). The heat-transfer coefficients of liquid nitrogen and liquid propane differ by a factor of 30 (Serp *et al.*, 2002).

The procedure to freeze large single crystals in liquid propane is now described briefly. We were able to freeze Photosystem I crystals of > 1 mm size for EPR and ENDOR experiments using this procedure (Brettel *et al.*, 1992; Brettel, 1997; Kamlowski *et al.*, 1997a; Kamlowski *et al.*, 1997b; Kamlowski *et al.*, 1998).

Pure propane gas (99.9999%) is liquefied by cooling in a gas-trap down to liquid nitrogen temperatures. Cryo vials (Hampton research) are filled with liquid propane and stored in liquid nitrogen. The crystals are mounted in large cryo-loops made either of nylon or hair. The mounted crystals are immediately flash frozen in propane and stored until the propane solidifies. In this way, a cylinder of solid propane surrounds the crystals and also prevents the crystal droplet from falling out of the loop for transport. The transport from the storage container into the cryo stream at the neutron beamline is also easily achieved, because the propane cylinder prevents the melting of the crystal during transfer.

CONCLUSIONS

Neutron Macromolecular Crystallography (NMC) is able to accurately determine proton locations, protonation states and hydration, and hydrogen/deuterium exchange in macromolecular crystals even at a moderate resolution (2 Å to 2.5 Å). In order to exploit the high neutron flux that will become available beginning in 2006 at the Spallation Neutron Source (SNS), it is proposed to develop a dedicated best-in-class high throughput and high resolution time-of-flight single crystal macromolecular neutron diffractometer (*MaNDi*) at the SNS. *MaNDi* is being designed to be able to collect a full hemisphere of Bragg data with a resolution of 1.5 to 2 Å on a crystal with a lattice constant up to 150 Å in a few days. A thorough evaluation of the instrument performance at different moderators using analytical equations and Monte-Carlo simulations show that the decoupled hydrogen moderator at SNS would be the best choice for *MaNDi*. State-of-the-art neutron guides and optics will be used for efficient beam transport and optimization of collimation at the sample. To reduce the radiation damage and the instrument background, a curved guide will be used to steer the beam gently so that the crystal will be out of line of sight of the moderator. The high throughput is accomplished by the use of a wide bandwidth of cold neutrons (1.8 Å < λ < 4.5 Å) sorted by time-of-flight and by an array of high resolution position-sensitive area detectors covering a large solid angle. It is expected that the unprecedented high data rates and resolution with *MaNDi* for the high resolution NMC will open up new avenues and greatly advance the field of structural biology.

REFERENCES

Afonine, P. V., V. Y. Lunin, N. Mezet and Urzhumtsev (2004). "On the possibility of the observation of valence electron density for individual bonds in proteins in conventional difference maps." Acta Cryst. D **60**: 260-274.

Agre, P., L. S. King, M. Yasui, W. B. Guggino, O. P. Otterson, Y. Fujiyoshi, A. Engel and S. Nielsen (2002). "Aquaporin water channels - from atomic structure to clinical medicine." J. Physiol. (London) **542**(1): 3-16.

Agre, P. and D. Kozono (2003). "Aquaporin water channels: Molecular mechanisms for human diseases." FEBS Lett. **555**: 72-78.

Arai, S., T. Chatake, Y. Minezaki and N. Niimura (2002). "Crystallization of a large single crystal of a B-DNA decamer for a neutron diffraction experiment by the phase-diagram technique." Acta Cryst. D **58**: 151-153.

Austin, R. H., K. W. Beeson, L. Eisenstein, H. Frauenfelder and I. C. Gunsalus (1975). "Dynamics of ligand binding to myoglobin." Biochemistry **14**(24): 5355-5373.

Badger, J. (1996). "Determination of protein and solvent volumes in protein crystals from contrast variation data." Neutrons in Biology, Basic Life Sciences. B. P. Schoenborn and R. B. Knott. New York, Plenum Press. **64:** 333-343.

Bentley, G. A., J. T. Finch and A. Lewit-Bentley (1981). "Neutron diffraction studies on crystals of nucleosome cores using contrast variation." J. Mol. Biol. **145**: 771-784.

Bentley, G. A., A. Lewit-Bentley, J. T. Finch, A. D. Podjarny and M. Roth (1984). "Crystal structure of the nucleosome core particle at 16 Å resolution." J. Mol. Biol. **176**: 55-76.

Berisio, R., V. S. Lamzin, F. Sica, K. S. Wilson, A. Zagari and L. Mazzarella (1999). "Protein titration in the crystal state." J. Mol. Biol. **292**: 845-854.

Betts, L., S. Xiang, S. A. Short, R. Wolfenden and C. W. Carter, Jr. (1994). "Cytidine deaminase. The 2·3 Å crystal structure of an enzyme: transition-state analog complex." J. Mol. Biol. **235**: 635-656.

Bolduc, J. M., D. H. Dyer, W. G. Scott, P. Singer, R. M. Sweet, D. E. Koshland, Jr. and B. L. Stoddard (1995). "Mutagenesis and Laue structures of enzyme intermediates: isocitrate dehydrogenase [published erratum appears in Science 1995 Oct 20;270(5235):365]." Science **268**(5215): 1312-8.

Bon, C., M. S. Lehmann and C. Wilkinson (1999). "Quasi-Laue neutron-diffraction study of the water arrangement in crystals of triclinic hen egg-white lysozyme." Acta Cryst. D **55**: 978-987.

Borah, B., C. W. Chen, W. Egan, M. Miller, A. Wlodawer and J. S. Cohen (1985). "Nuclear magnetic resonance and neutron diffraction studies of the complex of ribonuclease A with uridine vanadate, a transition-state analog." Biochemistry **24**: 2058-2067.

Brettel, K. (1997). "Electron transfer and arrangement of the redox cofactors in photosystem I." Biochim. Biophys. Acta **1318**(3): 322-373.

Brettel, K., I. Siekmann, P. Fromme, A. Van der Est and D. Stehlik (1992). "Low-temperature EPR on single crystals of photosystem I: Study of the iron-sulfer center F_A." Biochim. Biophys. Acta **1098**: 266-270.

Brooks, H. B. and V. L. Davidson (1994). "Free-energy dependence of the electron-transfer reaction between methylamine dehydrogenase and amicyanin." J. Am. Chem. Soc. **116**(24): 11201-11202.

Carrell, H. L., J. P. Glusker, V. Burger, F. Manfre, D. Tritsch and J. F. Biellmann (1989). "X-ray analysis of D-xylose isomerase at 1.9 A: native enzyme in complex with substrate and with a mechanism-designed inactivator." Proc Natl Acad Sci U S A **86**(12): 4440-4.

Chandra, S. and S. D. Aziz (1994). "Leidenfrost evaporation of liquid-nitrogen droplets." J. Heat Transfer - Trans. ASME **116**: 999-1006.

Chen, L., R. C. Durley, F. S. Mathews and V. L. Davidson (1994a). "Structure of an electron transfer complex: methylamine dehydrogenase, amicyanin, and cytochrome c551i." Science **264**: 86-90.

Chen, Y. Q., J. Kraut, R. L. Blakely and R. Callender (1994b). "Determination by Raman spectroscopy of the pKa of N5 of dihydrofolate bound to dihydrofolate reductase: Mechanistic implications." Biochemistry **33**: 7021-7026.

Coates, L., P. T. Erskine, S. P. Wood, D. A. Myles and J. B. Cooper (2001). "A neutron Laue diffraction study of endothiapepsin: implications for the aspartic proteinase mechanism." Biochemistry **40**(44): 13149-57.

Collyer, C. A., K. Henrick and D. M. Blow (1990). "Mechanism for aldose-ketose interconversion by D-xylose isomerase involving ring opening followed by a 1,2-hydride shift." J Mol Biol **212**(1): 211-35.

Crawford, R. K. (1978). "General principles of time-of-flight scattering instrument design." IPNS -- A National Facility for Condensed Matter Research. J. M. Carpenter, D. L. Price and N. J. Swanson. Argonne, IL, Argonne National Laboratory. **ANL-78-88:** 204.

Cunane, L. M., Z.-W. Chen, R. C. E. Durley and F. S. Mathews (1996). "X-ray structure of the cupredoxin amicyanin, from *Paracoccus denitrificans*, refined at 1.31 Å resolution." Acta Cryst. D **52**(4): 676-686.

Daggett, V. and M. Levitt (1993). "Realistic simulations of native-protein dynamics in solution and beyond." Ann. Rev. Biophys. Biomol. Struct. **22**: 353-380.

Davey, C. A. and T. J. Richmond (2002). "DNA-dependent divalent cation binding in the nucleosome core particle." Proc. Natl. Acad. Sci. USA **99**: 11169-11174.

Davidson, V. L. (2000). "What controls the rates of interprotein electron-transfer reactions?" Acc. Chem. Res. **33**: 87-93.

Davidson, V. L. (2002). "Chemically gated electron transfer. A means of accelerating and regulating rates of biological electron transfer." Biochemistry **41**(50): 14633-14636.

Deacon, A., T. Gleichmann, A. J. Kalb(Gilboa), H. Price, J. Raftery, G. Bradbrook, J. Yariv and J. R. Helliwell (1997). "The structure of concanavalin A and its bound solvent determined with small-molecule accuracy at 0.94 Å resolution." J. Chem. Soc., Faraday Trans. **93**: 4305.

Desmarais, W. T., D. L. Bienvenue, K. P. Bzymek, R. C. Holz, G. A. Petsko and D. Ringe (2002). "The 1.20 A resolution crystal structure of the aminopeptidase from Aeromonas proteolytica complexed with tris: a tale of buffer inhibition." Structure (Camb) **10**(8): 1063-72.

Doster, W., S. Cusack and W. Petry (1990). "Dynamic instability of liquid-like motions in globular proteins observed by inelastic neutron scattering." Phys. Rev. Lett. **65**: 1080-1083.

Egli, M. (2002). "DNA-cation interactions: Quo vadis?" Chem. Biol. **9**(3): 277-286.

Elofsson, A. and L. Nilsson (1993). "How consistent are molecular dynamics simulations? Comparing structure and dynamics in reduced and oxidized *Escherichia coli* thioredoxin." J. Mol. Biol. **233**(4): 766-780.

Englander, S. W., D. B. Calhoun, J. J. Englander, N. R. Kallenbach, R. K. Liem, E. L. Malin, C. Mandal and J. R. Rogero (1980). "Individual breathing reactions measured in hemoglobin by hydrogen exchange methods." Biophys. J. **32**(1): 577-589.

Englander, S. W., N. W. Downer and H. Teitelbaum (1972). "Hydrogen exchange." Ann. Rev. Biochem. **41**: 903-924.

Engler, N., A. Ostermann, N. Niimura and F. G. Parak (2003). "Hydrogen atoms in proteins: Positions and dynamics." Proc. Natl. Acad. Sci. USA **100**(18): 10243-10248.

Farber, G. K., A. Glasfeld, G. Tiraby, D. Ringe and G. A. Petsko (1989). "Crystallographic studies of the mechanism of xylose isomerase." Biochemistry **28**(18): 7289-97.

Feirke, C. A., K. A. Johnson and S. J. Benkovic (1987). "Construction and evaluation of the kinetic scheme associated with dihydrofolate reductase from *Escherichia coli*." Biochemistry **26**(13): 4085-4092.

Ferreira, K. N., T. M. Iverson, K. Maghlaoui, J. Barber and S. Iwata (2004). "Architechture of the photosynthetic oxygen-evolving center." Science **303**: 1831-1838.

Finch, J. T., A. Lewit-Bentley, G. A. Bentley, M. Roth and P. A. Timmins (1980). "Neutron diffraction from crystals of nucleosome core particles." Proc. Royal Soc. (London) **B290**: 635-638.

Frick, L., J. P. MacNeela and R. Wolfenden (1987). "Transition-state stabilization by deaminases - Rates of nonenzymatic hydrolysis of adenosine and cytidine." Bioorg. Chem. **15**(2): 100-108.

Fromme, P. (1998). "Crystallization of photosystem I for structural analysis. Berlin, Germany, Technical University Berlin.

Fromme, P., Ed. (2003). Crystallization of photosystem I, International University Line.

Gibson, W. M., A. J. Schultz, H. H. Chen-Mayer, D. F. R. Mildner, T. Gnäupel-Herold, M. E. Miller, H. J. Prask, R. Vitt, R. Youngman and J. M. Carpenter (2002). "Polycapillary focusing optic for small-sample neutron crystallography." J. Appl. Cryst. **35**: 677-683.

Guenot, J. and P. A. Kollman (1992). "Molecular dynamics studies of a DNA-binding protein: 2. An evaluation of implicit and explicit solvent models for the molecular dynamics simulation of the *Escherichia coli* trp repressor." Protein Sci. **1**(9): 1185-1205.

Gutberlet, T., U. Heinemann and M. Steiner (2001). "Protein crystallography with neutrons - status and perspectives." Acta Cryst. D **57**(2): 349-354.

Habash, J., J. Raftery, R. Nuttall, H. J. PRice, C. Wilkinson, A. J. K. (Gilboa) and J. R. Helliwell (2000). "Direct determination of the positions of the deuterium atoms of

the bound water in concanavalin A by neutron Laue crystallography." Acta Cryst. D **56**: 541-550.
Hanson, B. L., P. Langan, A. K. Katz, X. Li, J. M. Harp, J. P. Glusker, B. P. Schoenborn and G. J. Bunick (2004). "A preliminary time-of-flight neutron diffraction study of *Streptomyces rubiginosus* D-xylose isomerase." Acta Cryst. D **60**: 241-249.
Helliwell, J. R. (1997). "Neutron Laue diffraction does it faster." Nature Struct. Biol. **4**(11): 874-876.
Ho, J.-X., J.-P. Declercq, D. A. A. Myles, B. S. Wright, J. Ruble and D. C. Carter (2001). "Neutron structure of monoclinic lysozyme crystals produced in microgravity." Cryst. Growth **232**(4): 317-325.
Howard, E., R. Sanishvili, R. E. Cachau, A. Mitschler, B. Chevrier, V. Barth, V. Lamour, M. Van Zandt, E. Sibley, C. Bon, D. Moras, T. R. Schneider, A. Joachimiak and A. Podjarny (2004). "Ultrahigh resolution drug design I: Details of interactions in human aldose reductase-inhibitor complex at 0.66 Å." Proteins: Struct. Funct. Genet. **55**: 792-804.
Howell, E. E., J. E. Villafranca, M. S. Warren, S. J. Oatley and J. Kraut (1986). "Functional-role of aspartic acid-27 in dihydrofolate-reductase revealed by mutagenesis." Science **231**(4742): 1123-1128.
Hud, N. V. and J. Plavec (2003). "A unified model for the origin of DNA sequence-directed curvature." Biopolymers **69**: 144-159.
Hvidt, A. and K. Liderstromlang (1954). "Exchange of hydrogen atoms in insulin with deuterium atoms in aqueous solutions." Biochim. Biophys. Acta **14**(4): 574-575.
Hvidt, A. and S. O. Nielsen (1966). "Hydrogen exchange in proteins." Adv. Protein Chem. **21**: 287-386.
Hwang, T. L., S. Mori, A. J. Shaka and P. C. v. Zijl (1997). "Application of phase-modulated CLEAN chemical EXchange spectroscopy (CLEANEX-PM) to detect water-protein proton exchange and intermolecular NOEs." J Am Chem Soc **119**: 6203-6204.
Hwang, T. L., P. C. v. Zijl and S. Mori (1998). "Accurate quantitation of water-amide proton exchange rates using the phase-modulated CLEAN chemical EXchange (CLEANEX-PM) approach with a Fast-HSQC (FHSQC) detection scheme." J Biomol NMR **11**: 221-6.
Iverson, E. B. (2002). "Monte Carlo simulations of the SNS target system. http://www.sns.gov/users/instrument_systems/components/moderator/.
Iverson, E. B., P. D. Ferguson, F. X. Gallmeier and I. I. Popova (2002). "Detailed SNS neutronics calculations for scattering instrument design: SCT configuration. Oak Ridge, TN, Oak Ridge National Laboratory**:** 1-17.
Iwata, S., C. Ostermeier, B. Ludwig and H. Michel (1995). "Structure at 2.8 Å resolution of cytochrome c oxidase from *Paracoccus denitrificans*." Nature **376**: 660-669.
Jauch, W. (1986). Prospects of ISIS in single-crystal diffractometry. ISIS Workshop, Rapallo, Italy.
Jauch, W. (1993). "Accuracy of structural information from single crystal pulsed neutron diffraction: Achievements and implications." Transactions ACA **29**: 55-61.
Jauch, W. (1997). "Prospects of single-crystal diffraction at a long pulse spallation source." J. Neutron Research **6**: 161-171.

Jelsch, C., M. M. Teeter, V. Lamzin, V. Pichon-Pesme, R. H. Blessing and C. Lecomte (2000). "Accurate protein crystallography at ultra-high resolution: Valence electron distribution in crambin." Proc. Natl. Acad. Sci. USA **97**: 3171-3176.

Jordan, P., P. Fromme, O. Klukas, H. T. Witt, W. Saenger and N. Krauß (2001). "Three-dimensional structure of cyanobacterial photosystem I at 2.5 Å resolution." Nature **411**: 909-917.

Kachalova, G. S., A. N. Popov and H. D. Bartunik (1999). "A steric mechanism for inhibition of CO binding to heme proteins." Science **284**(5413): 473-476.

Kalb(Gilboa), A. J., D. A. A. Myles, J. Habash, J. Raftery and J. R. Helliwell (2001). "Neutron Laue diffraction experiments on a large unit cell: Concanavalin A complexed with methyl-D-glucopyranoside." J. Appl. Cryst. **34**(4): 454-457.

Kamiya, N. and J. R. Shen (2003). "Crystal structure of oxygen-evolving photosystem II from *Thermosynechoccus vulcanus* at 3.7 Å resolution." Proc. Natl. Acad. Sci. USA **100**: 98-103.

Kamlowski, A., A. van der Est, P. Fromme, N. Krauss, W. D. Schubert, O. Klukas and D. Stehlik (1997a). "The structural organization of the PsaC protein in photosystem I from single crystal EPR and X-ray crystallographic studies." Biochim. Biophys. Acta **1319**: 185-198.

Kamlowski, A., A. Van der Est, P. Fromme and D. Stehlik (1997b). "Low temperature EPR on photosystem I single crystals: Orientation of the iron sulfur centers FA and FB." Biochim. Biophys. Acta **1319**: 185-198.

Kamlowski, A., S. G. Zech, P. Fromme, R. Bittl, W. Lubitz, H. T. Witt and D. Stehlik (1998). "The radical pair state P700.+A1.- in photosystem I single crystals: Orientation dependence of the transient spin-polarized EPR spectra." J. Phys. Chem. B **102**(42): 8266-8277.

Kempf, J. G. and J. P. Loria (2002). "Protein dynamics from solution NMR: Theory and applications." Cell Biochem. & Biophys. **39**: 187-212.

Kitson, D. H., F. Avbelj, J. Moult, D. T. Nguyen, J. E. Mertz, D. Handzi and A. T. Hagler (1993). "On achieving better than 1 Å resolution accuracy in a simulation of a large protein: *Streptomyces griseus* protease A." Proc. Natl. Acad. Sci. USA **90**(19): 8920-8924.

Klukas, O., W. D. Schubert, P. Jordan, N. Krauss, P. Fromme, H. T. Witt and W. Saenger (1999a). "Localization of two phylloquinones, Q_K and $Q_{K'}$, in an improved electron density map of photosystem I at 4 Å resolution." J. Biol. Chem. **274**: 7361-7367.

Klukas, O., W. D. Schubert, P. Jordan, N. Krauss, P. Fromme, H. T. Witt and W. Saenger (1999b). "Photosystem I, an improved model of the stromal subunits PsaC, PsaD, and PsaE." J. Biol. Chem. **274**: 7351-7360.

Kossiakoff, A. A. (1982). "Protein dynamics investigated by the neutron diffraction-hydrogen exchange technique." Nature **296**: 713-721.

Kossiakoff, A. A. (1983). "Neutron protein crystallography: Advances in methods and applications." Annu. Rev. Biophys. Bioeng. **12**: 159-182.

Kossiakoff, A. A. (1984). "Use of the neutron diffraction-H/D exchange technique to determine the conformational dynamics of trypsin." Basic Life Sci. **27**: 281-304.

Kossiakoff, A. A. (1985). "The application of neutron crystallography to the study of dynamic and hydration properties of proteins." Ann. Rev. Biochem. **54**: 1195-1227.
Kossiakoff, A. A. (1988). "Tertiary structure is a principal determinant to protein deamidation." Science **240**: 191-194.
Kossiakoff, A. A. (1995). "Structure of growth hormone-receptor complex and mechanism of receptor signaling." J. Nucl. Med. **36**: 14-16.
Kossiakoff, A. A., J. Shpungin and M. D. Sintchak (1990). "Hydroxyl hydrogen conformations in trypsin determined by the neutron diffraction solvent difference map method: Relative importance of steric and electrostatic factors in defining hydrogen-bonding geometries." Proc. Natl. Acad. Sci. USA **87**: 4468-4472.
Kossiakoff, A. A., M. D. Sintchak, J. Shpungin and L. G. Presta (1992). "Analysis of solvent structure in proteins using neutron D_2O/H_2O solvent maps: Pattern of primary and secondary hydration of trypsin." Proteins: Struct. Funct. Genet. **12**: 223-236.
Kossiakoff, A. A. and S. A. Spencer (1980). "Neutron diffraction identifies His 57 as the catalytic base in trypsin." Nature **288**(5789): 414-416.
Kossiakoff, A. A. and S. A. Spencer (1981). "Direct determination of protonation states of aspartic acid-102 and histidine-57 in the tetrahedral intermediate of the serine proteases: Neutron structure of trypsin." Biochemistry **20**: 6462-6474.
Kossiakoff, A. A., M. Ultsch and A. De Vos (1993). "The structure of the hGH-hGH receptor complex: Implications of receptor activation." Structure **1**: 16-17.
Kossiakoff, A. A., M. Ultsch, S. White and C. Eigenbrot (1991). "Neutron structure of subtilisin BPN': Effects of chemical environment on hydrogen-bonding geometries and the pattern of hydrogen-deuterium exchange in secondary structure elements." Biochemistry **30**(5): 1211-1221.
Kuhn, P., M. Knapp, S. M. Soltis, G. Ganshaw, M. Thoene and R. Bott (1998). "The 0.78 Å structure of a serine protease: *Bacillus lentus* subtilisin." Biochemistry **37**(39): 13446-13452.
Kurihara, K. (2001). J. Phys. Soc. Jpn. Suppl. **A70**: 400-402.
Langan, P., G. Greene and B. P. Schoenborn (2004). "Protein crystallography with spallation neutrons: The user facility at Los Alamos Neutron Science Center." J. Appl. Cryst. **37**: 24-31.
Lanyi, J. K. and B. Schobert (2003). "Mechanism, of protein transport in bacteriorhodopsin from crystallographic structures of the K, L, M1, and M2' intermediates of the photocycle." J. Mol. Biol. **328**: 439-450.
Larsen, T. M., J. E. Wedekind, I. Rayment and G. H. Reed (1996). "A carboxylate oxygen of the substrate bridges the magnesium ions at the active site of enolase: structure of the yeast enzyme complexed with the equilibrium mixture of 2-phosphoglycerate and phosphoenolpyruvate at 1.8 A resolution." Biochemistry **35**(14): 4349-58.
Lavie, A., K. N. Allen, G. A. Petsko and D. Ringe (1994). "X-ray crystallographic structures of D-xylose isomerase-substrate complexes position the substrate and provide evidence for metal movement during catalysis." Biochemistry **33**(18): 5469-80.

Lee, W.-T. and X.-L. Wang (2002). "IDEAS: A General Purpose Software Package for Simulating Neutron Scattering Instruments." Neutron News **13**(4): 30-34.
Li, X., P. Langan, R. Bau, I. Tsyba, F. E. Jenney, Jr., M. W. Adams and B. P. Schoenborn (2004). "W3Y single mutant of rubredoxin from Pyrococcus furiosus: a preliminary time-of-flight neutron study." Acta Crystallogr D Biol Crystallogr **60**(Pt 1): 200-2.
Longhi, S., M. Czjzek, V. Lamzin, A. Nicolas and C. Cambillau (1997). "Atomic resolution (1.0 Å) crystal structure of *Fusarium solani* cutinase: Stereochemical analysis." J. Mol. Biol. **268**(4): 779-799.
Machczynski, M. C., H. B. Gray and J. H. Richards (2002). "An outer-sphere hydrogen-bond network constrains copper coordination in blue proteins." J. Inorg. Biochem. **88**: 375-380.
Maharaj, G., B. S. Selinsky, J. R. Appleman, M. Perlman, R. E. London and R. L. Blakley (1990). "Dissociation constants for dihydrofolic acid and dihydrobiopterin and implications for mechanistic models for dihydrofolate reductase." Biochemistry **29**(19): 4554-4560.
Marcus, R. A. and N. Sutin (1985). "Electron transfers in chemistry and biology." Biochim. Biophys. Acta **811**: 265-322.
McDowell, R. S. and A. A. Kossiakoff (1995). "A comparison of neutron diffraction and molecular dynamics structures: Hydroxyl group and water molecule orientations in trypsin." J. Mol. Biol. **250**(4): 553-570.
Mesecar, A. D. and D. E. Koshland, Jr. (2000a). "A new model for protein stereospecificity." Nature **403**(6770): 614-5.
Mesecar, A. D. and D. E. Koshland, Jr. (2000b). "Sites of binding and orientation in a four-location model for protein stereospecificity." IUBMB Life **49**(5): 457-66.
Mesecar, A. D., B. L. Stoddard and D. E. Koshland, Jr. (1997). "Orbital steering in the catalytic power of enzymes: small structural changes with large catalytic consequences." Science **277**(5323): 202-6.
Miele, A. E., L. Federici, G. Sciara, F. Draghi, M. Brunori and B. Vallone (2003). "Analysis of the effect of microgravity on protein crystal quality: The case of a myoglobin triple mutant." Acta Cryst. D **59**(6): 982-988.
Mildner, D. F. R., H. H. Chen-Mayer, W. M. Gibson, T. Gnäupel-Herold, M. E. Miller, H. J. Prask, A. J. Schultz, R. Vitt and R. Youngman (2002). "A monolithic polycapillary focusing optic for polychromatic neutron diffraction applications." Rev. Sci. Instrum. **73**(5): 1985-1993.
Minasov, G., V. Tereshko and M. Egli (1999). "Atomic-resolution crystal structures of B-DNA reveal specific influences of divalent metal ions on conformation and packing." J. Mol. Biol. **291**: 83-99.
Minasov, G., X. Wang and B. K. Shoichet (2002). "An ultrahigh resolution structure of TEM-1 beta-lactamase suggests a role for Glu166 as the general base in acylation." J Am Chem Soc **124**(19): 5333-40.
Mitsuoka, K., K. Murata, T. Walz, T. Hirai, P. Agre, J. B. Heymann, A. Engel and Y. Fujiyoshi (1999). "The structure of aquaporin-1 at 4.5 Å resolution reveals short alpha-helices in the center of the monomer." J. Struct. Biol. **128**: 34-43.

Mori, S., C. Abeygunawardana, P. C. M. v. Zijl and J. M. Berg (1996a). "Water exchange filter with improved sensitivity (WEX II) to study solvent-exchangeable protons. Application to the consensus zinc finger peptide CP-1." JMR **B 110**: 96-101.

Mori, S., J. M. Berg and P. C. M. v. Zijl (1996b). "Separation of intramolecular NOE and exchange peaks in water exchange spectroscopy using spin-echo filters." JBNMR **7**: 77-82.

Neutze, R., E. Pebay-Peyroula, K. Edman, A. Royant, J. Navarro and E. M. Landau (2002). "Bacteriorhodopsin: A high-resolution structural view of vectorial proton transport." Biochim. Biophys. Acta **1565**: 144-167.

Niimura, N. (1999a). "Neutron structural biology." J. Phys. Chem. Solids **60**(8-9): 1265-1271.

Niimura, N. (1999b). "Neutrons expand the field of structural biology." Curr. Op. Struct. Biol. **9**(5): 602-608.

Niimura, N., Y. Minezaki, T. Nonaka, J. C. Castagna, F. Cipriani, P. Hoghoj, M. S. Lehmann and C. Wilkinson (1997). "Neutron Laue diffractometry with an imaging plate provides an effective data collection regime for neutron protein crystallography." Nat Struct Biol **4**(11): 909-14.

Olkhova, E., M. C. Hutter, M. A. Lill, V. Helms and H. Michel (2004). "Dynamic water networks in cytochrome c oxidase from *Paracoccus denitrificans* investigated by molecular dynamics simulations." Biophys. J. **86**(4): 1873-1889.

Ostermann, A., I. Tanaka, N. Engler, N. Niimura and F. G. Parak (2002). "Hydrogen and deuterium in myoglobin as seen by a neutron structure determination at 1.5 angstrom resolution." Biophys. Chem. **95**(3): 183-193.

Ostermeier, C., A. Harrenga, U. Ermler and H. Michel (1997). "Structure at 2.7 Å resolution of the *Paracoccus denitrificans* two-subunit cytochrome c oxidase complexed with an antibody FV fragment." Proc. Natl. Acad. Sci. USA **94**: 10547-10553.

Palmer, A. G., C. D. Kroenke and J. P. Loria (2001). "Nuclear magnetic resonance methods for quantifying microsecond-to-millisecond motions in biological macromolecules." Meth. Enzymol. **339 Part B**: 204-238.

Pebay-Peyroula, E., R. M. Garavito, J. P. Rosenbusch, M. Zulauf and P. A. Timmins (1995). "Detergent structure in tetragonal crystals of OmpF porin." Structure **3**: 1051-1059.

Penel, S., E. Pebay-Peyroula, M. Rosenbusch, G. Rummel, T. Schirmer and P. A. Timmins (1998). "Detergent binding in trigonal crystals of Ompf porin from *Escherichia coli*." Biochemie **80**: 543-551.

Phillips, S. E. (1984). "Hydrogen bonding and exchange in oxymyoglobin." Basic Life Sciences. B. P. Schoenborn. **27:** 305-322.

Pirrung, M. C., H. Han and J. Chen (1996). "O-Alkyl Hydroxamates as Metaphors of Enzyme-Bound Enolate Intermediates in Hydroxy Acid Dehydrogenases. Inhibitors of Isopropylmalate Dehydrogenase, Isocitrate Dehydrogenase, and Tartrate Dehydrogenase(1)." J Org Chem **61**(14): 4527-4531.

Prince, S. M., T. D. Howard, D. A. A. Myles, C. Wilkinson, M. Z. Papaiz, A. A. Freer, R. J. Cogdell and N. W. Isaacs (2003). "Detergent Structure in Crystals of the Integral Membrane Light-harvesting Complex LH2 from Rhodopseudomonas acidophila Strain 10050." J. Mol. Biol. **326**: 307-312.

Qin, J., G. M. Clore and A. M. Gronenborn (1996). "Ionization equilibria for side-chain carboxyl groups in oxidized and reduced human thioredoxin and in the complex with its target peptide from the transcription factor NFκB." Biochemistry **35**: 7-13.

Raghavan, N. V. and A. Wlodawer (1987). "Neutron crystallography of proteins." Methods in experimental physics: Neutron scattering. K. Sköld and D. L. Price. Orlando, FL, Academic Press. **23:** 335-365.

Rasmussen, B. F., A. M. Stock, D. Ringe and G. A. Petsko (1992). "Crystalline ribonuclease A loses function below the dynamic transition at 220 K." Nature **357**(6377): 423-424.

Rose, I. A., E. L. O'Connell and R. P. Mortlock (1969). Biochem. Biophys. Acta **178**: 376-379.

Roth, M., B. Arnoux, A. Ducruix and F. Reiss-Husson (1991). "Structure of the detergent phase and protein-detergent interactions in crystals of the wild-type (strain Y) *Rhodobacter sphaeroides* photochemical reaction center." Biochemistry **30**: 9403-9413.

Roth, M., A. Lewit-Bentley, H. Michel, J. Deisenhofer, R. Huber and D. Oesterhelt (1989). "Detergent structure in crystals of a bacterial photosynthetic reaction center." Nature **340**(6235): 659-662.

Rubach, J. K. and B. V. Plapp (2003a). "Amino Acid residues in the nicotinamide binding site contribute to catalysis by horse liver alcohol dehydrogenase(,)." Biochemistry **42**(10): 2907-15.

Rubach, J. K. and B. V. Plapp (2003b). "Mobility of Fluorobenzyl Alcohols Bound to Liver Alcohol Dehydrogenases as Determined by NMR and X-ray Crystallographic Studies." Biochemistry **42**(4): 1178.

Saibil, H., M. Chabre and D. Worcester (1976). "Neutron diffraction studies of retinal rod outer segment membranes." Nature **262**: 266-270.

Sarkhel, S., A. Rich and M. Egli (2003). "Water-nucleobase "stacking": H-π and lone pair-π interactions in the atomic resolution crystal structure of an RNA pseudoknot." J. Am. Chem. Soc. **125**: 8998-8999.

Schmidt, M., B. Meier and F. Parak (1996). "X-ray structure of the cambialistic superoxide dismutase from *Propionibacterium shermanii* active with Fe or Mn." J. Biol. Inorg. Chem. **1**(6): 532-541.

Schobert, B., L. S. Brown and J. K. Lanyi (2003). "Crystallographic structures of the M and N intermediates of bacteriorhodopsin: Assembly of a hydrogen-bonded chain of water molecules between Asp-96 and the retinal Schiff base." J. Mol. Biol. **330**: 553-570.

Schoenborn, B. P. (1972). "A neutron diffraction analysis of myoglobin. 3. Hydrogen-deuterium bonding in side chains." Cold Spring Harbor Symp. Quant. Biol. **36**: 569-575.

Schoenborn, B. P. (1975). "Advantages of neutron scattering for biological structure analysis. Neutron scattering for the analysis of biological structures." Brookhaven Symp. Biol. **27**: 10-17.

Schoenborn, B. P. (1984)." Basic Life Sciences. B. P. Schoenborn. New York, Plenum Press. **27:** 261-281.

Schoenborn, B. P. (1985). Methods Enzymol. **114**: 510.

Schoenborn, B. P. (1996)." Basic Life Sciences. B. P. Schoenborn and R. B. Knott. New York, Plenum Press. **64:** 1-16.
Schoenborn, B. P. and P. Langan (2004). "Protein crystallography with spallation neutrons." J. Synchrotron Rad. **11**: 80-82.
Schreiber, H. and O. Stenhauser (1992). "Cutoff size does strongly influence molecular dynamics results on solvated polypeptides." Biochemistry **31**(25): 5856-5860.
Serp, D., M. Mueller, U. Von Stockar and I. W. Marison (2002). "Low-temperature electron microscopy for the study of polysaccharide ultrastructures in hydrogels. I. Theoretical and technical considerations." Biotechnol. Bioeng. **79**: 243-252.
Shibata, M., T. Tanimoto and H. Kandori (2003). "Water molecules in the Schiff base region of bacteriorhodopsin." J. Am. Chem. Soc. **125**: 13312-13313.
Shpungin, J. and A. A. Kossiakoff (1985). "A method of solvent structure analysis for proteins using D_2O-H_2O neutron difference maps." Methods Enzymol. **127**: 329-342.
Shu, F., V. Ramakrishnan and B. P. Schoenborn (2000). "Enhanced visibility of hydrogen atoms by neutron crystallography on fully deuterated myoglobin." Proc. Natl. Acad. Sci. USA **97**: 3872-3877.
Snijder, A., P. A. Timmins and B. W. Dijkstra (2002). "Detergent organisation in crystals of monomeric outer membrane phospholipase A." Acta Crystallographica Section A **58**(s1): C49.
Stellwagen, N. and U. Mohanty, Eds. (2004). Curvature and deformation of nucleic acids: Recent advances, new paradigms. Am. Chem. Soc. Symp. Ser.
Stoddard, B. L. (1998). "New results using Laue diffraction and time-resolved crystallography." Curr Opin Struct Biol **8**(5): 612-8.
Stoddard, B. L., B. E. Cohen, M. Brubaker, A. D. Mesecar and D. E. Koshland, Jr. (1998). "Millisecond Laue structures of an enzyme-product complex using photocaged substrate analogs." Nat Struct Biol **5**(10): 891-7.
Stoddard, B. L., A. Dean and P. A. Bash (1996). "Combining Laue diffraction and molecular dynamics to study enzyme intermediates." Nat Struct Biol **3**(7): 590-5.
Stubbs, G. (1999). "Developments in fiber diffraction." Curr. Op. Struct. Biol. **9**(5): 615-619.
Sui, H., B. G. Han, J. K. Lee, P. Walian and B. K. Jap (2001). "Structural basis of water-specific transport through AQPI water channel." Nature **414**: 872-878.
Sun, D., Z.-W. Chen, F. S. Mathews and V. L. Davidson (2002). "Mutation of alphaPhe55 of methylamine dehydrogenase alters the reorganization energy and electronic coupling for its electron transfer reaction with amicyanin." Biochemistry **41**: 13926-13933.
Sun, D. and V. L. Davidson (2003). "Effects of engineering uphill electron transfer into the methylamine dehydrogenase-amicyanin-cytochrome c-551i complex." Biochemistry **42**: 1772-1776.
Tanaka, I., K. Kurihara, T. Chatake and N. Niimura (2002). "A high-performance neutron diffractometer for biological crystallography (BIX-3)." J. Appl. Cryst. **35**: 34-40.
Teeter, M. M. (2001). "On the nature of the glassy state of matter in hydrated protein: Relation to protein function." Proc. Natl. Acad. Sci. USA **98**: 11242-11247.
Tereshko, V., G. Minasov and M. Egli (1999). "A "hydrat-ion" spine in a B-DNA minor groove." J. Am. Chem. Soc. **121**: 3590-3595.

Tereshko, V., C. J. Wilds, G. Minasov, T. P. Prakash, M. A. Maier, A. Howard, Z. Wawrzak, M. Manoharan and M. Egli (2001). "Detection of alkali metal ions in DNA crystals using state-of-the-art X-ray diffraction experiments." Nucleic Acids Res. **29**: 1208-1215.

Timmins, P. A. (1995). "Structural molecular biology: Recent results from neutron diffraction." Physica B **213-214**(1-4): 26-30.

Timmins, P. A., D. Wild and J. Witz (1994). "The three-dimensional distribution of RNA and protein in the interior of tomato busy stunt virus: A neutron low-resolution single-crystal study." Structure **2**: 1191-1201.

Trewhella, J., J. L. Popot, G. Zaccai and D. M. Engelman (1986). "Localization of two chymotryptic fragments in the structure of renatured bacteriorhodopsin by neutron diffraction." EMBO J. **5**(11): 3045-3049.

Tsukihara, T., H. Aoyama, E. Yamashita, T. Tomizaki, H. Yamaguchi, K. Shinzawa-Itoh, R. Nakashima, R. Yaono and S. Yoshizawa (1996). "The whole structure of the 13-subunit oxidized cytochrome c oxidase at 2.8 Å." Science **272**: 1136-1144.

Tsukihara, T., K. Shimokata, Y. Katayama, H. Shimada, K. Muramoto, H. Aoyama, M. Michizuki, K. Shinzawa-Itoh, E. Yamashita, M. Yao, Y. Ishimura and S. Yoshizawa (2003). "The low-spin heme of cytochrome c oxidase as the driving element of the proton-pumping process." Proc. Natl. Acad. Sci. USA **100**: 15304-15309.

Tsyba, I. and R. Bau (2002). "Neutron diffraction studies on proteins." Chemtracts - Inorganic Chemistry **15**: 233-257.

Vasil'ev, S., G. W. Brudwig and D. Bruce (2003). "The X-ray structure of photosystem II reveals a novel electron transport pathway between P680, cytochrome b559 and the energy-quenching cation, Ch1Z+." FEBS Lett. **543**: 159-163.

Veerapandian, B., J. B. Cooper, A. Sali, T. L. Blundell, R. L. Rosati, B. W. Dominy, D. B. Damon and D. J. Hoover (1992). "Direct observation by X-ray analysis of the tetrahedral "intermediate" of aspartic proteinases." Protein Sci **1**(3): 322-8.

Vojtechovsky, J., K. Chu, J. Berendzen, R. M. Sweet and I. Schlichting (1999). "Crystal structures of myoglobin-ligand complexes at near-atomic resolution." Biophys. J. **77**(4): 2153-2174.

Wesson, L. and D. Eisenberg (1992). "Atomic solvation parameters applied to molecular dynamics of proteins in solution." Protein Sci. **1**(2): 227-235.

Whitlow, M., A. J. Howard, B. C. Finzel, T. L. Poulos, E. Winborne and G. L. Gilliland (1991). "A metal-mediated hydride shift mechanism for xylose isomerase based on the 1.6 A Streptomyces rubiginosus structures with xylitol and D-xylose." Proteins **9**(3): 153-73.

Wilkinson, C. and M. S. Lehmann (1991). "Quasi-Laue neutron diffractometer." Nucl. Instr. Meth. A **310**: 411-415.

Williams, R. L., J. Vila, G. Perrot and H. A. Scheraga (1992). "Empirical solvation models in the context of conformational energy searches: Application to bovine pancreatic trypsin inhibitor." Proteins: Struct. Funct. Genet. **14**: 110-119.

Wilson, C. C., W. Jauch, G. J. McIntyre, D. A. A. Myles and J. Peters (2001). "Single crystal diffraction and protein crystallography instruments." Report of the ESS Instrumentation Task Group: Single Crystal Diffraction Working Group for the

ESS SAC Workshop in May 2001. F. Mezei, R. S. Eccleston and T. Gutberlet. Jülich, Germany, The ESS Project**:** 33-40.
Wlodawer, A. (1982). "Neutron diffraction of crystalline proteins." Prog. Biophys. Mol. Biol. **40**: 115-159.
Wlodawer, A. and W. A. Hendrickson (1982). "A procedure for joint refinement of macromolecular structures with X-ray and neutron diffraction data from single crystals." Acta Cryst. A **38**(2): 239-247.
Wlodawer, A., H. Savage and G. Dodson (1989). "Structure of insulin: Results of joint neutron and X-ray refinement." Acta Cryst. B **45**(1): 99-107.
Wlodawer, A. and L. Sjölin (1983). "Structure of ribonuclease A: Results of joint neutron and X-ray refinement at 2.0 Å resolution." Biochemistry **22**(11): 2720-2728.
Wlodawer, A., J. Walter, R. Huber and L. Sjölin (1984). "Structure of bovine pancreatic trypsin inhibitor: Results of joint neutron and x-ray refinement of crystal form II." J. Mol. Biol. **180**: 301-331.
Worcester, D. L., K. Hamacher, H. Kaiser, R. Kulasekere and J. Torbet (1996). "Intercalation of Small Hydrophobic Molecules in Lipid Bilayers Containing Cholesterol." Neutrons in Biology. B. Schoenborn and R. Knott. New York, Plenum Press**:** 215-226.
Xiang, S., S. A. Short, R. Wolfenden and C. W. Carter, Jr. (1995). "Transition-state selectivity for a single hydroxyl group during catalysis by cytidine deaminase." Biochemistry **34**(14): 4516-4523.
Xu, Q. and H. Guo (2004). "Quantum mechanical/molecular mechanical molecular dynamics simulations of cytidine deaminase: From stabilization of transition state analogues to catalytic mechanisms." J. Phys. Chem. B **108**(7): 2477-2483.
Zhu, Z., L. M. Cunane, Z. Chen, R. C. Durley, F. S. Mathews and V. L. Davidson (1998). "Molecular basis for interprotein complex-dependent effects on the redox properties of amicyanin." Biochemistry **37**: 17128-17136.
Zouni, A., R. Jordan, E. Schlodder, P. Fromme and H. T. Witt (2000). "First photosystem II crystals capable of water oxidation." Biochim. Biophys. Acta **1457**: 103-105.
Zouni, A., H. T. Witt, J. Kern, P. Fromme, N. Krauß, W. Saenger and P. Orth (2001). "Crystal structure of photosystem II from *Synechococcus elongatus* at 3.8 Å resolution." Nature **409**: 739-743.
Zulauf, M., P. A. Timmins and R. M. Garavito (1986). "Neutron crystallography of a membrane protein. Localization of detergent and protein at 20 Å resolution." Biophys. J. **49**: 96-98.